# Development and testing of a facility for the trapping and cooling of isomers

Krishna Manojkumar Jadeja

A dissertation submitted in partial fulfillment of the requirements for the degree of

**Doctor of Philosophy** 

of

**University College London.** 

Department of Physics and Astronomy
University College London

March 28, 2023

I, Krishna Manojkumar Jadeja, confirm that the work presented in this thesis is my own. Where information has been derived from other sources, I confirm that this has been indicated in the work.

# **Abstract**

The project presented in this thesis pertains to the intersection of atomic and nuclear physics, specifically, laser trapping techniques applied to caesium isotopes and isomers. The main experiment is a laser cooling apparatus installed at the Ion Guide Isotope Separation On-Line (IGISOL) facility at the University of Jyväskylä, Finland. When training or during delays in the primary experiment, I often worked on experiments based at UCL. The first section describes a <sup>133</sup>Cs Magneto-Optical Trap (MOT) experiment at UCL, and was used as an analogue to the isomer trapping experiment. The laser system was set up, and the vacuum chamber was prepared for the MOT, which was then characterised.

Then the isomer cooling experiment is discussed. Due to a power cut, many parts of the laser system had to be repaired. The apparatus was then tested - firstly by obtaining a  $^{133}$ Cs MOT from an ampoule, then from an offline  $^{133}$ Cs<sup>+</sup> ion beam. The experiment was further developed by establishing an offset frequency locking scheme for the laser sources. This will allow the laser frequencies to be varied for various isotopes and isomers. Frequency offsets from 200 MHz to 9.9 GHz were successfully locked to. The final section reports on an atomic magnetometer, which uses cold atoms instead of atoms at or close to room temperature. A sensitivity of  $330 \,\mathrm{pT/}\sqrt{Hz}$  with an operational range of  $15-100 \,\mathrm{kHz}$  was achieved and the result was published in [1].

Future progress is expected to include the trapping of <sup>134</sup>Cs, the beam for which shall be produced via <sup>134</sup>CsNO<sub>3</sub> samples from Institut Laue–Langevin (ILL). Long term goals include the trapping of the <sup>135m</sup>Cs isomer, and eventually a Bose-

Abstract 4

Einstein Condensate (BEC) of the isomer. This will allow the exploration of the generation of coherent gamma photons, which has many possible applications, ranging from biomedicine to fundamental studies on multi-body phenomena.

# **Impact Statement**

This thesis reports on work done to maintain and further develop an experiment in which radioactive isotopes and isomers can be laser cooled. The experiment has come about as a result of an international collaboration between University College London (UCL), in the UK and the University of Jyväskylä (JYU) in Finland.

The long-term goal of the experiment is to cool the <sup>135m</sup>Cs isomer down to a BEC, where the decay of the isomer can be used to produce coherent gamma photons. This could form the basis of a gamma ray laser, once noted as one of the 30 most important physics problems. The applications of such a laser outside of academia are wide ranging. In medicine, it could be used for imaging or cancer treatment, and higher resolution gamma imaging in the security sector. Within academia, the production of ultra-cold samples of caesium radioisotopes will allow for new studies of them, including the acquisition of spectroscopic data for chains of isotopes. In this work, the experiment was fully restored to the point that it was once again able to trap and cool atoms from an ion beam source. Additionally, an upgrade to the laser system was established, by which the cold atoms part of the experiment can now easily switch between trapping different species of caesium.

The project has received funding from the Engineering and Physical Sciences Research Council (EPSRC), the Atomic Weapons Establishment (AWE) and the European Commission under Horizon 2020. It has been active since 2014, and has had three PhD students thus far, as well as welcoming a third generation of PhD students starting in 2022.

A part of my time as a PhD student and this thesis has been dedicated to an ex-

periment that uses cold <sup>87</sup>Rb atoms as a sensor for an atomic magnetometer. Magnetometers are instruments that are used in a wide range of fields. In particular, atomic magnetometers can be used for Electromagnetic Induction Imaging (EII) where the conductivity of a material is mapped out. The control on the spatial distribution of the atoms in the magnetometer presented here could lead to higher resolution images. In terms of academic impact, the results from the magnetometer were presented in a peer-reviewed journal, Applied Physics Letters [1]. The experiment was further developed by colleagues to use a BEC as the sensor instead of cold atoms.

# Acknowledgements

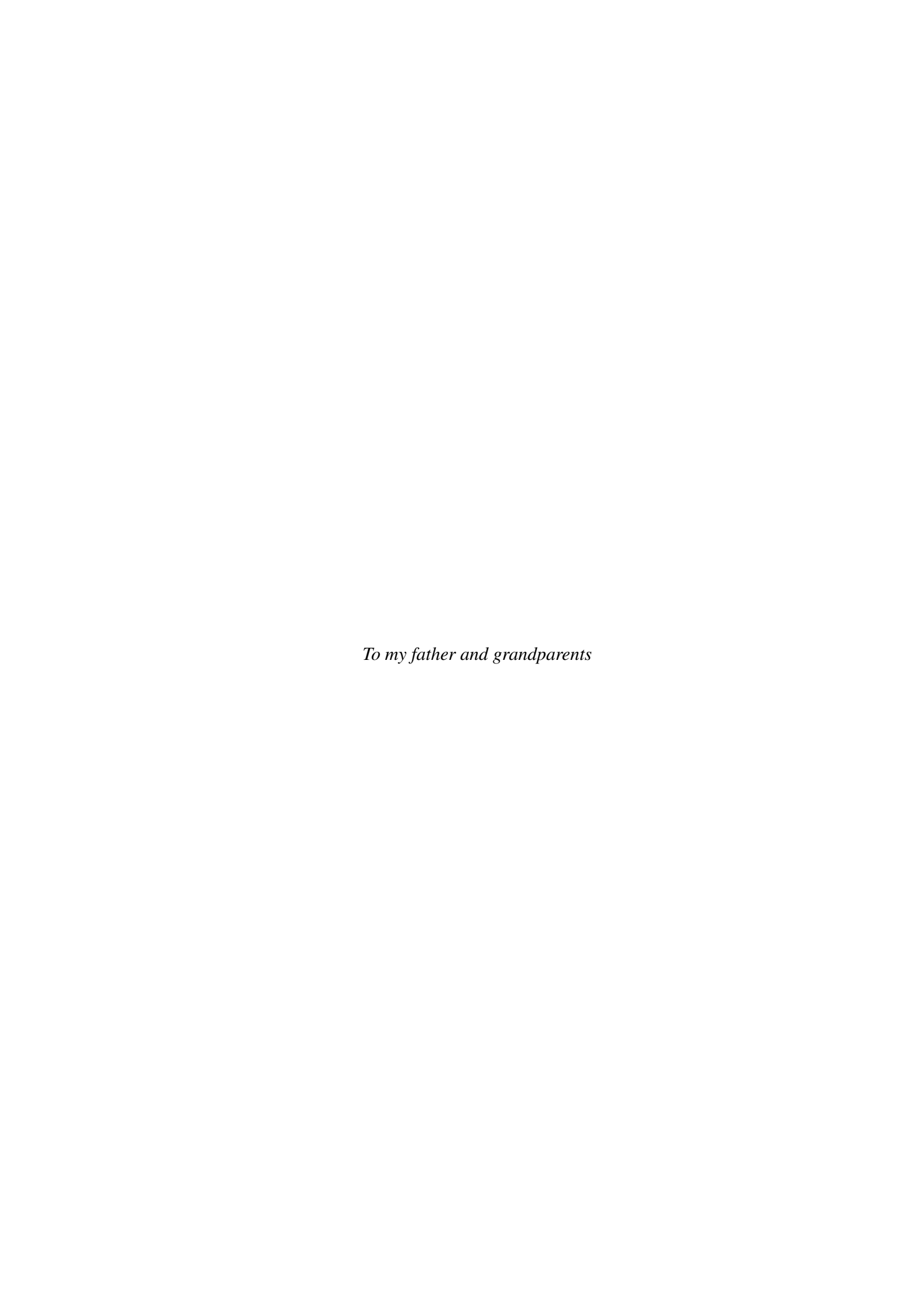
Over the course of this PhD I have been helped by many people. First, I would like to thank Professor Ferruccio Renzoni for his support and guidance. It has proved invaluable while navigating an international project during a pandemic. Thanks also to Professor Philip Jones for being my second supervisor. This work was funded by AWE plc and by the Engineering and Physical Sciences Research Council (EPSRC), via an iCASE studentship.

Dr. Luca Marmugi has had a large influence on my time working in this group. Thank you for teaching me so much about what must be nearly every aspect of experimental atomic physics and kindly replying to the countless emails and WhatsApp messages I sent.

I'd also like to express my gratitude to the current and former members of our laser cooling group at UCL. Pik, thank you for showing me the basics of working in an optics lab and for introducing me to the isomer trapping experiment with Alex. Cameron, Michela, Yuval, Sindi, Ben and Han- thank you for all your help with troubleshooting and making the lab a lively place to be. And Nin and Torin, the newer members of the group- I greatly appreciate your assistance with the latter stages of this work. I wish you the best of luck on your PhD journeys.

In Jyväskylä, I'd like to thank Professor Iain Moore for his help in getting me to Finland even when international travel was restricted and the support he provided while I was there, along with the members of the exotic nuclei and beams research group.

Thanks to Megha and Nathalie, for never failing to make me laugh or smile after talking about our PhD struggles and giving me confidence boosts when needed. And finally, to my mother Hansa, and my sisters, Surbhi and Jayshree. Without your love and support I would never have gotten to this point, and for that I cannot thank you enough.



# UCL Research Paper Declaration Form: referencing the doctoral candidate's own published work(s)

- 1. **1. For a research manuscript that has already been published** (if not yet published, please skip to section 2):
  - (a) What is the title of the manuscript? A cold atom radio-frequency magnetometer
  - (b) Please include a link to or doi for the work: https://doi.org/10.1063/1.5084004
  - (c) Where was the work published? Applied Physics Letters
  - (d) Who published the work? AIP Publishing
  - (e) When was the work published? 21/02/2019
  - (f) List the manuscript's authors in the order they appear on the publication: Yuval Cohen , Krishna Jadeja, Sindi Sula, Michela Venturelli, Cameron Deans , Luca Marmugi , and Ferruccio Renzoni
  - (g) Was the work peer reviewd? Yes
  - (h) Have you retained the copyright? Yes
  - (i) Was an earlier form of the manuscript uploaded to a preprint server (e.g. medRxiv)? If 'Yes', please give a link or doi https://arxiv.org/abs/1902.08258

If 'No', please seek permission from the relevant publisher and check the box next to the below statement:

I acknowledge permission of the publisher named under 1d to include in this thesis portions of the publication named as included in 1c.

- 2. For a research manuscript prepared for publication but that has not yet been published (if already published, please skip to section 3):
  - (a) What is the current title of the manuscript?

Acknowledgements

11

(b) Has the manuscript been uploaded to a preprint server 'e.g.

medRxiv'?

If 'Yes', please please give a link or doi:

(c) Where is the work intended to be published?

(d) List the manuscript's authors in the intended authorship order:

(e) Stage of publication:

3. For multi-authored work, please give a statement of contribution cover-

ing all authors (if single-author, please skip to section 4): The cold atoms

section of the experimental apparatus was set up by Michela Venturelli with

assistance from Luca Marmugi. The magnetometry specific additions to the

experiment were carried out by myself, Michela Venturelli and Yuval Cohen.

Data collection was carried out by myself, Yuval Cohen and Sindi Sula. Data

analysis was carried out by myself, Yuval Cohen and Cameron Deans. Fer-

ruccio Renzoni and Luca Marmugi provided guidance and support in all areas

of the work.

4. In which chapter(s) of your thesis can this material be found? Chapter 5

e-Signatures confirming that the information above is accurate (this form

should be co-signed by the supervisor/ senior author unless this is not appropriate,

e.g. if the paper was a single-author work):

**Candidate:** 

Date:

23/02/2023

**Supervisor/Senior Author signature** (where appropriate):

**Date:** 24/02/2023

# **Contents**

| 1 | Intr | oductio | n                                      | 23 |
|---|------|---------|--|----|
|   | 1.1  | Isome   | ric physics                            | 23 |
|   | 1.2  | Cohere  | ent gamma photon generation in a BEC   | 25 |
|   | 1.3  | Atomi   | c physics techniques for nuclear study | 28 |
|   | 1.4  | Thesis  | outline                                | 33 |
| 2 | Caes | sium-13 | 33 Magneto Optical Trap                | 35 |
|   | 2.1  | Worki   | ng principles                          | 35 |
|   |      | 2.1.1   | Laser cooling                          | 35 |
|   |      | 2.1.2   | Magneto-Optical Trap                   | 36 |
|   | 2.2  | Appara  | atus                                   | 37 |
|   |      | 2.2.1   | Lasers                                 | 37 |
|   |      | 2.2.2   | Vacuum chamber                         | 40 |
|   |      | 2.2.3   | Optical alignment                      | 43 |
|   |      | 2.2.4   | Magnetic fields                        | 47 |
|   | 2.3  | Proced  | lure                                   | 49 |
|   |      | 2.3.1   | MOT imaging                            | 49 |
|   |      | 2.3.2   | Measurement protocol                   | 50 |
|   | 2.4  | Charac  | eterisation of the MOT                 | 50 |
|   |      | 2.4.1   | MOT lifetime                           | 50 |
|   |      | 2.4.2   | MOT size                               | 55 |
|   |      | 2.4.3   | Number of atoms                        | 56 |
|   |      | 2.4.4   | Temperature of MOT                     | 58 |

| Contents | 14 |
|----------|----|
| Contents | 14 |

| 3 | Caes           | sium Iso                       | omer Trapping   | 61 |
|---|----------------|--------------------------------|---|----|
|   | 3.1            | Apparatus                      |   |    |
|   |                | 3.1.1                          | High energy apparatus                                     | 61 |
|   |                | 3.1.2                          | Low energy apparatus                                      | 62 |
|   |                | 3.1.3                          | Ion neutralisation  | 64 |
|   |                | 3.1.4                          | Cold atoms chamber  | 66 |
|   |                | 3.1.5                          | Optical alignment   | 67 |
|   |                | 3.1.6                          | Magnetic fields   | 70 |
|   |                | 3.1.7                          | Fluorescence imaging                                      | 71 |
|   |                | 3.1.8                          | Offline caesium-133 ion beam                              | 72 |
|   | 3.2            | Setbac                         | ks to the experiment                                      | 73 |
|   |                | 3.2.1                          | Power cuts and resulting damage                           | 73 |
|   |                | 3.2.2                          | COVID-19 pandemic   | 73 |
|   | 3.3            | Experi                         | mental repairs  | 74 |
|   |                | 3.3.1                          | Uninterruptible Power Supply (UPS)                        | 74 |
|   |                | 3.3.2                          | Vacuum system   | 74 |
|   |                | 3.3.3                          | Repump slave ECDL   | 75 |
|   |                | 3.3.4                          | RadiantDyes NarrowDiode Cooling laser                     | 76 |
|   |                | 3.3.5                          | Tapered Amplifier (TA)                                    | 78 |
|   | 3.4            | Testing of repaired experiment |   | 80 |
|   |                | 3.4.1                          | MOT from caesium-133 vapour                               | 80 |
|   |                | 3.4.2                          | MOT from offline caesium-133 ion beam                     | 81 |
|   | 3.5            | Offline                        | caesium-134 & <sup>135</sup> aesium-135 ion beams         | 86 |
|   |                | 3.5.1                          | Irradiated caesium  | 86 |
|   |                | 3.5.2                          | Preparation of ion beam                                   | 87 |
|   |                | 3.5.3                          | Caesium-133 test beam                                     | 88 |
| 4 | Offset Locking |                                |   | 90 |
|   | 4.1            | Variati                        | on in cooling cycle frequencies with isotopes and isomers | 90 |
|   | 4.2            | Frequency offset locking       |   | 92 |
|   |                | 4.2.1                          | Offset Phase Lock Servo (OPLS)                            | 92 |

| Contents | 15 |
|----------|----|
|----------|----|

|    |      | 4.2.2                     | Optical alignment                     | . 96  |  |
|----|------|---------------------------|---------------------------------------|-------|--|
|    |      | 4.2.3                     | Beat note and locking                 | . 97  |  |
| 5  | Cold | l Atom                    | Magnetometry                          | 101   |  |
|    | 5.1  | Worki                     | ng principles                         | . 102 |  |
|    | 5.2  | Appar                     | atus and procedure                    | . 103 |  |
|    | 5.3  | Result                    | s and analysis                        | . 106 |  |
|    |      | 5.3.1                     | Response of magnetometer              | . 106 |  |
|    |      | 5.3.2                     | Operational range                     | . 107 |  |
|    |      | 5.3.3                     | Effect of atom number                 | . 108 |  |
| 6  | Con  | clusion                   | s and Outlook                         | 110   |  |
|    | 6.1  | Summ                      | ary                                   | . 110 |  |
|    | 6.2  | Offline                   | e caesium-134 & caesium-135 ion beams | . 111 |  |
|    | 6.3  | Planned apparatus updates |                                       |       |  |
|    |      | 6.3.1                     | Pneumatic gate valve                  | . 113 |  |
|    |      | 6.3.2                     | MagneTOF detector                     | . 114 |  |
| Ap | pend | ices                      |                                       | 115   |  |
| A  | Fluo | rescen                    | ce imaging MOT population calibration | 115   |  |
| В  | Bak  | ing of v                  | acuum chamber                         | 117   |  |
| C  | PDN  | AS coat                   | ing procedure                         | 118   |  |

# **List of Figures**

| 1.1  | Diagram of isomer types and their energy states                                     | 24 |
|------|---|----|
| 1.2  | Diagram of two step decay of ${}^{135m}$ Cs to ${}^{135}$ Cs                        | 27 |
| 1.3  | Fine and hyperfine structure of ${}^{133}$ Cs $6^2P_{3/2}$ state, with nuclear spin |    |
|      | $I = \frac{7}{2}$ . Hyperfine energy shift denoted by $\Delta E$                    | 28 |
| 2.1  | Energy levels of a two state atom undergoing Zeeman splitting in a                  |    |
|      | magnetic field gradient   | 37 |
| 2.2  | Hyperfine structure of the $^{133}\mathrm{Cs}$ with cooling cycle transitions shown | 38 |
| 2.3  | SAS and error signals for the $6s^2S_{1/2}$ , $F=3$ ground state                    | 40 |
| 2.4  | Labelled DAVLL spectrum of the $^{133}$ Cs $F=4$ manifold                           | 41 |
| 2.5  | Vacuum chamber used to obtain a MOT in UHV  | 42 |
| 2.6  | Optical alignment for cooling and repump lasers; spectroscopy and                   |    |
|      | amplification sections  | 44 |
| 2.7  | Optical alignment for cooling and repump lasers on MOT table                        | 46 |
| 2.8  | Optical alignment for first MOT   | 47 |
| 2.9  | Optical alignment for second MOT  | 48 |
| 2.10 | Imaging beam path   | 49 |
| 2.11 | Flowchart of LabVIEW imaging sequence   | 51 |
| 2.12 | Decay of MOT fluorescence for the measurements of the MOT life-                     |    |
|      | time  | 53 |
| 2.13 | Fitting of MOT fluorescence decay   | 54 |
| 2.14 | Fitting of MOT fluorescence decay   | 55 |
| 2.15 | Number of atoms trapped in the MOT for TOF = 4ms, as it varies                      |    |
|      | with the detuning of the MOT beams  | 57 |

3.19 Fluorescence of MOT captured from offline  $^{133}\text{Cs}^+$  beam . . . . .

|      | List of Figures   | 18 |
|------|---|----|
| 3.21 | Diagram of 'Hot Cavity'   | 88 |
| 3.22 | The current detected at the switch yard due to the ion beam 8           | 89 |
| 3.23 | Mass spectrometry measurement of the ion beam                           | 89 |
| 4.1  | Schematic of the OPLS internal circuit, illustrating how the beat       |    |
|      | note is converted to an error signal                                    | 93 |
| 4.2  | Error signal produced by the OPLS                                       | 95 |
| 4.3  | Transfer function of the OPLS   | 96 |
| 4.4  | Optical alignment used with the Vescent OPLS                            | 97 |
| 4.5  | Error signal shown with spectroscopy of slave laser                     | 98 |
| 4.6  | Locked and unlocked beat frequencies as seen on the spectrum anal-      |    |
|      | yser  | 99 |
| 4.7  | Demonstration of the range of frequency offsets that can be locked . 10 | 00 |
| 5.1  | Optical pumping with $\sigma^+$ light being used to polarise atoms with |    |
|      | two states and three Zeeman split levels                                | )3 |
| 5.2  | Apparatus used for magnetometry   | )5 |
| 5.3  | FFT of polarimeter signal for Larmor oscillation, and a noise FFT 10    | )7 |
| 5.4  | Lorentzian fits of data acquired using the lock-in amplifier, with      |    |
|      | resonant frequencies of 17 kHz, 52 kHz, 75 kHz, and 99 kHz 10           | 98 |
| 5.5  | Sensitivity of magnetometer as a function of the number of atoms 10     | )9 |

# **List of Tables**

| 4.1 | Parameters for the calculation of transition frequencies for different |    |
|-----|--|----|
|     | species of caesium   | 91 |
| 4.2 | Summary of cooling and repump transition frequency shifts for          |    |
|     | <sup>135</sup> Cs. <sup>134</sup> Cs. and <sup>135m</sup> Cs.          | 97 |

# Acronyms

**AOM** Acousto-Optical Modulator.

**APNC** Atomic Parity Non-Conservation.

AWE Atomic Weapons Establishment.

**BEC** Bose-Einstein Condensate.

**CCD** Charge Coupled Device.

**DAVLL** Dichroic Atomic Vapour Laser Lock.

**ECDL** External Cavity Diode Laser.

**EDM** Electric Dipole Moment.

EII Electromagnetic Induction Imaging.

**EPSRC** Engineering and Physical Sciences Research Council.

FFT Fast Fourier Transform.

**HWP** Half Waveplate;  $\lambda/2$ .

**IGISOL** Ion Guide Isotope Separation On-Line.

ILL Institut Laue-Langevin.

JYU University of Jyväskylä.

Acronyms 21

**LabVIEW** Laboratory Virtual Instrumentation Engineering Workbench.

LVIS Low Velocity Intense Source.

MATLAB (MATrix LABoratory).

MOPA Master Oscillator Power Amplifier.

**MOSFET** Metal-Oxide Semiconductor Field-Effect Transistor.

**MOT** Magneto-Optical Trap.

NPBS Non-Polarising Beam Splitter.

**OI** Optical Isolator.

**OPLS** Offset Phase Lock Servo.

**PBS** Polarising Beam Splitter.

**PDMS** Polydimethylsiloxane.

**PFD** Phase Frequency Detector.

**PGC** Polarisation Gradient Cooling.

PID Proportional-Integral-Differential.

**PMT** Photon-Multiplier Tube.

**PSD** Phase Space Density.

**QWP** Quarter Waveplate;  $\lambda/4$ .

**RF** Radio Frequency.

**RF-OAM** Radio Frequency Optical Atomic Magnetometer.

**SAS** Saturated Absorption Spectroscopy.

**SNR** Signal to Noise Ratio.

**TA** Tapered Amplifier.

**TOF** Time of Flight.

UCL University College London.

UHV Ultra-High Vacuum.

**VCO** Voltage Controlled Oscillator.

### Chapter 1

# Introduction

The primary purpose of developing a facility for the cooling and trapping of isomers is the condensation of the  $^{135m}$ Cs isomer into a Bose-Einstein Condensate (BEC). Such a condensate was predicted to be capable of generating coherent gamma photons, and forming the basis of a nuclear gamma ray laser [2]. In addition to this, trapping other species of caesium could enable further research into their atomic and even nuclear structure.

This chapter introduces the physics relevant to this work; that of isomers and BECs. Having established the relevant physics, the proposed mechanism by which coherent gamma photons could be generated is described. The wider use of atomic physics and its techniques in the field of nuclear study is discussed, alongside a description of current and past optical trapping of neutral radioisotopes. Finally, the structure of the thesis is outlined.

### 1.1 Isomeric physics

Much like isotopes are atoms with the same number of protons but different numbers of neutrons, isomers are atoms with nuclei that have the same number of protons and neutrons, but they exist in different nuclear energy states. Most nuclei in excited states immediately decay down to the nuclear ground state, however metastable isomeric states exist [3].

Metastable states are comparatively long-lived; this can range from nanoseconds to year long half lives [4]. The only naturally occurring isomer, <sup>180m</sup>Ta, has a

half life of  $10^{15}$  years. As per isomeric state notation, the m following the atomic mass number indicates that the state is the first metastable excitation. n, p and q indicate successive long lived excitations [4]. The long-lived nature of metastable isomers is a result of these states having only low probability avenues of decay available. The low probabilities can be linked to the properties of the isomeric state; either its shape, its spin, or the projection of its spin onto the nuclear symmetry axis [3].

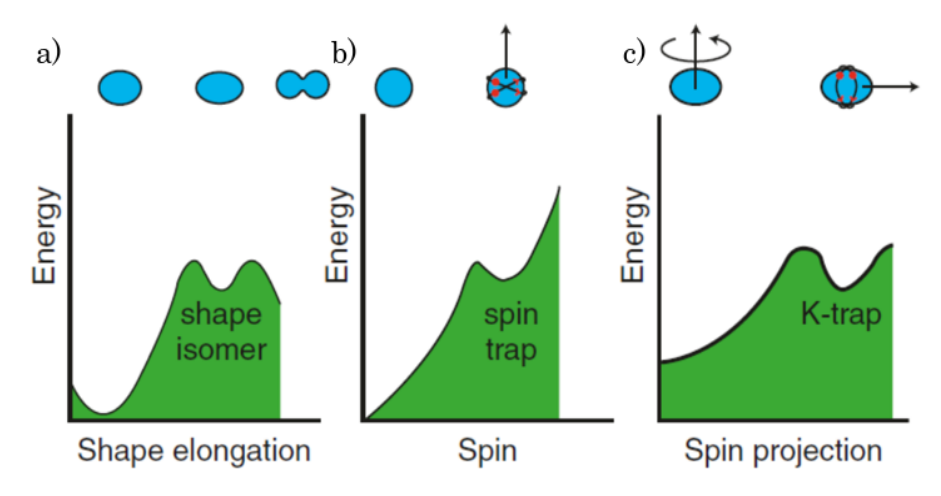


**Figure 1.1:** Diagram of isomer types and their energy states.

These three types of isomers will generally have a second energy minimum in addition to the ground state according to the relevant property, as illustrated in Figure 1.1 [3]. For shape isomers, there exists a specific arrangement of nucleons that is energetically favourable and significantly different to the ground state. In order to decay, the nucleons must 'rearrange' to the ground state configuration, which is highly improbable. An interesting instance of this is <sup>242m</sup>Am [5], which is so elongated that the ratio of the minor and major axes of the nucleus is 2:1. Its excitation relative to the ground state is 2.2 MeV, with a half life of 14 ms.

The long half lives of spin isomer states can be attributed to the spin selection rules that must be obeyed for a decay to take place. The decay to the ground state often necessitates a large change in spin. For example, <sup>180</sup>mTa, mentioned above, can decay down to the ground state <sup>180</sup>Ta with an emission of gamma radiation.

However, there is a large difference between the nuclear spin of the two states; the isomeric state has I = 9, and the ground state has I = 1. Hence the decay to the ground state requires the emission of radiation that has an angular momentum of  $8\hbar$ , or a multipolarity of  $\lambda = 8$ .

The third and final type of isomer is the K isomer. The 'K' refers to the projection of the nuclear spin I onto the symmetry axis of the nucleus, as shown in Figure 1.1. K isomers only exist in nuclei that are very deformed, but are still axially symmetric, like a rugby ball. These isomers tend to be far from stable spherically shaped nuclei in N-Z space, where the number of protons in a nucleus, Z, is plotted against the number of neutrons, N. Though decay to a ground state via an emission of correct multipolarity ( $\lambda$ ) may seem necessary for a change in K value, it is not. There are in fact symmetry breaking processes that make other K non-conserving decays not only possible, but more probable. In the case of  $^{180m}$ Hf, I = 8 and K = 8, the most probable route of decay is via a 58 keV,  $\lambda = 1$  radiation emission. The resulting state has I = 8 and K = 0, thus breaking the  $\lambda \ge \Delta K$  rule [3].

As well as being a large and interesting area of research in nuclear physics, nuclear isomers also present an opportunity for the energy sector. Also known as 'energy traps', isomers carry large amounts of trapped energy as a result of their excited nuclear state. Long-lived isomers, such as the naturally occurring <sup>180m</sup>Ta, can be induced to decay (also known as triggering) in some way and release the stored energy [3]. This has been done with an electron beam for the 31 year <sup>178</sup>Hf isomer, which has an excitation energy of 2.446 MeV and a many step decay to the ground state [6]. <sup>180m</sup>Ta has also been triggered, using a photon beam [7]. Isomers could also be induced to decay by laser radiation [8], [9].

## 1.2 Coherent gamma photon generation in a BEC

A BEC is a state of matter in which bosonic atoms all occupy the lowest quantum state. It was first predicted in 1924-1925 in the works of Bose and Einstein [10, 11, 12]. Experimentally, a BEC was first realised in 1995 with <sup>87</sup>Rb [13], and later in <sup>133</sup>Cs in 2003 [14]. A BEC can be described by a single wave-function,

meaning that the particles in the BEC are coherent, and that the BEC itself is a single quantum-mechanical entity on a macroscopic scale. Condensation occurs as a result of cooling the particles down (typically to  $10^{-7}$  K), which causes an enlargement of the de Broglie wavelength associated with the bosons:

$$\lambda_{dB} = \sqrt{\frac{2\pi\hbar^2}{mk_BT}} \tag{1.1}$$

which is determined by the mass m and temperature T of the particle.  $k_B$  is the Boltzmann constant. The phase-space density (PSD) in Eq. 1.2 is equal to the number of particles in a volume equal to the cube of  $\lambda_{dB}$ :

$$PSD = n\lambda_{dB}^3 \tag{1.2}$$

When  $\lambda_{dB}$  becomes greater than the interatomic distance, i.e. when the PSD exceeds unity, the particles collapse into the lowest accessible energy quantum state. An experiment to trap and cool caesium isomers has been developed as a result of the identification of a mechanism through which a BEC of the metastable spin isomer of caesium,  $^{135m}$ Cs, may be used in the generation of coherent gamma photons. Such a phenomenon could form the basis for a gamma ray laser, once noted as one of the 30 most important problems in modern physics [15]. Such a laser would have applications in a wide range of fields, including security imaging, medical imaging and medicine itself.

One potential method of generating coherent gamma photons involves condensing positronium down into a BEC, in which the annihilation of the positrons and electrons of positronium atoms in the condensate will generate gamma photons of 511 keV [16, 17]. An alternative suggestion utilising nuclear gamma emission is the stimulated emission of <sup>229m</sup>Th nuclei that are suspended within a LiCaAlF<sub>6</sub> crystal, as the use of the crystal theoretically allows population inversion and absorption of photons without recoil [18].

The mechanism considered here is as follows: the <sup>135m</sup>Cs isomer is cooled

down to a BEC. Within it, the decay of a single isomer will trigger the collective decay of the BEC as a whole. As a result of the coherence of this decay, the emitted gamma photons will also be coherent [2]. The isomer has a lifetime of 53 minutes and a two step gamma photon decay to the  $^{135}$ Cs ground state (shown in Figure 1.2), the first of which will generate the coherent gamma photons. It is an 846.1 keV decay from the I=19/2 nuclear spin state to an intermediate I=11/2 state. The emission is M4, meaning that the emission is magnetic hexadecapole radiation with an angular momentum of  $4\hbar$ .

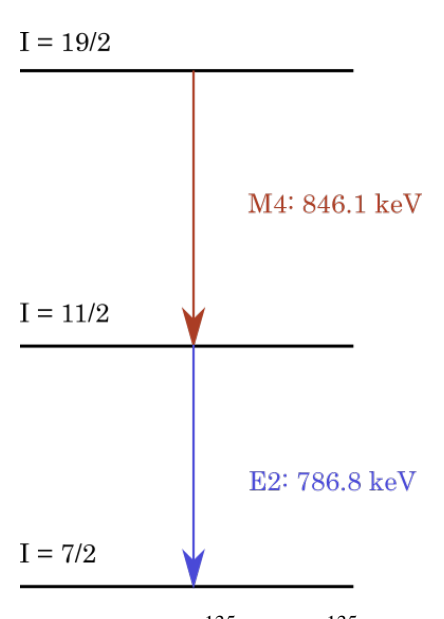


**Figure 1.2:** Diagram of two step decay of  $^{135m}$ Cs to  $^{135}$ Cs. Also shown, are the angular momenta of the nucleus during the decay process.

The use of a BEC allows for the accumulation of a sufficient number of isomeric nuclei and a reduction of the linewidth of the emission due to the low temperatures of a BEC. In the approach proposed above, it is also instrumental in providing the coherence required for the generation of coherent gamma photons. The isomeric BEC approach avoids some of the known problems with approaches to a nuclear gamma ray laser. In single pass amplification, due to the large nuclear recoil there is a large difference between the absorption and emission wavelengths. The nuclear recoil energy for the  $^{135m}$ Cs is 2.8 eV - much larger than the natural linewidth of the transition of  $10^{-19}$  eV [2].

Another approach is Dicke super-radiance, the collective emission from a sample of atoms, which is started by coherent excitation from an optical pulse [19]. However, this requires a separation between the super radiance medium (the nuclei) less than the radiation's wavelength. Were this approach attempted with the <sup>135m</sup>Cs isomer, the super-radiance medium would be the <sup>135m</sup>Cs nuclei, rather than the atoms themselves. The separation required between the nuclei would then be smaller than the size of the caesium atom, and such densities are not currently achievable. The mechanism of a coherent decay of the <sup>135m</sup>Cs isomer BEC does not require such a high density of atoms.

### 1.3 Atomic physics techniques for nuclear study

Laser spectroscopy is a tool used to understand the electronic structure of atoms and the electronic transitions which can occur. With accurate enough spectroscopy, important information about the nature and structure of the nucleus can be extrapolated from knowledge of an atom's electronic structure. The following section is intended to give context to what may be possible to investigate with caesium species other than the  $^{135m}$ Cs isomer.

The hyperfine structure of an atom arises due to the interaction between the electrons and nucleus of said atoms. The contributions made to the energy shift of the hyperfine structure from the fine structure level (as shown in Figure 1.3) can be separated into the different magnetic and electric moments of the nucleus.

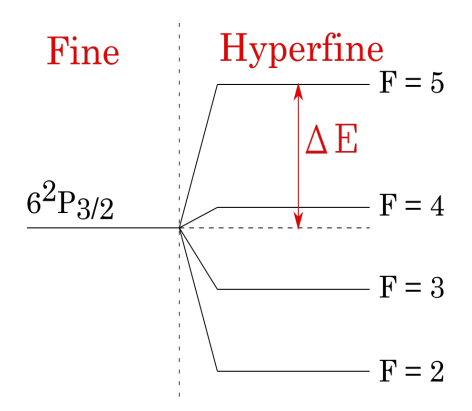


**Figure 1.3:** Fine and hyperfine structure of  $^{133}$ Cs  $6^2P_{3/2}$  state, with nuclear spin  $I = \frac{7}{2}$ . Hyperfine energy shift denoted by  $\Delta E$ 

The hyperfine energy shift is equal to:

$$\Delta E = \frac{1}{2}AK + B\frac{\frac{3}{2}K(K+1) - 2I(I+1)J(J+1)}{2I(2I-1)2J(2J-1)}$$
(1.3)

where I is the nuclear spin, J is the total electron angular momentum, and K is as below [20],

$$K = F(F+1) - I(I+1) - J(J+1)$$
(1.4)

with F being the total atomic angular momentum,

$$F = |\mathbf{I} + \mathbf{J}| \tag{1.5}$$

The two constants A and B are the magnetic dipole and electric quadrupole hyperfine constants respectively. In general, the terms in the energy shift formula are limited to the larger magnetic dipole and electric quadrupole moments, as the contributions of further moments to the hyperfine shift are  $10^8$  smaller [21].

The value of these constants can be found by measuring the hyperfine splitting via spectroscopy, and these in turn make it possible to measure the nuclear moments associated with them. Gerginov et al. used extremely sensitive spectroscopy to measure the magnetic octupole moment of <sup>133</sup>Cs [22]. The octupole moment has a much smaller effect on the hyperfine structure, but a value for its hyperfine constant is found. Values for the electric quadrupole and magnetic octupole moments are extracted from the hyperfine constants in a dual approach with data from the spectroscopy and theoretical calculations. The octupole moment of <sup>87</sup>Rb has also been calculated by Gerginov et al. [23] from hyperfine structure intervals measured by Ye et al. [24] with a spectrometer. An atomic beam was used by Gerginov et al. [22], however cold atoms could be used to make similar measurements with enhanced resolution due to increased interrogation times [25].

While the experimental values of these nuclear moments have their importance in the nuclear field, the discrepancy between the experimental octupole moment value and the theoretical value based on an unpaired valence proton in the nuclear shell model prompts important questions about the structure of the nucleus. Indeed, spectroscopy can be used to help answer other such questions about nuclear structure. Grossman et al. measured the hyperfine anomaly in the spectroscopy of francium isotopes and considered how well the observed anomaly fits various nuclear magnetization distribution models [26].

The so-called 'hyperfine anomaly' refers to the Bohr-Weisskopf effect, which is the difference in the magnetic dipole moment hyperfine interaction between a point like nucleus and a nucleus with extended nuclear magnetisation. For the  $7^2S_{1/2}$  and  $7^2P_{1/2}$  states, the hyperfine shifts would only consist of the magnetic dipole moment term:  $\Delta E = \frac{1}{2}A_lK$ . Electronic S- and P- shells experience nuclear magnetisation differently, meaning that the constant  $A_l$  will differ for the two states. The ratio of the two constants,  $\rho_A$  is:

$$\frac{A_S}{A_P} = \rho_A = \rho_0 [1 + \varepsilon(A, S) - \varepsilon(A, P)]$$
 (1.6)

where  $\rho_0$  is the hyperfine constant ratio for a point nucleus, and the  $\varepsilon(A,S)$  and  $\varepsilon(A,P)$  are the Bohr-Weisskopf effects for the S nd P shells respectively. In these terms, the A refers to the nuclear mass. Due to this mass-dependence, measurements of  $\rho_A$  are made for many francium isotopes. These are then compared to theoretical values calculated based on different models for nuclear magnetisation, a point nucleus, nuclear magnetisation distribution the same size as the charge radii and a theoretical Bohr-Weisskopf model.

The study of nuclear magnetisation is significant because, unlike the nuclear charge which is only contributed to by protons, it is contributed to by the neutrons in the nucleus and can shed light on neutron radial distributions. In fact, it was found that the improvement of the theoretical Bohr-Weisskopf model over a model where the nuclear magnetisation distribution is the same size as the charge radii was that it was closer to matching experimental data for all isotopes studied, not just those with an even number of neutrons. The facility described in this thesis has the potential to trap many caesium isotopes, meaning that the hyperfine anomaly may be studied

for the isotope chain, including species not suitable for the generation of coherent gamma photons, such as the <sup>134</sup>Cs ground state.

The fine structure of an isotope experiences an isotope shift which is a result of changes in the nucleus. It is given by [27, 28]

$$\delta v = \frac{m_{A'} - m_A}{m_{A'} m_A} (N + S) + F \delta \langle r^2 \rangle^{A', A}. \tag{1.7}$$

The first term is the mass shift, and this accounts for the changes to the electron energy level caused by the change in the mass of the nucleus between isotope A and A' [29]. N and S are coefficients for the normal and specific mass shift. The normal mass shift is due to the change in the electron-nucleus mass ratio and can be calculated [30]. The specific mass shift is the change in frequency caused by correlation between the motions of the electrons [30].

The second term in Eq. 1.7 is the field shift. This is caused by the difference in the charge distribution of the nucleus, since the charge of the nucleus is the same for isotopes of the same element but the mass distribution will change [31]. F is the field shift constant, and  $\delta \langle r^2 \rangle^{A',A}$  is change in the mean-square charge radius of the isotope nucleus. This is measured using collinear or in-source spectroscopy [27].

To realise a BEC of the <sup>135m</sup>Cs isomer, radioactive neutral atoms will be optically trapped and cooled. Though neutral isomers have yet to be trapped in a MOT, plenty of radioisotopes have been. MOTs of radioisotopes can be used to study parity violating transitions. This is typically referred to as the Atomic Parity Non-Conservation (APNC), to stress its peculiar nature with respect to the more widely known parity-violating effects at high energies in nuclear and particle physics. Weak interactions with the nucleus generate a parity-violating moment called the anapole moment [32]. To extract the physics of the weak interactions from atomic APNC data, electron wave functions overlapping with nuclei must be understood, via isotope shifts and hyperfine splittings [33].

This is being pursued using francium MOTs [33, 34]. At the TRI-University

Meson Facility in Vancouver, Canada (TRIUMF), the isotope shifts for the  $7S \rightarrow 8S$  transition were measured for five isotope MOTs ( $^{2028-211}Fr$ ,  $^{213}Fr$ ). In addition to the two laser frequencies needed for a MOT (discussed further in Section 2.2.1), a third 1012 nm laser is shone on the MOT and its frequency is swept to excite the  $7S \rightarrow 8S$  transition. Photon-Multiplier Tubes (PMTs) then detect the 817 nm radiation associated with the decay down to the  $7P_{1/2}$  state. From this data the isotope shifts are calculated. With data for multiple isotopes, the ratio of field shifts between the isotopes can be found. Similar measurements could be made with caesium isotopes with the apparatus characterised and discussed in Chapter 3.

At the Laboratori Nazionali di Legnaro (LNL) in Legnaro, Italy, the  $7P_{3/2} \rightarrow 7D_{5/2}$  transition is detected for both  $^{209}$ Fr and  $^{210}$ Fr [35]. These results serve as a preliminary step towards observing a  $7S_{3/2} \rightarrow 6D$  transitions, which are of major interest for APNC, but are as yet unobserved [36]. As at TRIUMF, a third spectroscopy laser is used, but the excitation of the transition of interest is observed via the decrease in the fluorescence of the MOT, which is tied to the population of the MOT.

Other fundamental physics is being explored with the use of optically trapped and cooled radioisotopes. An experiment is being developed at the Cyclotron and Radioisotope Center (CYRIC) in Tohoku University, Japan, to search for the electron's permanent Electric Dipole Moment EDM using francium isotope MOTs [37]. Francium is a good candidate for the measurement of the electron's EDM, because of francium's large enhancement factor- a measure of how large an EDM will be induced in a francium atoms by an electron. The lower velocities of atoms in a MOT mean that motion-induced magnetic fields will be suppressed [38].

A MOT of  $^{37}$ K atoms has been used to measure the asymmetry of the  $\beta$ -decay with respect to the  $^{37}$ K polarisation axis to a higher precision at TRIUMF. An increase in the precision of such measurements of  $\beta$  decays, increases their sensitivity as probes of non-SM physics [39]. The cold atomic sample for the asymmetry measurements is prepared using a MOT, and then spin-polarised through opti-

cal pumping. The nuclear decay products are detected by a pair of  $\beta$  telescopes along the polarization axis. The asymmetry of the  $\beta$  decay is found by comparing the detection of  $\beta$  particles in the two telescopes. The Heavy Unseen Neutrinos from Total Energy–momentum Reconstruction (HUNTER) collaboration in the US will use a MOT of  $^{131}$ Cs to search for weakly coupled sterile neutrinos with much higher masses than flavours of neutrinos that have been observed [40]. The massive-neutrinos will be emitted as a result of electron capture events in the cooled  $^{131}$ Cs nuclei.

#### 1.4 Thesis outline

The collaboration between UCL and JYU necessitated a situation where my time would be split between London and Jyväskylä, so that I might gain experience working with cold atoms. Though the main aim of this project has been the cooling and trapping of isomers, the work carried out throughout the duration of my PhD was split across three different experiments, and the structure of the thesis reflects this.

**Chapter 2** covers the work done on a <sup>133</sup>Cs MOT. The working principles of laser cooling and MOTs are stated here. Details of the apparatus and techniques used here are included, and are in fact widely used in laser cooling including the subsequently discussed experiments. Then the MOT is characterised using a combination of imaging techniques.

Chapter 3 presents the experiment dedicated to the cooling and trapping of isomers. The large-scale apparatus is described, as well as the set backs that occurred regarding the experiment. Following this, the repairs that were carried out as a result of this are documented, alongside the tests that were made to verify that the experiment was fully restored.

**Chapter 4** reports on the differences in the cooling cycle transition frequencies for the isotopes and isomers of interest. The frequency-offset locking system by which the aforementioned laser systems can be adapted to trapping different species of caesium is characterised.

**Chapter 5** shows an experiment that uses an <sup>87</sup>Rb MOT instead of room temperature atoms as its sensor for radio frequency optical atomic magnetometry. The skills needed for the preparation of the cold atoms for this is similar to the previously discussed experiments, and as such, working on this was a part of my initial training.

**Chapter 6** summarises the contents and achievements of the thesis. Additionally, upcoming work and updates concerning the isomer trapping and cooling experiment are described.

#### **Chapter 2**

# Caesium-133 Magneto Optical Trap

The following chapter details the work carried out on an experiment for the trapping and cooling of the stable isotope of caesium, <sup>133</sup>Cs. The experiment is at UCL, and serves as a testing ground for the implementation of techniques that will be of benefit to the isomer trapping experiment discussed in Chapter 3. It also provided me with an introduction to laser cooling and Magneto-Optical Traps (MOTs). The principles behind the experiment are established before a description of the laser system and apparatus that realised the <sup>133</sup>Cs double MOT. The system by which the MOT is imaged is described, along with how the characterisation of the MOT is carried out from the images.

#### 2.1 Working principles

#### 2.1.1 Laser cooling

Laser cooling makes use of the momentum transfer that occurs between an atom and a photon being absorbed or emitted. When an atom absorbs a photon, the atom receives a momentum kick of  $\hbar k$  in the direction of the photon, where k is the wave vector of the photon. The atom will then decay back to its ground state and spontaneously emit a photon in a random direction, delivering a recoil momentum kick of  $\hbar k$  to the atom. As these recoil kicks are random in direction, if the process is repeated, the net momentum change to the atom from them is zero, meaning that the momentum change to the atom comes entirely from photon absorption of laser light.

The rate at which photons are absorbed and emitted is known as the photon scattering rate, and is given by [41]:

$$R_{sc} = \frac{\Gamma}{2} \left( \frac{I/I_{sat}}{1 + I/I_{sat} + (2\delta_{\pm}/\Gamma)^2} \right), \tag{2.1}$$

where  $\Gamma$  is the natural linewidth of the corresponding optical line, I is the laser intensity,  $I_{sat}$  is the saturation intensity and  $\delta_{\pm}$  is the detuning of the laser from the resonant frequency. This is equal to

$$\delta_{+} = \delta + kv. \tag{2.2}$$

 $\delta$  is the detuning (which is always red-detuning) of the laser frequency from the resonant frequency and v is the atomic velocity. The kv term is the Doppler shift.

Combining three orthogonal pairs of counter-propagating laser beams can cool atoms moving in any direction. This arrangement is known as optical molasses, which is capable of cooling atoms down to the Doppler temperature:

$$T_D = \frac{\hbar\Gamma}{2k_B} \tag{2.3}$$

The intensity of the cooling beams is a parameter of a trap that is optimised. An intensity of  $3.5 \text{ mW cm}^{-2}$  is generally found to be the minimum intensity required for cooling beams.

#### 2.1.2 Magneto-Optical Trap

If a magnetic field gradient is added to the above, we have a MOT, in which the force felt by the atoms becomes position dependent. With a magnetic field along the z axis of the form

$$B(z) = bz (2.4)$$

where b is a constant, the atoms within the trap will experience a Zeeman shift, related to its position with respect to the centre of the trap.

Diagram 2.1 shows the 1D Zeeman shifts for an atom with J'=1,  $m_J=0,\pm 1$ .



37

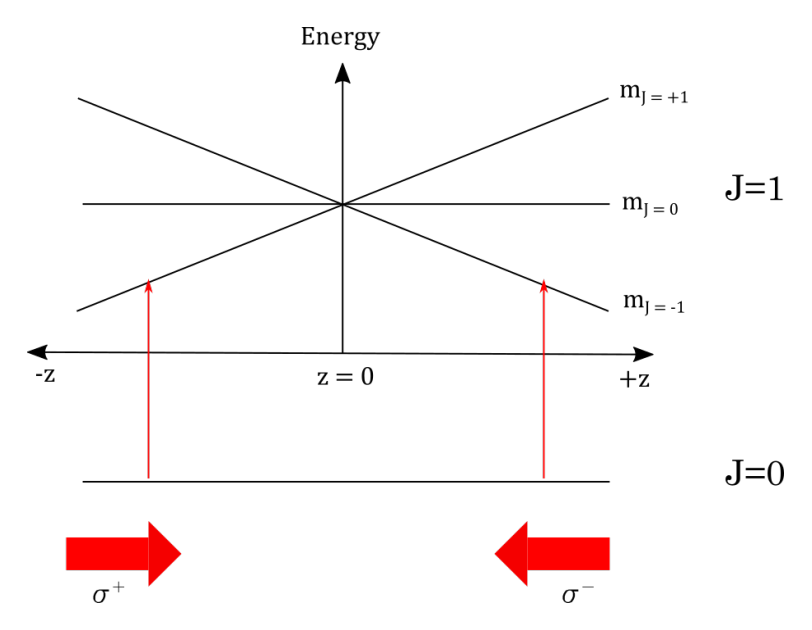


**Figure 2.1:** Energy levels of a two state atom undergoing Zeeman splitting in a magnetic field gradient.

The counter propagating laser beams have opposite circular polarisations  $\sigma^+$  and  $\sigma^-$ . Circularly polarised light can pump atoms into the adjacent  $m_J$  state.  $\sigma^-$  light will pump an atom from the  $J=0, m_J=0$  state to the  $J=1, m_J=-1$  state, and  $\sigma^+$  to  $J=1, m_J=+1$ . For an atom with position z>0, the J=0 to  $J=1, m_J=-1$  transition is closer in frequency to the red-detuned laser light due to the Zeeman effect lowering the  $m_J=-1$  state. This means that the absorption of the  $\sigma^-$  beam is more probable, the beam that will push the atoms towards the centre of the trap.

The MOT allows atoms to be trapped and cooled from a room temperature background vapour. The commonly accepted limit of a MOT is the Doppler temperature defined in Eq. 2.3. To reach the conditions for BEC, many more steps are necessary.

# 2.2 Apparatus

### **2.2.1** Lasers

Two lasers are used in the experiment, the cooling laser and the repump laser. The purpose of this is to create a closed cooling loop so the atoms can be continually cooled. The cooling laser is tuned to the  $6s^2S_{1/2}$ ,  $F = 4 \rightarrow 6p^2P_{3/2}$ , F' = 5 transi-

tion. For this reason, this optical transition is called the 'cooling transition'. Atoms are largely excited to the F'=5 state, however due to the red-detuning of the cooling laser, they can occasionally be excited to the F'=4 state. From there, they can decay down to the F=3 ground state. The latter is an atomic state that cannot be excited by the cooling laser. To prevent atoms collecting in this state, the repump laser is tuned to the  $6s^2S_{1/2}$ ,  $F=3 \rightarrow 6p^2P_{3/2}$ , F'=4 transition. In this way, the atoms that reach the  $6s^2S_{1/2}$ , F=3 state by spontaneous emission are once again in the cooling loop. The cooling laser used is an External Cavity Diode Laser (ECDL) [42, 43]. The repump laser is a CEL/850 diode laser from MOGLabs. The beam intensity is 1.1 mW cm<sup>-2</sup>.

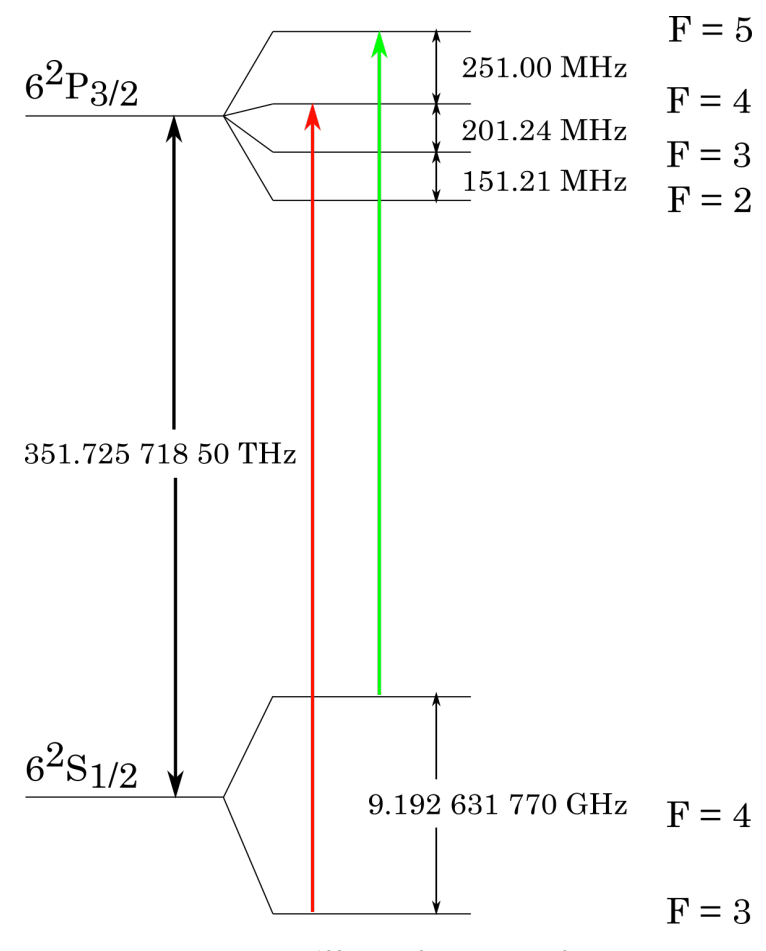


**Figure 2.2:** Hyperfine structure of the  $^{133}$ Cs  $6p^2P_{3/2}$  and  $6s^2S_{1/2}$  states, with cooling transition shown in green, and repump in red.

In order to set the frequency of the lasers, caesium vapour cells are used to find the required hyperfine optical transition, via absorption; and electronics lock onto the signals and maintain the frequency via a feedback control loop. Two methods of generating zero-passing error signals from Saturated Absorption Spectroscopy (SAS) signals are used: Dichroic Atomic Vapour Laser Locking (DAVLL) for the ECDL and electronic modulation of the SAS signal for the MOGLabs laser.

SAS uses two laser beams to remove the effects of Doppler broadening of atomic transitions, and reveal their hyperfine components- thus identifying the position of the excited hyperfine levels. If a laser beam that is on resonance is simply passed through a vapour cell once, there will be one broad peak for each ground state hyperfine level, due to Doppler broadening. However if there are two resonant beams passing through the cell, the first beam (the pump beam) will pump the atomic transitions so much so that the transition becomes saturated. Then when the second beam comes through for the spectroscopy peak, there will have been a 'hole' burnt into the peak, which allows resolution of the hyperfine components of the excited state, normally buried underneath the Doppler profile [44].

SAS gives rise to an additional feature in the spectroscopy signal known as crossover resonances. When two transitions (from the same ground state) have a frequency interval smaller than the Doppler linewidth, there exists a point between the two frequencies where the pump beam will excite one transition, and the probe beam will excite the other. This results in an extra absorption peak at this point. The crossover resonances are labelled according to the transitions they are between in Figures 2.3 and 2.4.

Figure 2.3 shows the  $6s^2S_{1/2}$ , F=3 spectroscopy signal from SAS and the corresponding error signal generated.

For caesium, typical full-width at half-maximum of the Doppler profile is 386 MHz at room temperature [45]. The excited states of interest to laser cooling are separated by 251.0 MHz, and 201.2 MHz, respectively [20]. Therefore, their observation is impossible unless SAS is used.

The signal shown in red in Figure 2.3, is the result of the current of the laser

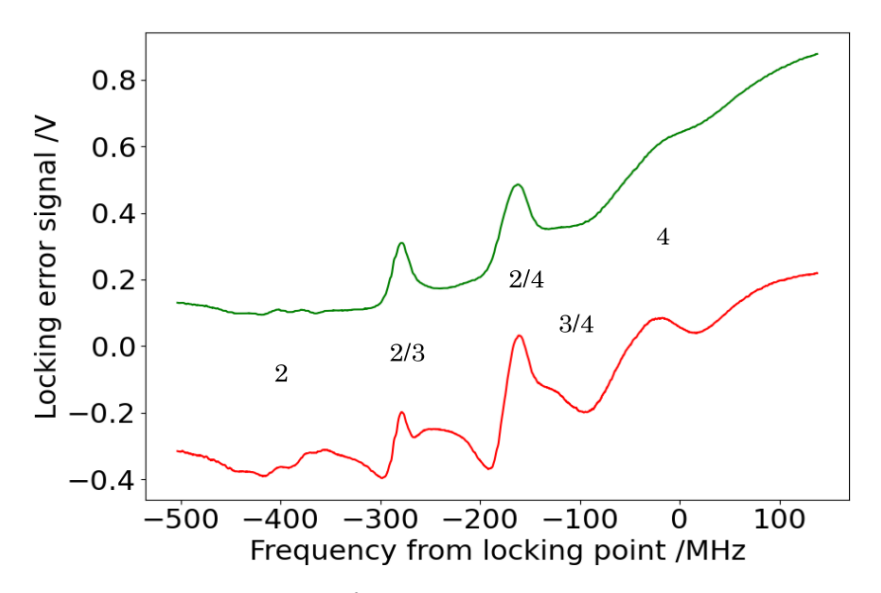


**Figure 2.3:** SAS signal for the  $6s^2S_{1/2}$ , F=3 ground state shown in green, and the corresponding error signal in red. Transitions and crossover resonances are labelled.

diode being modulated at 250 kHz by the MOGLabs ECDL Controller. This modulation converts the SAS peaks into an error signal that can be used for frequency locking.

DAVLL is an alternative method for generating an error signal from a spectroscopy signal, and in this work is used for non-commercial ECDLs. DAVLL uses Zeeman splitting to make the atomic vapour in the cell dichroic. In this condition, the absorption cross-sections of  $\sigma+$  and  $\sigma-$  polarised components of light are different [46]. Specifically for a finite magnetic field acting on the atoms, in the same direction as the propagation of the light, the centre of the absorption line will increase in frequency for  $\sigma+$  and decrease by the same amount for  $\sigma-$ . Taking the difference between the signals gives an error signal which crosses zero at the original non degenerate absorption line centre. An example of this can be seen in Figure 2.4.

### 2.2.2 Vacuum chamber

The maximum background pressure at which atoms can be loaded into a MOT is typically  $10^{-7}$  mbar. And to obtain a BEC, the background pressure should be

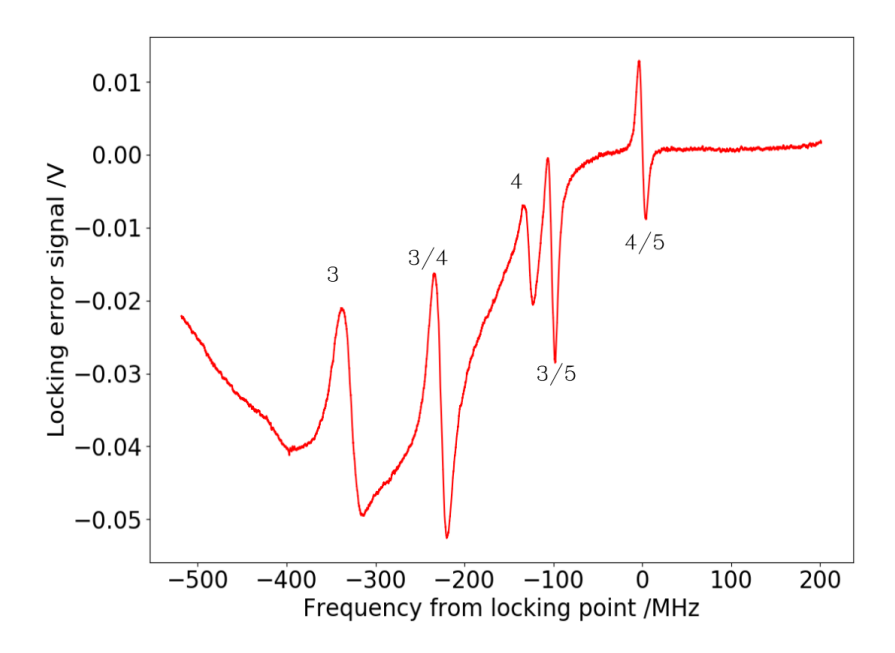


**Figure 2.4:** DAVLL spectrum of the F=4 manifold. Transitions and crossover resonances are labelled.

10<sup>-10</sup> mbar or lower. Lower pressures mean there are fewer background atoms present in a chamber that can knock atoms out of the trapped sample. As the atom cooling sequence between the MOT and BEC stages can be around 20 s, low pressures prevent too many atoms being lost to background collisions before reaching a BEC. These pressures were achieved by baking the entire chamber to Ultra-High Vacuum (UHV), a process detailed in Appendix B. It is necessary to separate where a MOT is loaded from background vapour from the chamber where a BEC would be obtained, as any background pressure from which a MOT could be loaded will be detrimental to the formation and maintenance of a BEC.

The solution to this is to use a double MOT setup, where the first chamber contains a MOT that is loaded from background caesium vapour. Though the capture velocity for a MOT is typically tens of m/s and the average thermal velocity of caesium at room temperature is in the hundreds of m/s, there are atoms in the lower end of the vapour's velocity distribution that can be trapped in the MOT.

The vapour comes from an ampoule that is in a smaller, separable part of the chamber. The pressure is generally on the order of  $10^{-8}$  mbar in the first chamber.

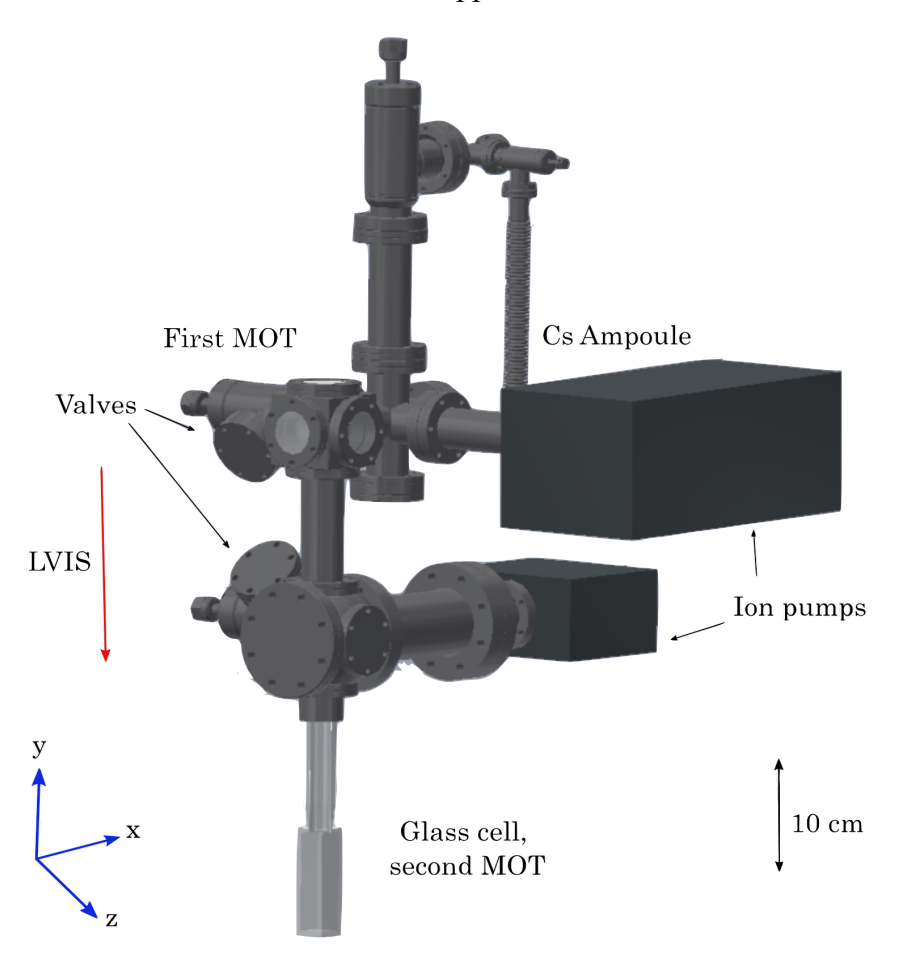


**Figure 2.5:** Vacuum chamber used to obtain a MOT in UHV. The first MOT referred to in the text is situated at the top of the chamber, where there are windowed flanges on the chamber. The second MOT is obtained in the cuboidal glass cell at the bottom of the chamber.

The second chamber has a pressure of  $10^{-10}$  mbar. Here, as a first step towards the BEC, a second MOT is loaded with an atomic beam, or a Low Velocity Intense Source (LVIS) from the first chamber's MOT [47]. Between the first chamber and the second, there is a mirror and quarter waveplate with a hole drilled into them, as well as a vacuum impedance, which is a flange with a small hole which particles can pass through. This mirror reflects a beam from outside the chamber to form one of the three counter propagating pairs of beams required for the first MOT. However the hole in the mirror means that there is a hole in the reflected beam. For that region of the trap, the force experienced by the atoms is unbalanced. So the atoms are propelled through the hole and to the second chamber.

## 2.2.3 Optical alignment

Unless stated otherwise, the height of the beams is 10.5 cm above the optical table in optical diagrams.

Laser Sources As shown in Figure 2.6, the cooling laser is passed through an anamorphic prism pair to shape the outgoing beam into a Gaussian profile. It is then fed into an optical isolator (OI) to stop optical feedback into the laser cavity, which would negatively affect the laser behaviour. After this, the beam is split into two paths by a Polarising Beam Splitter (PBS) - one going to spectroscopy and the other towards the experiment. The spectroscopy beam's frequency is shifted by an Acousto-Optical Modulator (AOM), as the laser will be locked to the F' = 4,5 crossover which is a larger peak in the spectrum, instead of the F' = 5 transition, for ease of locking.

Passing a beam through an AOM once results in a change in the beam's direction of an angle of  $n\theta$  for the nth order outgoing beam, which varies with the frequency shift. However, if the outgoing beam is reflected and passed through the AOM a second time, there is no overall change in the angle of the beam. Doing this is known as a double pass configuration, where the first order beam from the AOM is reflected back into the AOM while the zeroth order is blocked. A quarter waveplate is placed before the mirror, and the beam passes through it twice. Hence, the polarisation of the returning beam can be changed- allowing it to be separated from the initial beam.

The beam is passed to a vapour cell within a solenoid that provides the Zeeman shift necessary for DAVLL, then it passes through a quarter waveplate to convert the  $\sigma^+$  and  $\sigma^-$  components of light to vertically and horizontally polarised light before going to a balanced photodiode where the difference between the signals from each component can be taken. The beam that goes towards the experiment is amplified by a Tapered Amplifier (TA). This configuration is known as Master Oscillator Power Amplifier (MOPA). Then the beam is injected into an optical fibre, with optical isolators to protect the TA. The main difference in the alignment for the repump

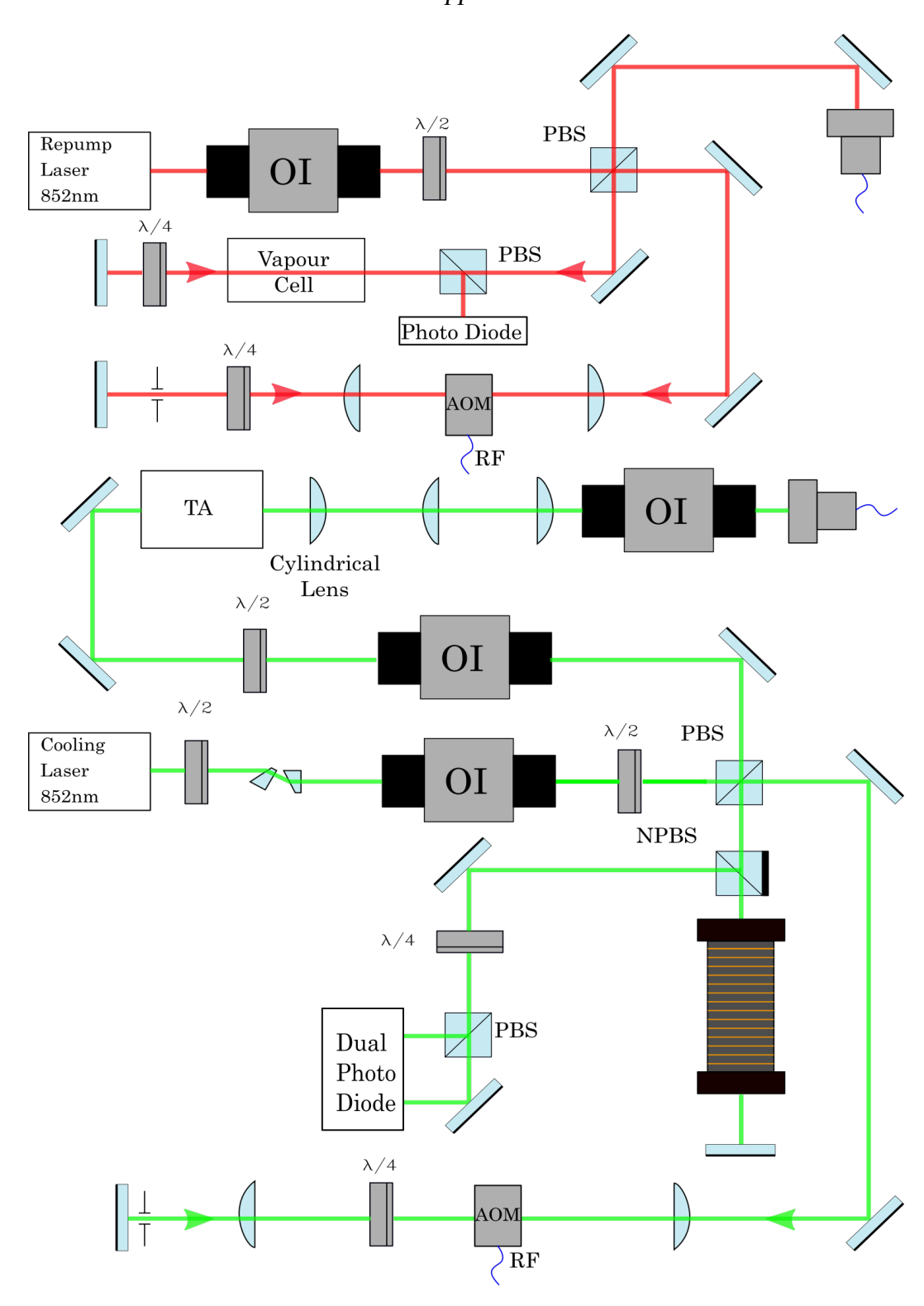


**Figure 2.6:** The area depicted is the alignment and spectroscopy section of the two lasers used in this experiment before being transported toward the vacuum chamber via optical fibres. Red is used to depict the repump laser, whilst green is used for the cooling laser. Labels used: Radio Frequency (RF), Non-Polarising Beam Splitter (NPBS), half waveplate (HWP;  $\lambda/2$ ), quarter waveplate (QWP;  $\lambda/4$ ). The arrows along the laser beam indicate where the laser beam has been reflected along its initial path.

laser is the lack of a TA. This is due to the fact that the laser diode for the repump laser is capable of reaching 120 mW, which is more than enough for the repump beams.

MOT Table The cooling laser passes through another AOM to complete the detuning necessary for locking to the F' = 4.5 crossover, before being overlapped with the repumper laser at a PBS to be split between the first and second MOTs. But just before the AOM, there is a partial mirror that takes 8% of the cooling laser away to be an imaging beam. This is used to carry out absorption imaging of the MOT, further explained in Section 2.3.1.

The first MOT beams are reflected upwards to an optical breadboard 54 cm above the optical table, as the chamber for the first MOT is at the top of the vacuum chamber. The portion of the beams for the second MOT is passed through a telescope to enlarge the beams, after which the repump and the cooling beams are separated at a PBS. They are later recombined after a half waveplate is placed in the path of each beam. This allows the amount of cooling or repump power in each of the three MOT beams to be independently varied. A similar alignment is used for the first MOT, as can be seen in Figure 2.8, with the LVIS beam being raised to a height of 23 cm above the breadboard before it is reflected down. The LVIS beam does not contain any repump light.

For the second MOT, the imaging beam and one of the MOT beams is raised to a height of 18 cm, i.e. to the centre of the glass cell as depicted in Figures 2.9 a) and b). This MOT beam does not contain any repump light. The imaging beam is raised to the same height and goes through the cell perpendicular to the first beam, through to the Charge Coupled Device (CCD) Camera. The other MOT beams are lowered to 5 cm, and then passed to the PBS shown in Figure 2.9 a). There, the two MOT beams are split and then raised to 36 cm, before entering the glass cell at an angle of 45°.

### Towards chamber, height:

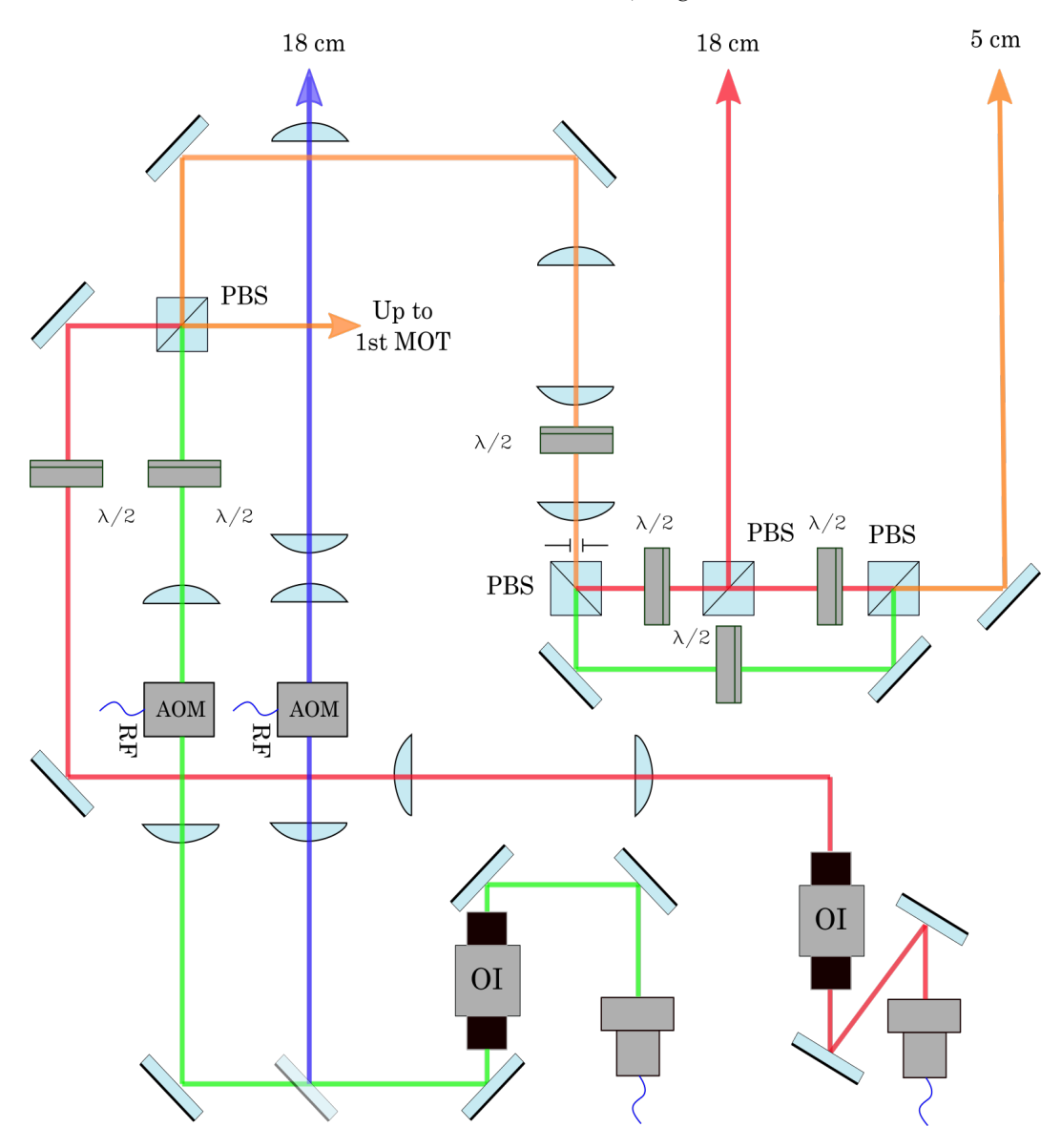


**Figure 2.7:** The optical alignment shown in this figure is that of the cooling and repump lasers after emerging from optical fibres onto the MOT table, where the vacuum chamber is placed. The division of laser beams for the second MOT is partially shown here. Orange shows repump and cooling lasers overlapped, and blue shows the imaging beam.

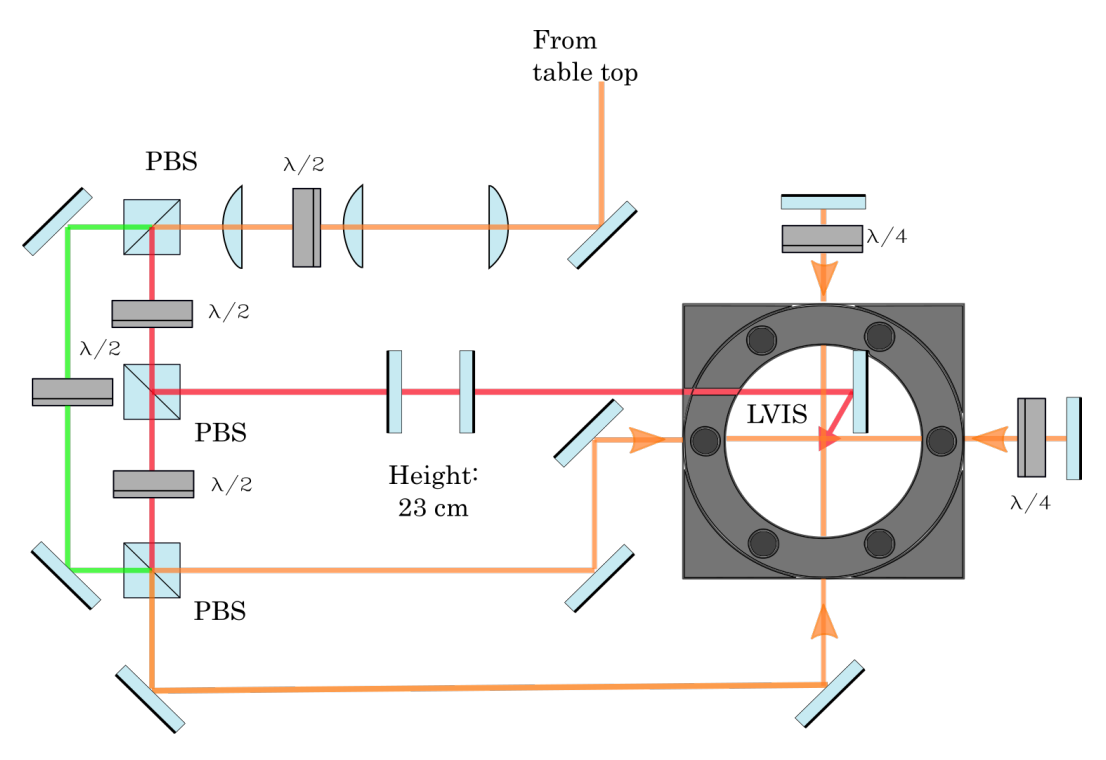


**Figure 2.8:** The optical alignment for the first MOT on the breadboard 54 cm above the optical table.

# 2.2.4 Magnetic fields

There are two types of magnetic fields used in the experiment; a magnetic gradient to create the MOT and homogeneous compensation fields. These fields compensate for background magnetic fields which can alter the location of the magnetic centre of the trap. A small shift in the location may not necessarily prevent a MOT from loading; it may however prevent the first MOT from being in the correct position to load the LVIS. After obtaining the MOT in the first chamber, compensation coils were used to align the centre of the first trap to the LVIS beam. The coils have DC electric current running through them in the same direction, i.e. the Helmholtz configuration [48]. The size and orientation of the fields were set to optimise the MOT via the current of the coils. To create the magnetic field gradient for the MOT, a pair of coils wired in the anti-Helmholtz configuration is used, where the current runs through the coils in opposite directions. These produced a gradient of 8.5 G cm<sup>-1</sup>.

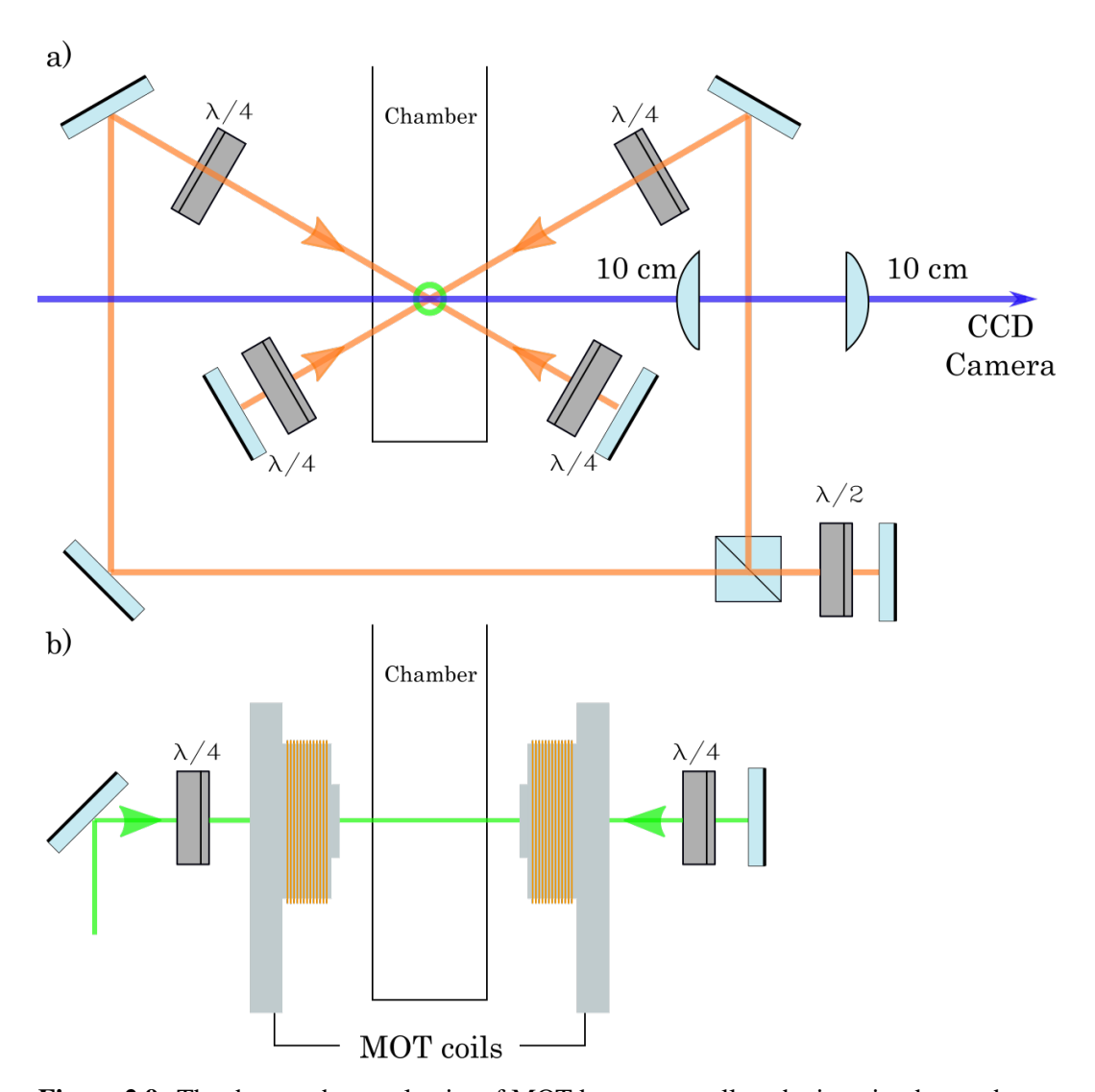


**Figure 2.9:** The three orthogonal pairs of MOT beams as well as the imaging beam shown from different views of the glass cell, a) shows a view along the axis of a MOT beam that goes straight through the cell whilst b) shows a view of the cell along the imaging beam's path. A circle indicates the beam is travelling into the page.

## 2.3 Procedure

## 2.3.1 MOT imaging

As the atoms in the MOT are being continuously excited by the cooling laser, they are continuously emitting fluorescence at a wavelength of 852 nm. To look for and monitor MOTs, this fluorescence can be captured by CCD cameras. This kind of imaging is useful for continuous and real time monitoring of the MOT, for example to see the decay of the second MOT when the LVIS beam is blocked. However, to take more detailed data about the MOT, absorption imaging is used. For this technique, a beam with a resonant frequency is shone on the atom cloud and is detected by the CCD camera. The atoms interact with the photons in the beam, so the image received by the camera is actually a shadow of the atom cloud in the imaging beam. The atoms' absorption is then calculated by subtracting background images from the image with the atoms cloud. The first background image is taken when atoms are not present (ensured by removing the gradient field), but the MOT beams are still active. This takes fluctuations in the beam power into account. The second background image is taken without the MOT beams, so as to eliminate any background light.

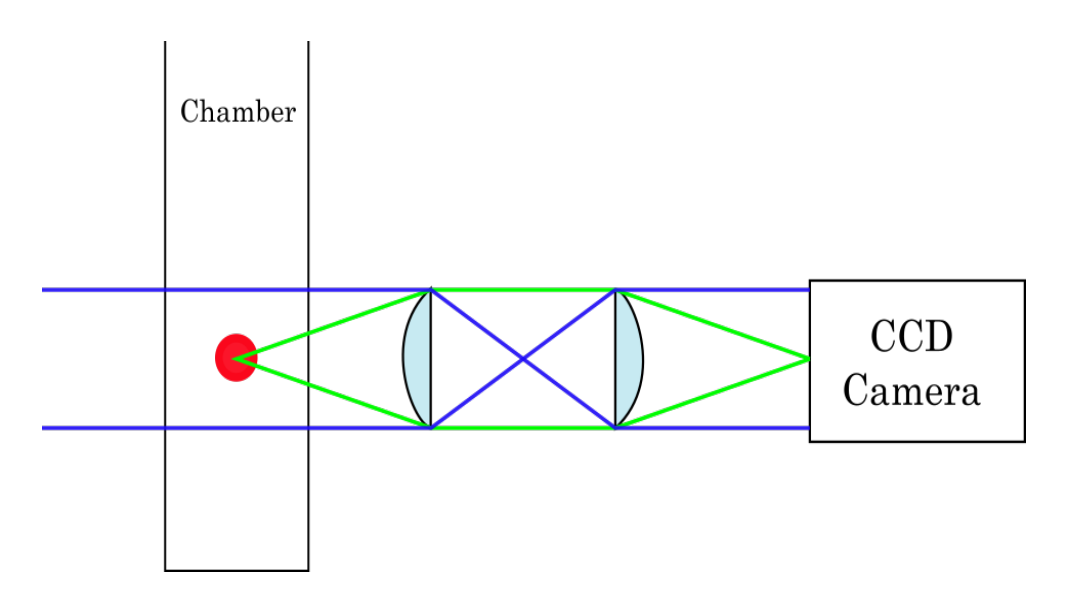


**Figure 2.10:** Diagram showing the path of the imaging beam through the lenses as well as the path of fluorescence to the CCD camera. The imaging beam is shown in blue, and the fluorescence in green.

The lens arrangement shown in Figure 2.10 enables the same camera to be used for both fluorescence and absorption imaging. For the former, light emanates from the MOT and will be collimated by the first lens and focused onto the camera by the second. For the latter, the imaging beam passes through the chamber as a collimated beam, is focused by the first lens and collimated by the second.

## 2.3.2 Measurement protocol

The experiment is executed using a LabVIEW (Laboratory Virtual Instrumentation Engineering Workbench) program, which controls whether the MOT and imaging beams were incident on the chamber using mechanical shutters. They also control the radio frequencies supplied to the AOMs, and thus the detunings provided by them. The program takes data for the characterisation of the second MOT. The program allows for the variation of certain parameters for a MOT and imaging sequence- loading time, detuning of cooling beams, detuning of imaging beam and the Time of Flight (TOF). The loading time is the amount of time the MOT is left to gather atoms from the LVIS, and it is controlled by closing the shutter for the first MOT beams. The detunings are controlled by varying the radio frequency supplied to the double passed AOM in the cooling laser's spectroscopy. The TOF is the amount of time left between releasing the atom cloud (MOT beams and magnetic field being turned off) and the initiation of the absorption imaging sequence. The imaging sequence is shown by Figure 2.11.

## 2.4 Characterisation of the MOT

The MOT was obtained in the second chamber, with a pressure of  $4 \times 10^{-9}$  mbar. As this is not a low enough pressure to be able to obtain a BEC, a rudimentary characterisation of the MOT was carried out, before work on the vacuum was done.

#### 2.4.1 MOT lifetime

Data regarding the lifetime of the MOT in the science chamber was taken by allowing the MOT to saturate (i.e. to reach its maximum fluorescence level), and then blocking the LVIS to stop the loading of the atoms. The cooling laser detuning used for this data was  $-2\Gamma$ . The dynamics of the population of a MOT with no loading

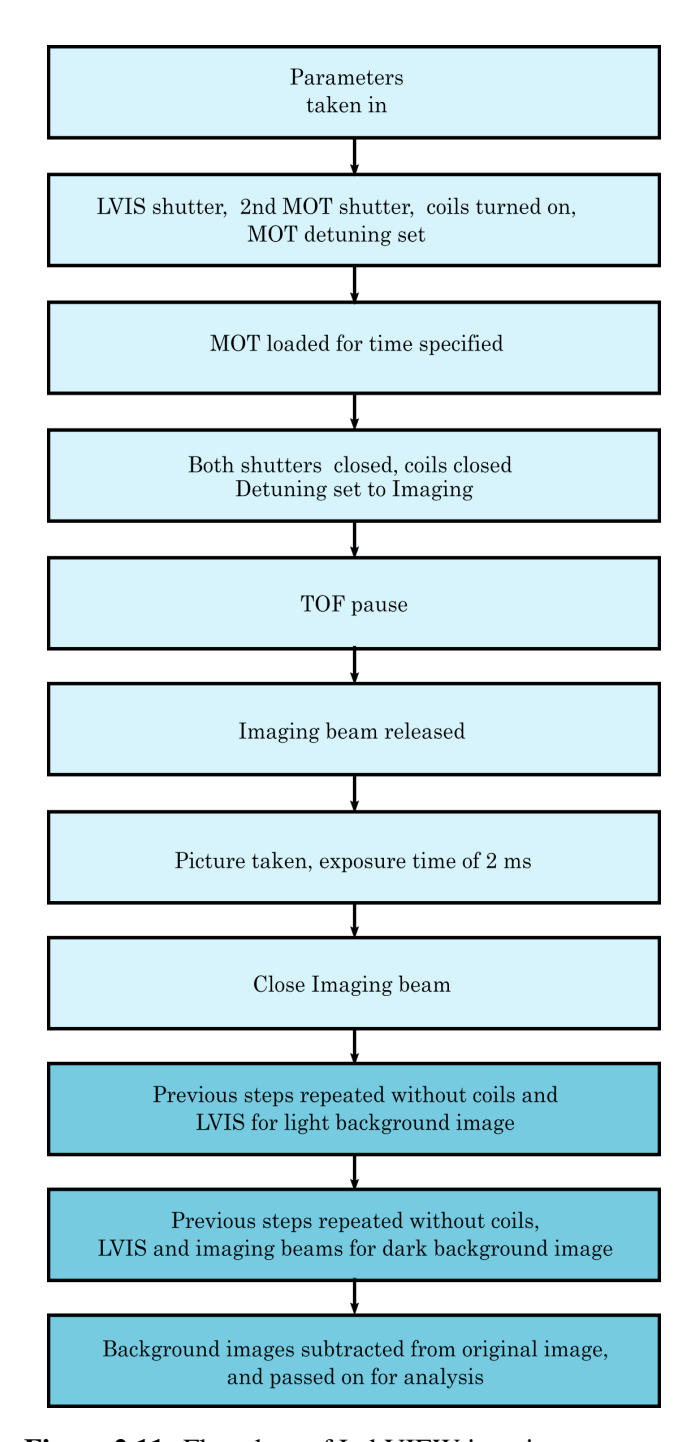


Figure 2.11: Flowchart of LabVIEW imaging sequence.

can be expressed as in Equation 2.5 [49]

$$\frac{dN}{dt} = -\gamma N - \beta \int_{V} n^{2}(r,t)d^{3}r \qquad (2.5)$$

where N is the atom number, t is the time elapsed since the loading of the MOT stopped,  $\gamma$  is the coefficient for the loss rate due to background collisions,  $\beta$  is the two-body collisional coefficient, V is the volume of the MOT, n(r,t) is the density of the MOT, and r is the radius of the MOT.

There are three regimes of MOT dynamics, and the type of dynamic a MOT will have is largely dependent on the population of the MOT [50]. The first regime is the constant volume regime, where the MOT cloud's volume remains constant, and the density increases as atoms are loaded into the MOT. This is typical for MOTs with a small number of atoms,  $<10^4$  [50]. As atoms are loaded into a MOT, the density will hit a maximum, and at this point the volume of the MOT will increase as atoms are loaded into the trap [51]. This regime is known as the density limited regime, where the density of the cloud is constant. It has been shown to apply to MOTs with a population of  $4-8 \times 10^4$  [52],  $10^5$  [53] and  $10^6$  atoms [50]. The third regime is the two-component regime, where the MOT has a dense central region to the MOT and less dense outer regions. This is caused by the volume of the atom cloud expanding past the central, strongly confining region of the MOT. This region comes about as a result of the restoring force in a MOT not being linear function of position [50].

In the constant density regime, the solution to the above Equation 2.5 is shown in Equation 2.6 [54]

$$N = N_0 e^{-(\gamma + \beta n_c)t} \tag{2.6}$$

where  $N_0$  is the initial atom number and

$$\frac{1}{\tau} = (\gamma + \beta n_c) \tag{2.7}$$

where  $\tau$  is the MOT lifetime. This means that the decay of a MOT can be fitted

with a single exponential decay. Figure 2.12 shows the data collected, and Figure 2.13 shows an example fitting of the data with the form of Equation 2.6. Though the y-scale has not been calibrated to give the number of atoms, this would only affect the  $N_0$  parameter. By fitting the individual lifetime measurements, and averaging the values, a MOT lifetime of  $\tau = (3.5 \pm 0.4)$  s is found. The uncertainty given is the standard deviation on the mean. However, it can be seen that this exponential form doesn't fit the data well, leading to the conclusion that the assumption made in Equation 2.6 does not hold true for this data.

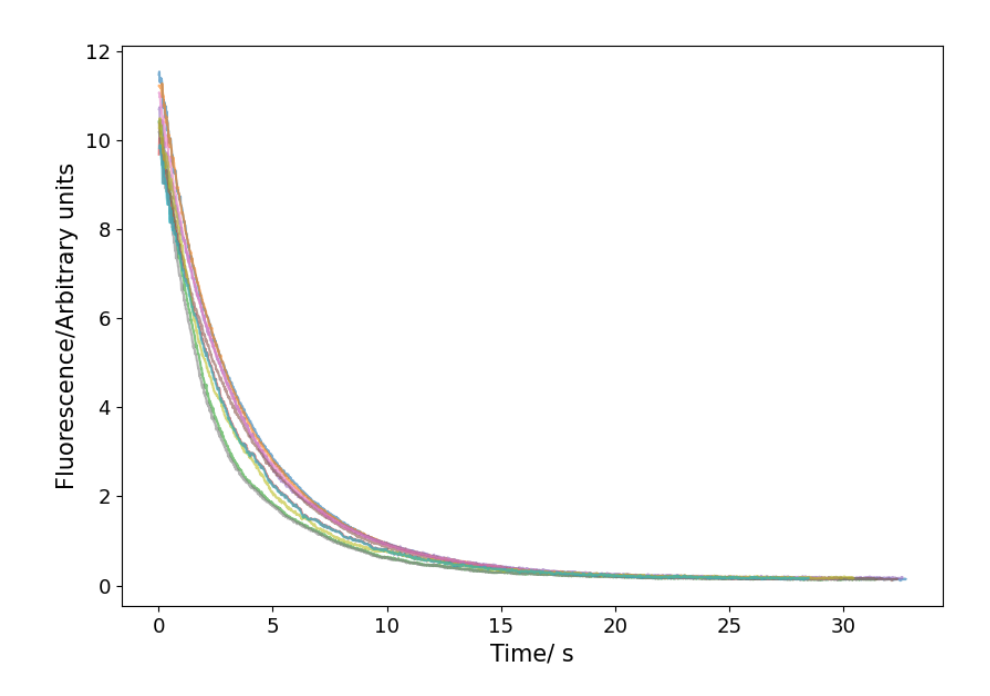
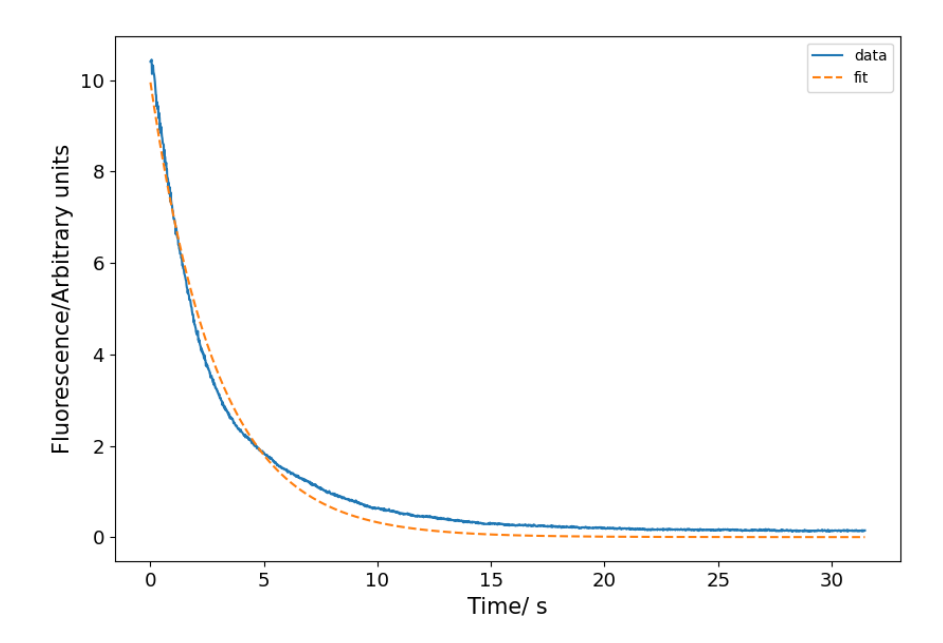


Figure 2.12: Decay of MOT fluorescence for the measurements of the MOT lifetime.

However, this assumption only affects the contribution of two-body collisions to te loss rate of the MOT. The exponential term due to the background collisions will still be present. It was found that the best fitting function was a dual exponential function, as shown in Equation 2.8.

$$N = N_1 e^{-\gamma t} + N_2 e^{-\beta' t} \tag{2.8}$$

 $\beta'$  has been used to indicate a decay constant associated with  $\beta$  the two-body col-



**Figure 2.13:** An example of the fitting of a single exponential decay to the MOT population decay data. The data is shown in solid blue, and the fit is shown in dashed orange.

lision coefficient. Since the fluorescence scale is not calibrated, the constants  $N_1$  and  $N_2$  are not themselves indicative of anything. However in this dual exponential function, the ratio of these constants will show which contribution to the loss rate is more dominant. The ratio of  $N_1/N_2 = 6.5$ , so  $\tau_1$  has the more dominant effect on the overall MOT lifetime.

For this function, the average parameters are  $\tau_1 = 1/\gamma = (2.7\pm0.5)$  s and  $\tau_2 = 1/\beta' = (12\pm2)$  s.

The lifetime of the MOT can be related to the background pressure by Equation 2.9 [55].

$$\frac{1}{\tau} = 3.3 \times 10^{16} P \sigma_b v_b \tag{2.9}$$

In the cited paper, the background pressure and the MOT lifetime are used to calculate a combined value of  $10^{-9}$  cm<sup>3</sup> s<sup>-1</sup> for  $\sigma_b v_b$ , where  $\sigma_b$  is the cross section for non-alkali background particles to knock an atom from the trap, and  $v_b$  is the thermal velocity of the gas. For  $\tau_1$  and a recorded pressure of 4 x  $10^{-9}$  mbar,  $\sigma_b v_b$ 

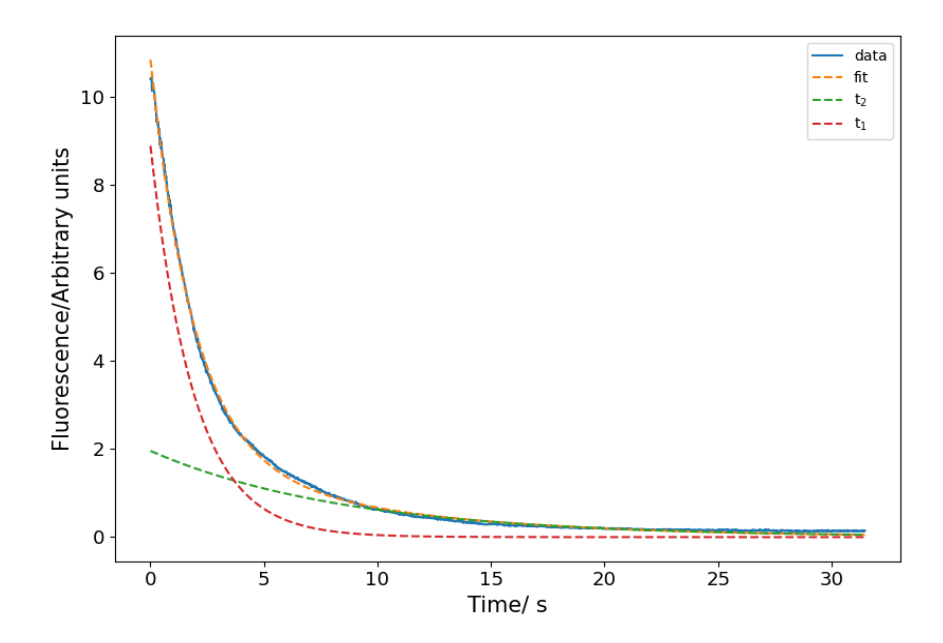


**Figure 2.14:** An example of the fitting of a dual exponential decay to the MOT population decay data. The data is shown in solid blue, and the fit is shown in dashed orange. The two components of the dual exponential function are also plotted.

= 2.8 x  $10^{-9}$  cm<sup>3</sup> s<sup>-1</sup>. This consistency with the value stated in [55] indicates that this component of the dual exponential function is indeed due to background gas collisions. By contrast, using  $\tau_2$  in Equation 2.9 gives  $\sigma_b v_b = 6.3$  x  $10^{-10}$  cm<sup>3</sup> s<sup>-1</sup>.

A possible reason for the exponential shape of the two-body collision contribution that differs from the background collision is that as atoms are lost from the trap, the dynamics of the MOT come closer to the constant density regime. As atoms are kicked out of the trap, the volume of the trap will shrink, till eventually the entirety of the trap is once again contained within the central strong trapping region, at which point the MOT dynamics will behave in accordance with the constant density regime.

#### **2.4.2 MOT** size

The analysis for the absorption imaging data is carried out by LabVIEW with the help of some integrated MATLAB (MATrix LABoratory) scripts. The MOT size is obtained by summing the values of the images pixel rows along the x- and y-

axes. This gives a Gaussian shape as defined in Equation 2.10, which is fitted by the MATLAB program.

$$f(x) = ae^{-\frac{(x-b)^2}{2c^2}} (2.10)$$

This outputs the parameters of the fit: a, b, and c, which is taken as the size of the MOT along the x- and y-axes.

### 2.4.3 Number of atoms

As the imaging beam passes through the atom cloud, the atoms absorb part of the beam. The intensity of the imaging beam after interacting with the atoms is given by Equation 2.11, known as the Beer-Lambert Law [56].

$$I = I_0 e^{-OD} (2.11)$$

where OD is the optical depth,  $I_0$  is the initial intensity and I is the intensity measured after the interaction with the atomic cloud. If the intensity of the imaging beam is less than the saturation intensity for the cooling transition ( $I_{sat} = 2.70 \text{ mW} \text{ cm}^{-2}$  [20]), the optical depth can be written in terms of the atomic column density, n(x,y), of the cloud as in 2.12 [56]. The atomic column density is the density along the directions perpendicular to the imaging beam, here referred to as x and y.

$$OD = -n(x, y)\sigma \tag{2.12}$$

where  $\sigma$  is the absorption cross section is given by Equation 2.13 [20].

$$\sigma = \frac{\sigma_0}{1 + 4(\frac{\delta}{\Gamma})^2 + \frac{I_0}{I_{Sat}}} \tag{2.13}$$

 $\sigma_0$  is the cross-section of absorption for a beam that is on resonance, and is shown in 2.14 [20].  $\delta$  is the detuning of the imaging beam.

$$\sigma_0 = \frac{\hbar \omega \Gamma}{2I_{sat}} \tag{2.14}$$

OD is given by Equation 2.15 [56].

$$OD = ln \frac{I_{light} - I_{dark}}{I_{atoms} - I_{dark}}$$
 (2.15)

where  $I_{light}$  is the intensity of the 'light' background picture,  $I_{dark}$  is the intensity of the 'dark' background picture and  $I_{atoms}$  is the intensity due to the atoms.

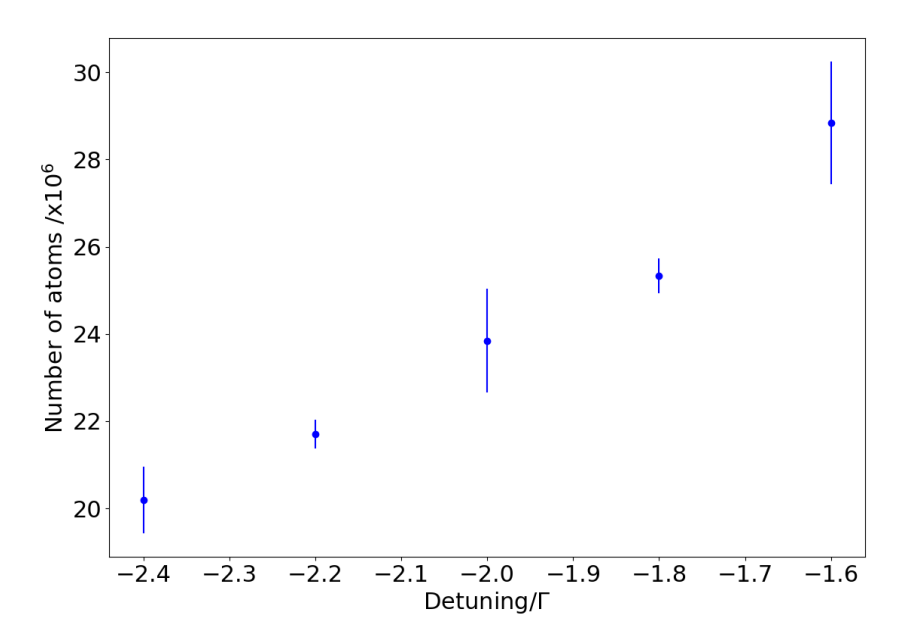


**Figure 2.15:** Number of atoms trapped in the MOT for TOF = 4ms, as it varies with the detuning of the MOT beams.

The number of atoms can be found by integrating the atomic column density across the x- and y-axes, as below in Equation 2.16 [56]. In an image, this is equivalent to assessing the optical density of the cloud in each pixel and summing over all pixels.

$$n = \int_{\infty}^{-\infty} \int_{\infty}^{-\infty} n(x, y) \, dx dy = \frac{1}{\sigma} \int_{\infty}^{-\infty} \int_{\infty}^{-\infty} OD \, dx dy$$
 (2.16)

The number of atoms data in Fig. 2.16 is obtained by taking 10 measurements of the number of atoms in a cloud for a given detuning, and taking the mean of those results, with the standard deviation being the uncertainty in that data.

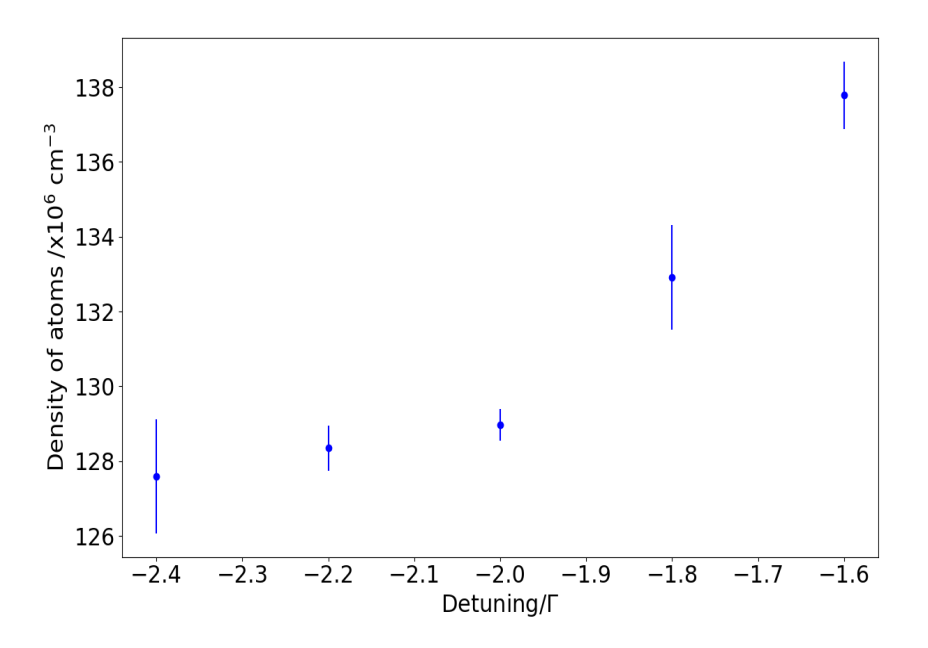


**Figure 2.16:** Density of the atoms trapped in the MOT for TOF = 4ms, as it varies with the detuning of the MOT beams.

The density of the atom cloud is then found by dividing this by the volume of the cloud. This is an ellipsoid with radii of  $\sigma_x$  and  $\sigma_y$ .  $\sigma_z$  is taken to be equal to  $\sigma_y$ , as these are both perpendicular to the axis of the MOT coils.

$$V = \frac{4}{3}\pi\sigma_x\sigma_y^2\tag{2.17}$$

The uncertainties in this data are found by propagating the uncertainty in the number of atoms, the uncertainty in  $\sigma_x$ , and the uncertainty  $\sigma_y$  - which is used as the uncertainty in  $\sigma_z$ . The propagation is carried out using the uncertainty propagation formula for independent variables.

## 2.4.4 Temperature of MOT

The temperature of a MOT is measured by allowing the atom cloud to expand freely, i.e. with the MOT beams blocked and the MOT coils turned off. The method by which the cloud expansion is linked to its temperature is shown here [56]. By taking images with different times of flight, the expansion of the cloud over a time period can be recorded, as shown by Figure 2.17. By assuming the atomic cloud obeys

Boltzmann's statistics, the probability of an atom having energy  $E_i$  at temperature T is

$$p_i = \frac{1}{Z} exp\left(-\frac{E_i}{k_B T}\right) dE \tag{2.18}$$

Z is the partition function, and  $k_B$  is Boltzmann's constant. This assumption can be made as atoms in a MOT are from a thermal distribution in the MOT. Multiply this by the number of atoms in the MOT, N

$$n_i = \frac{N}{Z} exp\left(-\frac{E_i}{k_B T}\right) dE \tag{2.19}$$

and the mean number of atoms at energy  $E_i$  at T is found,  $n_i$ . As the expansion of the atoms can be monitored, Equation 2.19 must be expressed in a suitable parameter-velocity. Assuming the motion of the atoms trapped in the MOT can be described classically, the kinetic energy is given by

$$E_k = \frac{1}{2}mv^2 (2.20)$$

As the expansion of the cloud in the x- and y-directions will be monitored, velocity is simply  $v = \frac{x}{t}$ , and is used to give Equation 2.19 as

$$n_i = \frac{Nmx^2}{Zt} exp\left(-\frac{mx^2}{2k_BTt^2}\right) dt$$
 (2.21)

Equation 2.21 has the form of a Gaussian distribution, i.e.

$$f(x) = \frac{1}{\sigma\sqrt{2\pi}}exp\left(-\frac{x^2}{2\sigma^2}\right)dx$$
 (2.22)

The distribution of atoms within the atom cloud as it expands is also a Gaussian distribution, precisely because of the velocity of the atoms. It is therefore fair to equate the two as follows:

$$\frac{mx^2}{2k_BTt^2} = \frac{x^2}{2\sigma^2} \tag{2.23}$$

which are both the argument of the exponential in their Gaussian distributions. Re-

arrange to find  $\sigma$ , the radial dimension along a given direction (e.g., x or y)

$$\sigma = \sqrt{\frac{k_B T}{m}} t \tag{2.24}$$

where  $\sqrt{\frac{k_BT}{m}}$  is the gradient of expansion, easily rearranged to give T. Such an expansion is shown in Figure 2.17.

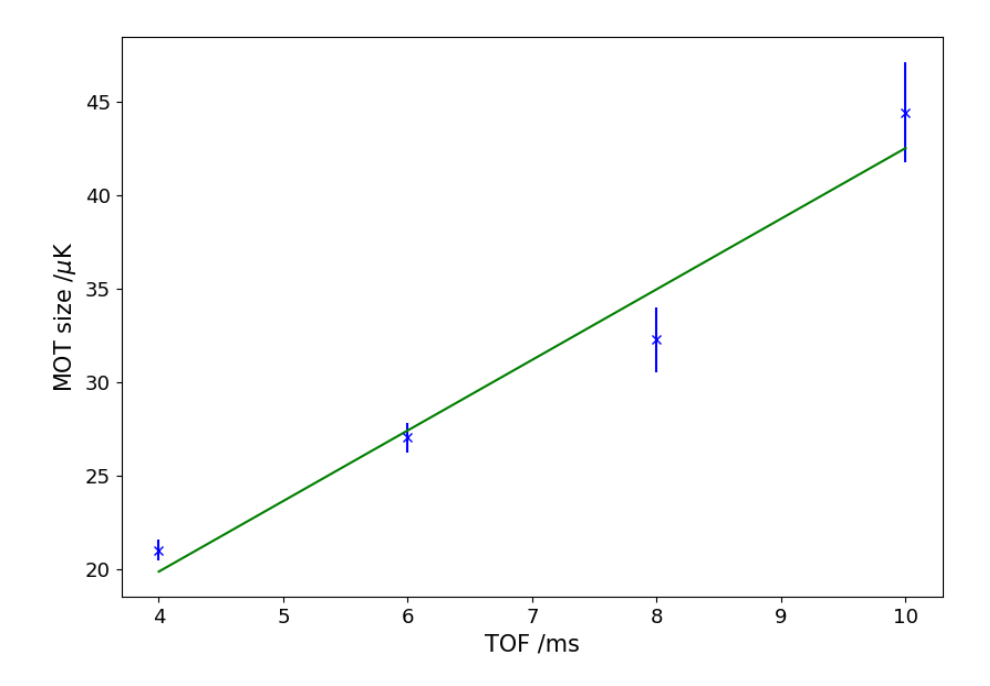


**Figure 2.17:** The size of the atomic cloud along the y axis during free expansion. The original atomic sample was obtained with a MOT loaded for 5 seconds, with a -2.2  $\Gamma$  detuning. This corresponds to a temperature of (60  $\pm$  5)  $\mu$ K

In Fig. 2.17, each TOF measurement was taken three times, and the standard deviation was taken as the uncertainty on the mean. A linear gradient was fitted to the cloud expansion, giving a temperature of  $(60 \pm 5) \mu K$ . Then to assess the fitting of the gradient, the reduced  $\chi^2$  was calculated as 1.72, indicating a good fit that is not over-fitted.

# Chapter 3

# **Caesium Isomer Trapping**

Here, the experiment focussing on the trapping of caesium isomers is discussed. The many different elements of the apparatus, dealing with isotope production, ion beam manipulation and laser cooling, are outlined. The instances where it is rather similar to the apparatus at UCL are not discussed at length. The progress of the experiment was hindered by the COVID-19 pandemic and damage to the apparatus, and the effects of this are also stated here. Details of repairs and updates that were made to the apparatus as a result of these hindrances are included here along with more in-depth descriptions of specific equipment. The results of the tests that were carried out to confirm the experiment was once again functional are shown.

# 3.1 Apparatus

An experiment that involves both high energy ion beams and laser cooling and trapping atoms requires the use of a large and diverse apparatus. It is best described by dividing it into two sections: the high energy section where the isotopes are produced and formed into an ion beam, and the low energy one, where the isotopes are neutralised and cooled using laser cooling techniques.

## 3.1.1 High energy apparatus

The University of Jyväskylä's accelerator laboratory, with its Ion Guide Isotope Separation On-Line (IGISOL) laboratory, is a facility for producing exotic species of radioactive atoms of interest for nuclear physics and for the work described here. It is shown in Figure 3.1 [57]. Nuclear reactions are induced in targets by the bom-

bardment of either light or heavy ions, in a K130 or MCC30 cyclotron. To produce caesium isotopes via fission reactions, the K130 cyclotron is used to bombard a natural uranium target with a 50 MeV proton beam.

The products of the reaction recoil into a gas cell filled with helium buffer gas. Roughly 1% of the products are thermalised and stopped by the gas. The electric charge of the reaction products allows for their complete control and manipulation into the ion beam. As the reaction products leave the gas cell, any neutral gas is removed by vacuum pumps. The ions however, are cooled and collimated into a beam by a sextupole ion guide and guided towards the high-vacuum mass separation area. Here, the ions are accelerated to an energy of 30 keV, and the desired mass to charge ratio is separated out using a 55° dipole magnet with a mass resolution,  $\frac{M}{\Delta M}$ , between 300 and 500.

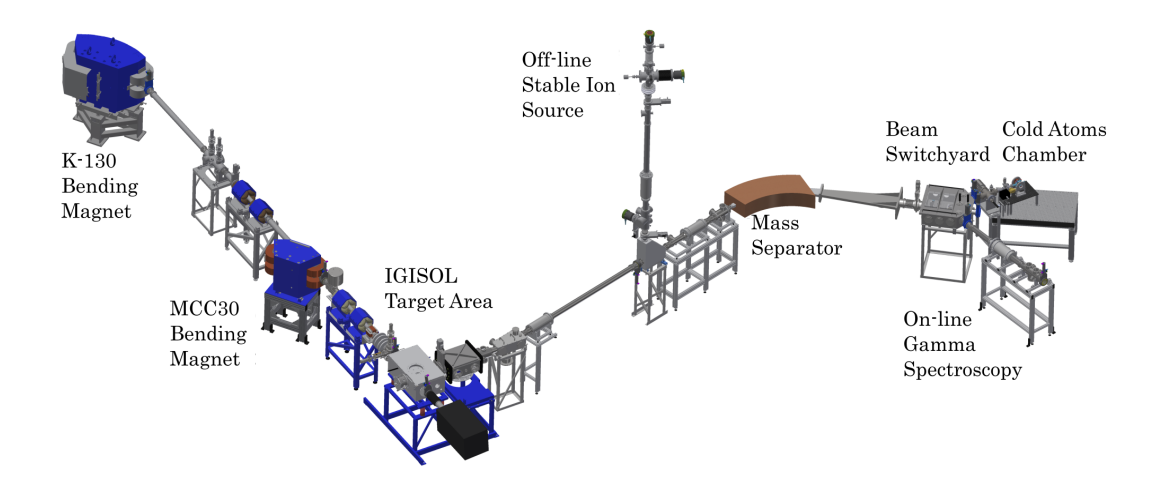


**Figure 3.1:** Diagram of IGISOL reaction area and beam line towards the cold atoms chamber.

## 3.1.2 Low energy apparatus

After the mass separator, the 'low energy' part of the setup begins, shown in Figures 3.2 and 3.3. It is separated by an UHV pneumatic gate valve. A set of electrostatic x-y plates are placed just before the gate valve. These steer the beam towards the trapping chamber. Just after the gate valve, there is an Einzel lens which focusses the ion beam onto a thin Y foil (the neutraliser, discussed in 3.1.3). A turbo-molecular

pump (Leybold CE TURBOVAC 350i) maintains the vacuum at  $\leq 10^{-8}$  mbar - even when the gate valve is suddenly opened.

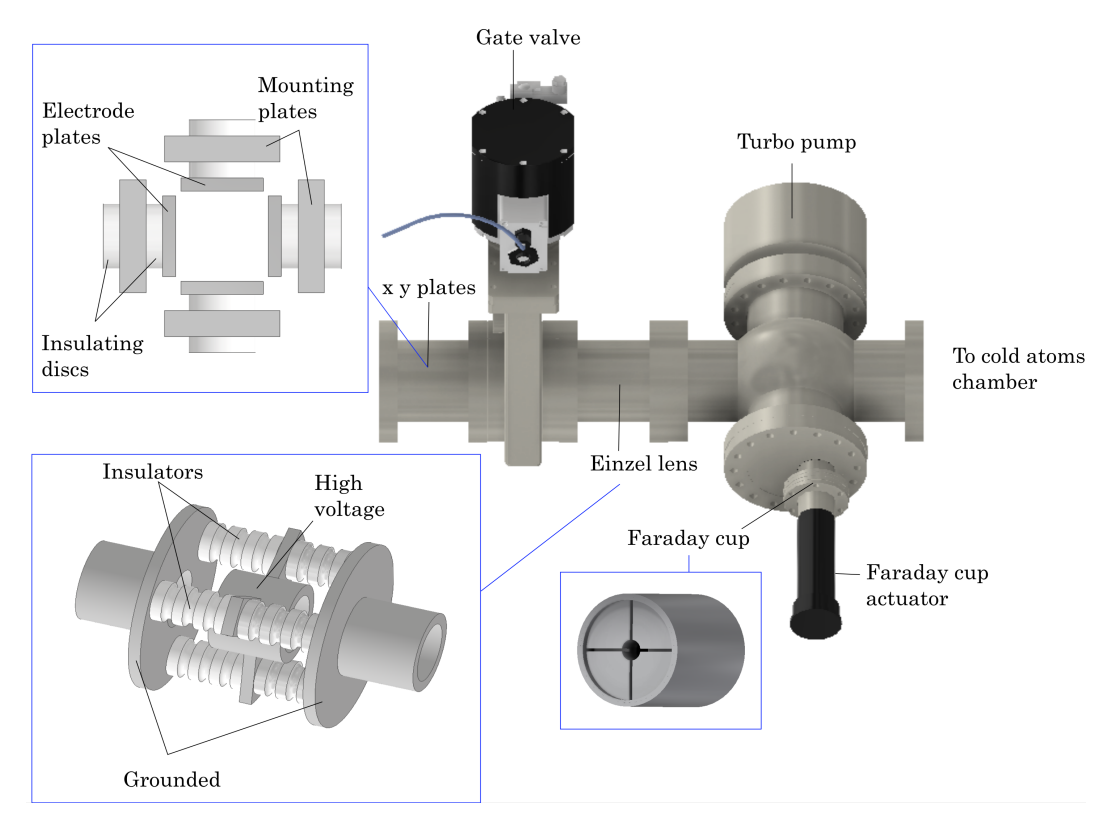


**Figure 3.2:** Bird's eye view diagram of high to low energy apparatus connection via a custom made CF 100 vacuum cross piece, with internal views of x y plates, Einzel lens and Faraday cup.

This vacuum pump is connected to the beam line via a CF 100 cross piece. The cross piece also connects a Faraday cup to the beam line, which measures the current of, and hence the amount of ions in, the beam. Finally, the cross piece is connected to the CF 40 section of the low-energy part of the apparatus via a reducer. This CF 40 section is shown along with the glass cold atoms chamber in Figure 3.3 [57].

Beyond the reducer, there is a 20 l/s, Varian VacIon Plus 20 Star-Cell ion pump to maintain the  $\leq 10^{-8}$  mbar pressure necessary for laser cooling. The ion pump is separated from the cold atoms chamber by a gate valve. This allows the vacuum to be broken in the chamber for maintenance while protecting the ion pump. This (alongside venting with  $N_2$  instead of air) means that the system can recover from

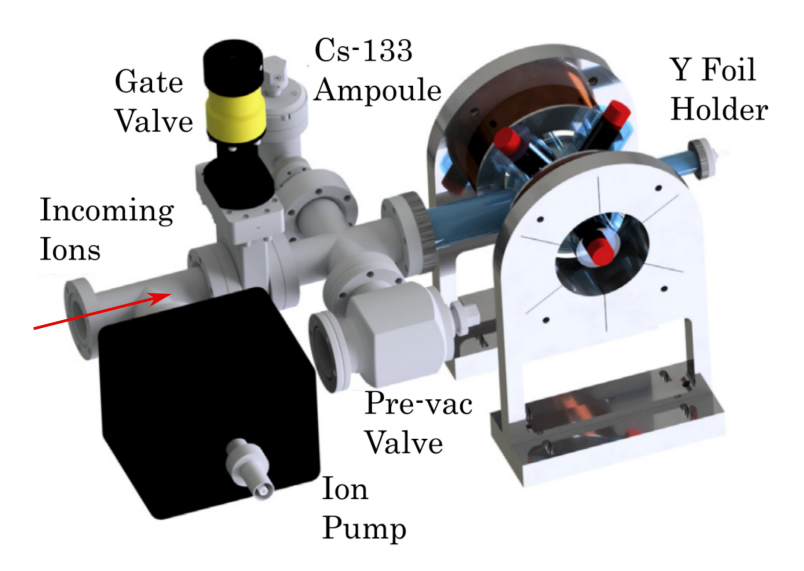


**Figure 3.3:** Cold atoms chamber, with laser beams going through optical windows shown in red, as well as MOT coils.

room pressure exposure within a matter of hours rather than days. After the gate valve, there is a  $^{133}$ Cs ampoule connected to a cross piece, controlled by an angle valve. This source of caesium is used to test the MOT settings of the system, such as beam alignment, the quadrupole field, etc. Also connected to the cross piece, is the valve through which nitrogen gas  $(N_2)$  is vented and preliminary pumping is done if the system needs to be opened.

#### 3.1.3 Ion neutralisation

The particles arriving in the science chamber are ions, and they must be neutralised prior to laser cooling. The ion beam is focussed onto a  $25\mu$ m thick yttrium (Y) foil, which is held on a mount 28 mm within the main 'sphere' of the chamber.

The mount (as shown in Figure 3.4) consists of copper supports that hold the foil. These are held in place by two 105.6 mm long hollow aluminium oxide (Al<sub>2</sub>O<sub>3</sub>) rods. The rods are secured to 20 A rated electrical feedthroughs in a CF 16 flange. Electric currents are run through the Y foil via copper core in the aluminium oxide rods. A centering ring is used to ensure that the Y foil is not under unnecessary tension, but it also allows for the expansion of the Y foil when heated.

After the Y foil split during operation in May 2018, I redesigned the copper

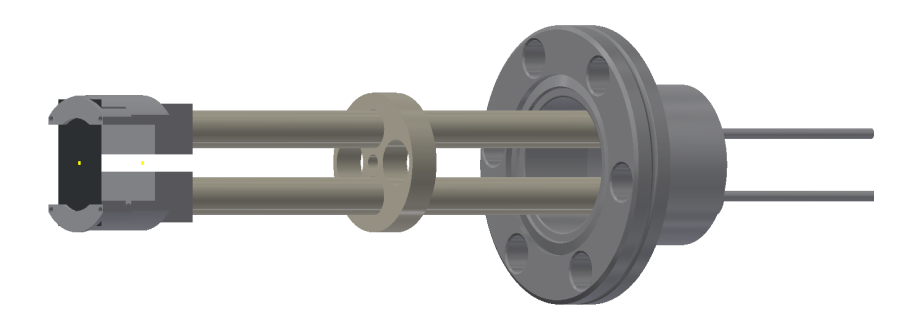


**Figure 3.4:** Diagram of neutraliser mount and connections that run current through the neutraliser. The connections were designed by Dr Luca Marmugi.

section of the mount to which the foil is attached. The previous design consisted of two copper 'D' shaped caps that were screwed into a copper base. This required the Y foil to be pierced to be mounted. The foil was also screwed into the mount tightly to provide a clamping force, which ensured electrical contact between the copper supports and the foil. Both the piercing and the screwing are thought to have damaged the foil to the point where the electrical contact became uneven and the heating was inhomogeneous. This led to the foil tearing and current no longer flowing. Another separate issue was that the caps that clamped the foil onto the copper mount once loosened and rotated while in the chamber, covering part of the foil available for ion implantation. To fix this the vacuum had to be broken.

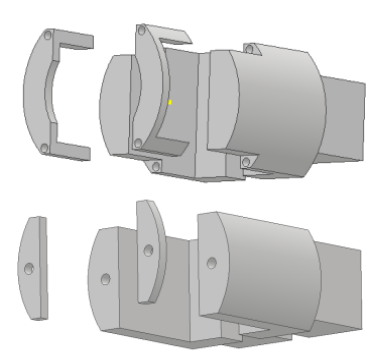


**Figure 3.5:** Diagram showing differences in the two neutraliser mount designs (new design on the top; previous on the bottom).

The new design featured two prongs on each copper cap, which prevents the caps rotating or falling, shown in Figure 3.5. The foil is held between each prong, which avoids piercing the foil, and the tight hold needed for electrical contact comes from the screwing of the prongs to the copper base. This design avoids the aforementioned problems. It was also compatible with the existing design from the  $Al_2O_3$  rods, in Figure 3.4.

The incoming ions are implanted into the yttrium foil. As this happens, the ions lose a large part of their kinetic energy via inelastic collisions within the yttrium lattice. Thermal diffusion is used to extract the caesium from the foil. A DC current is run through the foil via the copper core of the aluminium oxide rods  $(Al_2O_3)$  and the copper mount through to the foil. Diffusion from the foil is enhanced by an increase in its temperature, up to  $10^3$  K [57]. The ions gain an electron from the surrounding yttrium atoms and are neutralised, due to the caesium ionisation energy (3.89 eV [58]) being larger than the yttrium work function (3.1 eV [57]).

The caesium atoms that diffuse from the yttrium foil have temperatures in the range of  $600 \text{ K} \leq T \leq 1000 \text{ K}$ . These atoms are far too fast to be trapped by laser cooling techniques. However the atoms are able to thermalise through collisions with the chamber wall as a result of an organic coating used in the cold atoms chamber, as discussed in 3.1.4.

## 3.1.4 Cold atoms chamber

The chamber is spherical and made from borosilicate glass. There are three pairs of optical windows for laser beams, one CF 40 to glass connection from the transport line and a CF 16 connection for the neutraliser and its mount. One pair of optical windows is placed orthogonally to the beam line, and is the axis of the anti-Helmholtz MOT coils.

By using a glass chamber instead of a standard steel UHV chamber, coatings that increase the trapping efficiency of a MOT can be applied to the chamber. Such coatings reduce the adsorption energy of the chamber walls, meaning that fewer atoms are captured by the wall. Upon adsorption, the amount of time they are adsorbed to the wall, or the sticking time  $\tau_s$ , is reduced. The adsorption energy,  $E_a$ , and sticking time of a chamber wall are related to one another as shown in Eq. 3.1[59]

$$\tau_{\rm s} = \tau_0 \exp\left(E_a/k_B T\right) \tag{3.1}$$

T is the temperature of the surface and  $k_B$  is the Boltzmann constant. This refers to physisorption, where an atom is held to a surface by its image charge, which is a van der Waal interaction. Chemisorption on the other hand, is where the adsorption occurs permanently via a chemical reaction between a surface and the adsorbate.

The coating used in the chamber is polydimethylsiloxane (PDMS,  $CH_3[Si$   $(CH_3)_2O]_nSi(CH_3)_3$ ). This coating reduces the probability that an atom will be adsorbed to the chamber wall after colliding with it. Specifically, PDMS lowers the glass surface adsorption energy down to  $\sim 0.1$  eV, thereby reducing the sticking time of atoms onto the chamber wall and limiting- to a large extent- losses because of atom-wall collisions. In an experiment where the atoms being investigated may have a short lifetime and are in short supply, this is quite advantageous as more atoms will be available at any time. As mentioned above, the coating also helps to thermalise the atoms that come out of the yttrium foil at high temperatures. The thermalisation takes place via collisions with the chamber wall, and due to the presence of the PDMS coating, more collisions can occur without the atoms adsorbing to the chamber wall. The procedure by which the coating is applied to the chamber is described in Appendix C.

## 3.1.5 Optical alignment

The optical setup on the experiment is largely similar to the setup described in Section 2.2.3, with a few differences. On the laser table, the RadiantDyes Narrow-Diode cooling laser is split between two branches of alignment, spectroscopy for laser locking and amplification with the TA. Part of the RadiantDyes NarrowDiode repump laser is split off for spectroscopy, another small part is split off for the off-

set locking beat note and the rest is injected into an optical fibre for transport to the MOT table like the cooling laser. The difference between this alignment and what is shown in Chapter 2 is the inclusion of an ECDL as the slave laser for the repump offset locking scheme.

In general, the terms master and slave laser refer to the lasers in an arrangement where the frequency of the slave laser (often the more powerful of the two) is fixed in relation to the master (generally the one with a smaller linewidth). This can refer to injection locking, where stimulated emission is generated from the injection of the master laser into the slave laser [60]. However here, the slave laser is offset frequency locked to the master laser. The scheme is discussed in detail in Section 4.2.

After a telescope, the slave laser is split into two beams, one towards the fibre and the other to the offset lock's optical fibre. Here, the master and slave laser are combined at an NPBS before being injected into the offset lock fibre. Removing or adding the mirror marked with an asterisk in Figure 3.6 controls whether it is the repump master or repump slave laser going through the optical fibre to the MOT table.

The cooling and master repump lasers are brought to the MOT table via optical fibres. The cooling laser's polarisation is stabilised with a linear polariser as well as the half waveplate before the fibre. A small fraction of the beam is split off for the imaging beam. The rest is singly passed through an AOM at 80 MHz. After this it is combined with the repump beam at a PBS. The beams are enlarged and split up into three beams that will be retro-reflected as described in Chapter 2, except the last two beams are split up with an NPBS. The glass chamber was designed to have six optical windows for the three beams and their retro-reflections. However, the pyrex that makes up the main spherical body of the chamber distorts beams passed through it. Instead of having an imaging beam that takes a separate path to the MOT beams through the main body, the horizontal MOT beam and the imaging are combined at a PBS. Had a PBS been used to split the last two MOT beams, then

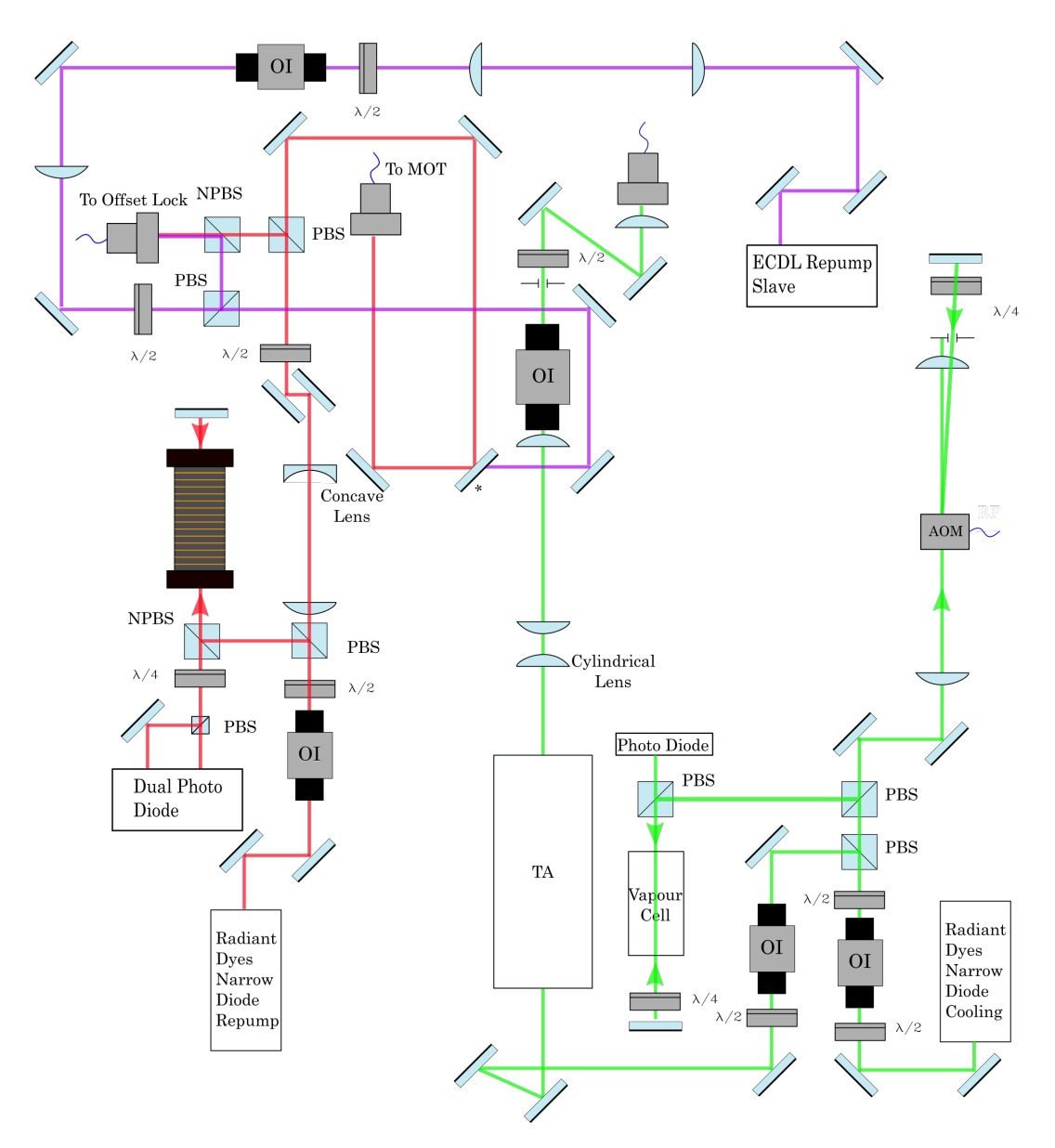


**Figure 3.6:** This figure shows the optical alignment of three lasers on the laser table. The cooling laser is shown in green. The repump laser is shown in red. The third laser is the slave laser for the repump laser offset locking scheme, shown in magenta.

the repump and cooling beams would have had orthogonal polarisations and would have been separated at the PBS combining the MOT and imaging beam. In Figure 3.8, the imaging beam is shown being separated out from the MOT beam using a PBS before the MOT beam is retro-reflected.

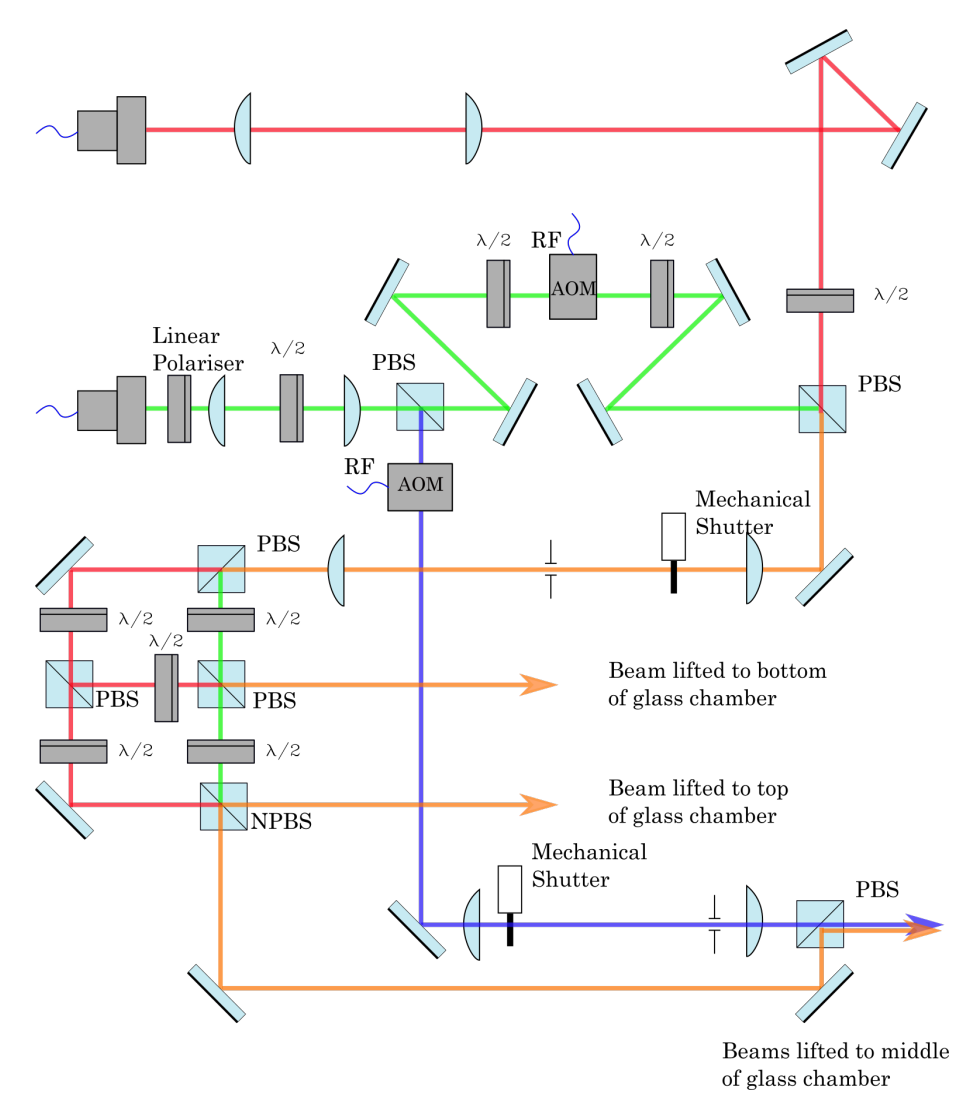


**Figure 3.7:** Optical alignment on the MOT table. Cooling laser is shown in green, repump in red and blue depicts the imaging beam. An orange beam indicates overlapped cooling and repump beams.

# 3.1.6 Magnetic fields

Like the apparatus in the UCL lab in London, there are three sets of compensation coils in the Helmholtz configuration (one for each axis) as well as a pair in anti-Helmholtz configuration for the MOT gradient coils. The water-cooled gradient

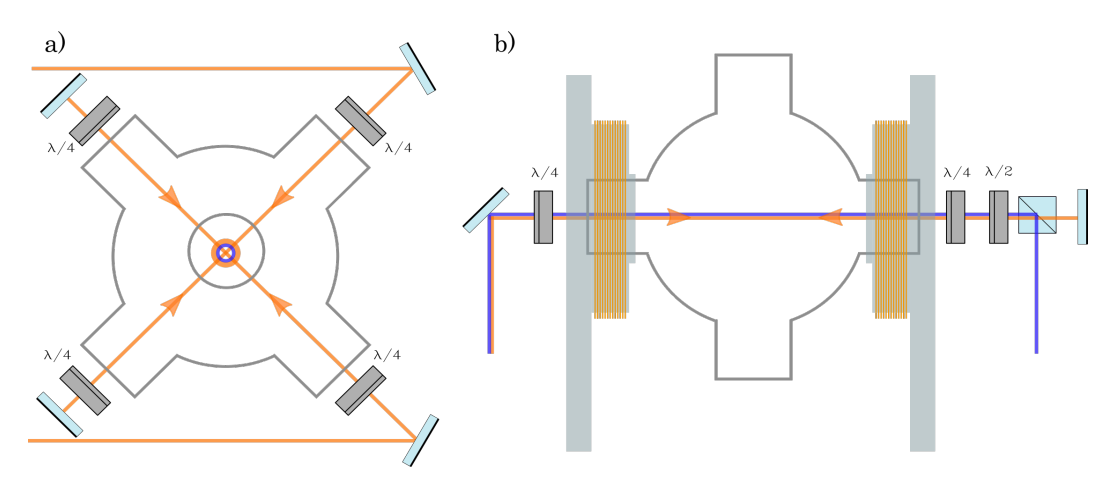


**Figure 3.8:** Optical alignment in relation to the glass chamber. a) shows the view of the chamber and beams along the axis of the gradient coils, and b) shows the view of the chamber along the axis of the ion beam. Orange beams indicate an overlap of the repump and cooling lasers, and blue indicates the imaging beam.

coils are operated at an optimised current of 1.86 A, giving a magnetic gradient of 14 G/cm, which is set and maintained with LabVIEW software via a MOSFET (IXFN 120N20) and a Proportional-Integral-Differential (PID) controller (SRS SIM960). The mounts for the coil also provide support to the glass chamber, as they are arranged along the axis perpendicular to the beam line in the horizontal plane (as seen in Figure 3.3). There is a small amount of foam between the mounts and the chamber.

## 3.1.7 Fluorescence imaging

The main imaging procedure used for this experiment is fluorescence imaging. As stated in Chapter 2, this is useful for detecting and monitoring MOTs. The CCD camera used is a PixelFly USB camera from PCO, with a PENTAX C2514-5M objective lens. In between the objective and the CCD camera, there is an 852 nm interference filter an a pinhole with a diameter of 1.6 mm. These features serve to reduce background light reaching the CCD camera.

Much information about a MOT can be learnt from a trace of a MOT's fluorescence in arbitrary units, as shown in Section 2.4. However, it is possible for the number of atoms in the MOT to be found from the fluorescence of the MOT (described in Appendix A), and this has been incorporated into a LabVIEW fluorescence imaging program. The program also continually subtracts a weighted background based on the fluctuations in the laser power. To this end, the program also monitors the power of the laser beams and displays this alongside the fluorescence trace. The LabVIEW program was written and developed by Dr. Luca Marmugi and Dr. Alexandros Giatzoglou.

#### 3.1.8 Offline caesium-133 ion beam

Due to the nature of a large scale facility like the IGISOL cyclotron being shared by many different projects, most of the time the apparatus described above will not have access to isotopes or isomers of caesium. It is at these times that the off line stable ion source depicted in Figure 3.1 can be used.

The offline beam source is situated just above the mass separator on the second floor of the IGISOL facility. Two stable sources can be used in this line: a surface source or a discharge ion source. The surface source contains a mix of potassium, rubidium and caesium atoms. The source element in the discharge source can be changed as needed, however this gives a beam of smaller current.

The surface source is heated to ionise the atoms and the ions are accelerated by a 30 kV potential difference as an isomer beam from the main cyclotron would be. In contrast to the main IGISOL beamline, the ions produced by the offline source are not of similar mass to charge ratios. This means that  $^{133}\text{Cs}^+$  ions are easily selected at the mass separator. After this, the  $^{133}\text{Cs}^+$  ions arrive at the beam switchyard and are steered towards the cold atoms chamber.

The offline source allows the experiment to be run with a beam <sup>133</sup>Cs<sup>+</sup> ions, the stable isotope for which the trapping and repump frequencies are known and can be locked to using <sup>133</sup>Cs vapour reference cells, as well as the known optimum detuning and MOT coil gradient. This means that the features of the apparatus geared towards taking an ion beam and producing neutralised atoms that can be trapped in a MOT can be thoroughly tested or optimised. This includes the PDMS coating, neutraliser, beam optics (Einzel lens and x-y plates), and the settings of the steering magnets in the switchyard. Being able to optimise these outside of

online beam time is useful. The efficiency of the beam from the switchyard to the neutraliser is also crucial for online beam time where every atom counts, and this can be tested with the offline source. Another logistical rather than scientific benefit to the offline source, is that it can be used directly after online beam time without needing to wait for a 'cooling' period.

# 3.2 Setbacks to the experiment

## 3.2.1 Power cuts and resulting damage

In early 2019, there were a series of large-scale power cuts, affecting not only the IGISOL facility but significant parts of Jyväskylä. This caused severe damage to the experiment. The laser controllers had been turned off in one of the power cuts, and when they were turned back on it was discovered that the RadiantDyes NarrowDiode cooling laser's temperature control circuit had been badly damaged. Specifically, the Peltier component that is used to heat or cool the laser diode was damaged. Unfortunately since this was a commercial laser, it had to be sent back to RadiantDyes in Germany for repairs, which took several months. Another laser damaged by the power cut was the slave laser for the repump offset lock. The ECDL had been setup in July 2018, but the laser diode was broken by the power cut.

The TA also suffered an issue with its cooling circuit. Unlike the Radiant-Dyes laser controllers, when power was restored, the temperature control (Thorlabs TED 200C) of the TA was turned back on. The Peltier element in the TA box was damaged in the power cut, and once the power was switched back on, it drove up the temperature of the TA box to well above 60 °C. While this would be fixed, a replacement TA and its controllers were shipped to Jyväskylä.

## 3.2.2 COVID-19 pandemic

Once the RadiantDyes NarrowDiode cooling laser was repaired and returned, repairs to the experiment were begun with a few short trips to Jyväskylä in late 2019 to early 2020. However once the COVID-19 pandemic began, international travel became severely restricted. In addition to this, the hosting of visiting students and

staff at the University of Jyväskylä was also monitored and applications for visitors from abroad had to be made, as well as risk assessments. And of course, the state of the pandemic in both Finland and the UK was a large factor in determining whether international travel to work on the experiment was feasible.

Two trips to Jyväskylä were made during the pandemic, the first was a month long, from mid November to mid December 2020. This was after the first wave of the pandemic in both the UK and Finland when restrictions were easing (despite the approaching second wave) and the university was open to considering visiting students. The second trip was from mid June to the end of August in 2021. The delay between the two trips occurred as a result of the second waves of the pandemic. The majority of the repair work presented in this chapter is the work carried out in these two trips.

# 3.3 Experimental repairs

## 3.3.1 Uninterruptible Power Supply (UPS)

To prevent any future power cuts causing damage to the experiment, an Uninterruptible Power Supply (UPS) was installed which will power the lasers, TA and the ion pump. The Sentinel Pro 1000ER UPS system from Riello was installed and is used with a extended runtime battery pack. This can support the lasers, the ion pump and the TA on the experiment for approximately 55 mins in the case of another power cut.

# 3.3.2 Vacuum system

A LabVIEW system was put in place to record and save the pressure measured by the ion pump, with the possibility of remote monitoring from London in mind. The LabVIEW program (developed for use at UCL by a colleague) reads the voltage outputted by the 4 UHV Agilent ion pump controller, which corresponds to a pressure measurement, shown in Figure 3.9.

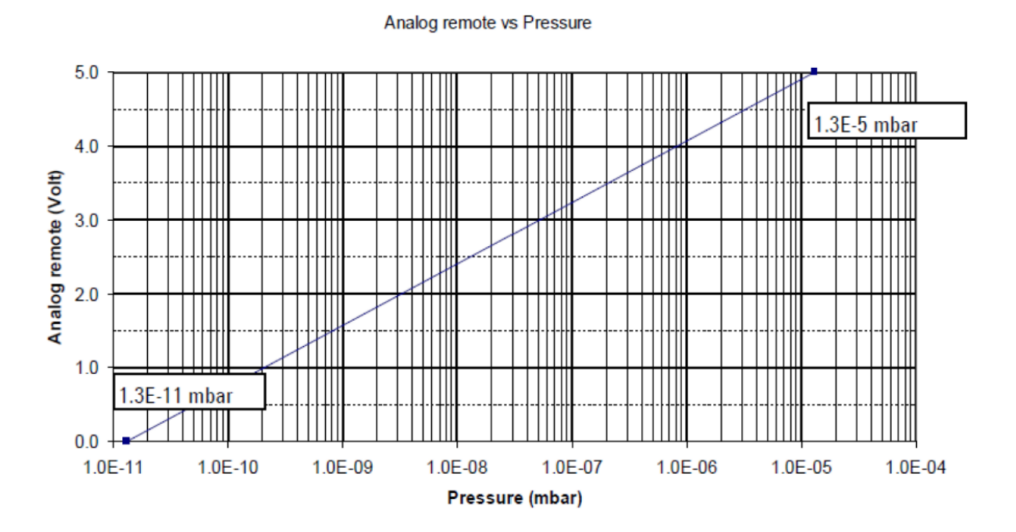


Figure 3.9: Voltage to pressure conversion of ion pump pump controller, [61]

## 3.3.3 Repump slave ECDL

The slave laser for the repump offset lock is an ECDL arranged in the Littrow configuration, as shown in Figure 3.10. The output of the laser diode passes through a lens for collimation, and is then reflected off of a diffraction grating. Due to the blazed grating, the first order reflection is reflected along the incident beam, and thus provides optical feedback for stimulated emission from the diode. A temperature sensor and Peltier element are included for control of the cavity temperature.

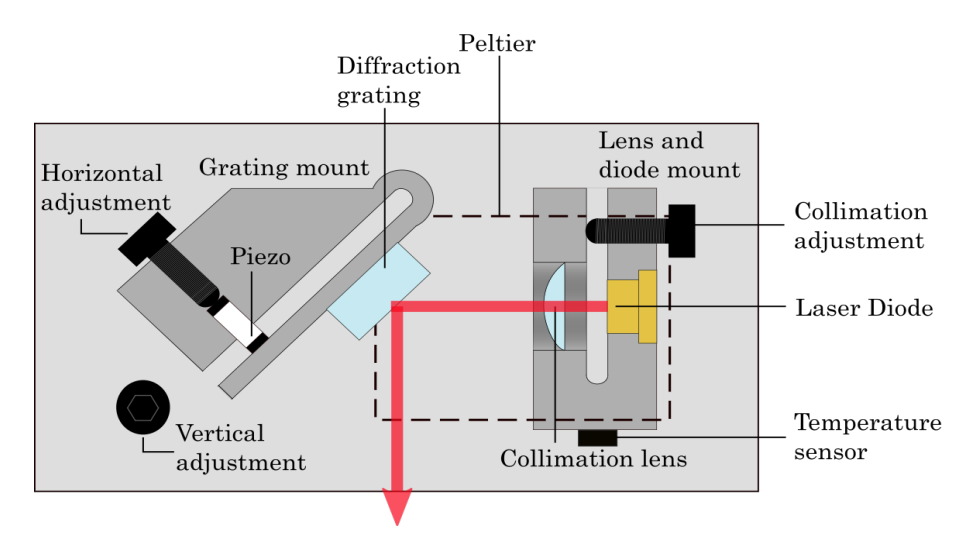


Figure 3.10: Diagram of repump slave ECDL in Littrow configuration

The zeroth order of the diffraction grating reflection is the output beam of the

laser. The diffraction condition of the beam is given by

$$n\lambda = 2d\sin(\theta_i),\tag{3.2}$$

where d is the distance between the grooves of the diffraction grating, and  $\theta_i$  is the angle of the incident beam. Hence, the wavelength of the laser can be tuned using the angle of the diffraction grating. This is done in two ways; the first and coarser method is the horizontal adjustment screw, which is manually turned. The second is a piezo placed such that the diffraction grating angle can be finely tuned with its expansion.

The broken diode was replaced. The alignment of the cavity was optimised by reducing the lasing threshold. This is the laser diode current at which the laser's output is dominated by stimulated emission rather than spontaneous emission. It is typified by a sudden increase in power output with increasing current. The threshold is lowered by optimising the alignment of the laser cavity. This is done by changing the vertical adjustment of the cavity, with the screw shown in Figure 3.10. The final threshold current of the laser is shown in Figure 3.11, a plot of the laser's output power against the current of the laser diode.

Then the manual setting of the diffraction grating was done using an IR viewer to observe strong fluorescence in a caesium vapour cell. After this, the optics after the laser were realigned, and then the laser was reinjected into the beat note detector for the offset lock, which is discussed in Chapter 4.

### 3.3.4 RadiantDyes NarrowDiode Cooling laser

Once the cooling laser's temperature control circuit was repaired at RadiantDyes and returned, it was reinstalled on the experiment's laser table. The laser itself is a different configuration to above, shown below in Figure 3.12

The light from the laser diode first passes through a collimation lens, then an interference filter, the angle of which determines the frequency of the output. There are two more (fixed) lenses for the collimation of the beam. Between those, the

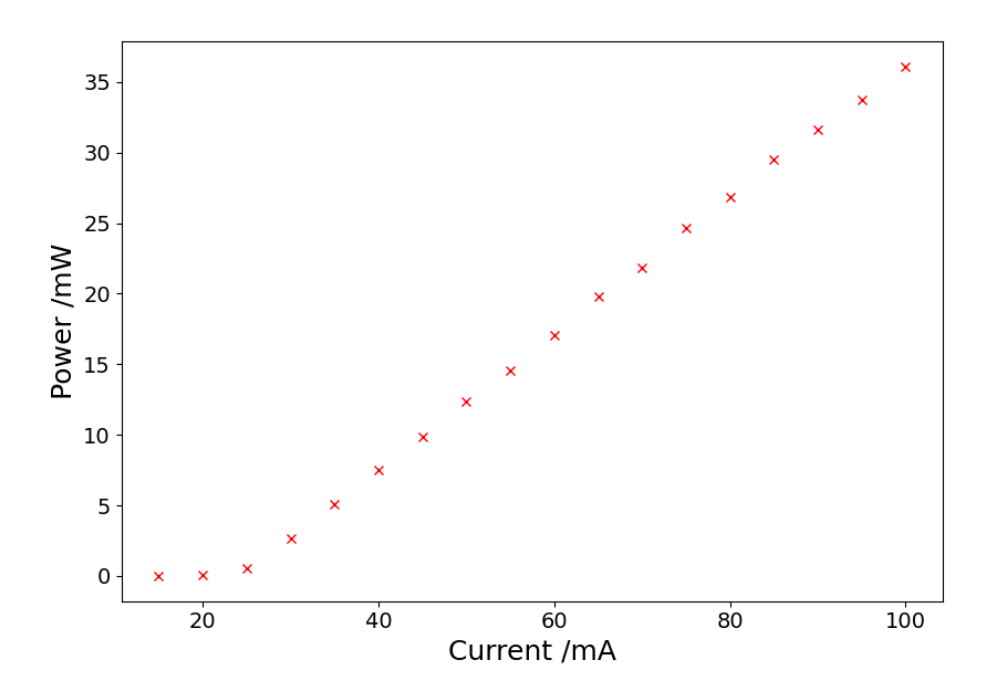


Figure 3.11: Current to the laser diode against the power output of the repump slave laser

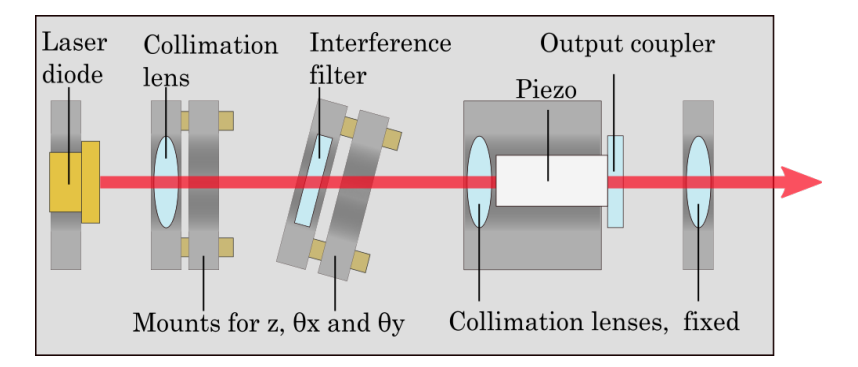


Figure 3.12: Diagram of RadiantDyes NarrowDiode laser cavity.

piezo is attached to the output coupler of the cavity, thus varying the length of the cavity for frequency variation.

After the installation, the laser cavity's back-injection needed to be optimised by lowering the threshold current as described previously. In this laser configuration however, the position of the first collimation lens was adjusted instead.

Then the alignment for both the spectroscopy and the TA seed beam preparation was redone. The term seed beam refers to an initial beam that is amplified. In addition to this, upgrades were made to the locking system, switching from DAVLL to a current modulation generated error signal, which affords more control over the error signal.

## 3.3.5 Tapered Amplifier (TA)

The TA chip is set up within a larger box, as shown in Figure 3.13. Before the seed beam reaches the TA (m2k-TA-0850-2000; m2k-laser GmbH), it passes through a Brewster window and a lens. A Brewster window is a piece of optical glass cut at Brewster's angle, so that the 100% transmission of p-polarised light that occurs can be exploited. Here, they are used to minimise reflections close to the TA that would otherwise interfere with the stability of the TA and affect the power throughput.

The lens focusses the seed beam onto the TA. The lens mount has five controls (shown in Figure 3.13). A and B change the x and y positions of the lens respectively. C and D change  $\theta y$  and  $\theta x$  respectively. Changing C, D and E together changes the lens' z position.

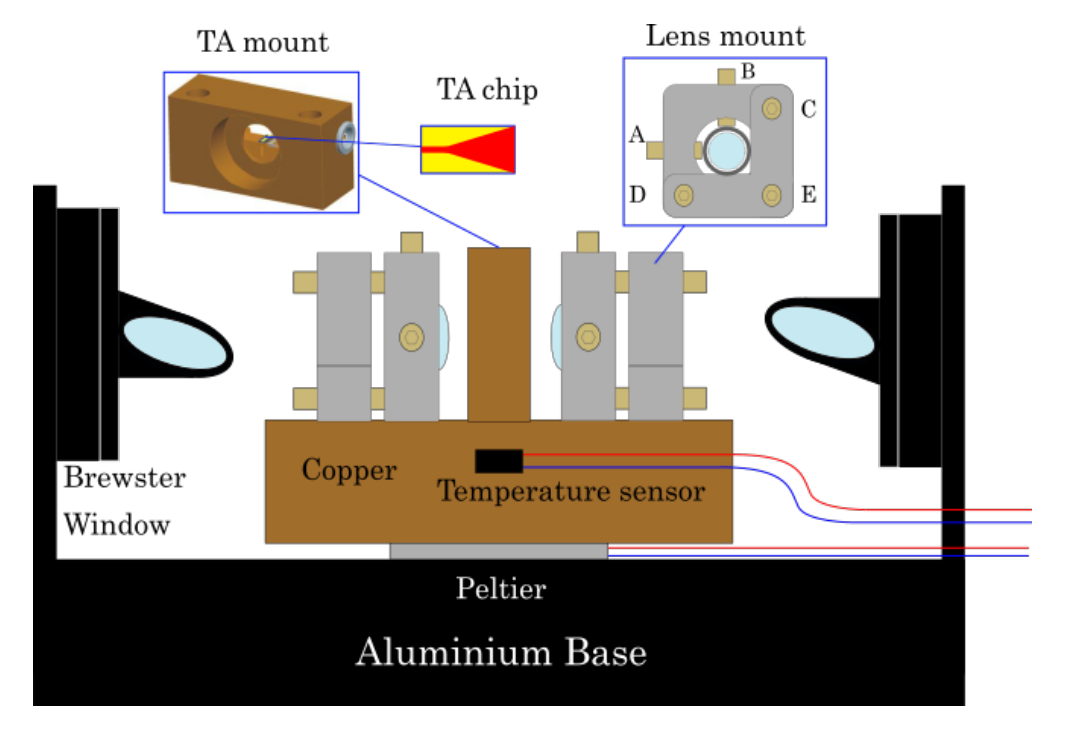


Figure 3.13: Diagram of TA chip and surrounding system. Inset of TA mount.

The TA chip is mounted in a DHP-F mount (Coherent, shown in Figure 3.13

inset [62]), which provides the connections for the current supply. This sits on a larger copper block alongside the lens mounts. The temperature of the TA chip is maintained via the copper block, with a temperature sensor (AD590) and a Peltier element (MCPE1-12707AC-S 55.6W; Multicomp).

The ideal position for the input lens was found by matching the size and shape of the spontaneous emission of the TA to the seed beam prior to aligning the seed beam to the chip. The seed beam was coupled to the chip using two mirrors at a low current of 1.5 A with a seed beam of 12.3 mW. The positions and orientations of the two mirrors were finely adjusted until amplification in the output power was seen and then optimised. The position of the output lens also affects the power output, so it was optimised by considering the amplification. The resulting output power of the TA for currents up to 2.5 A with a seed beam of 12.3 mW is shown in Figure 3.14.

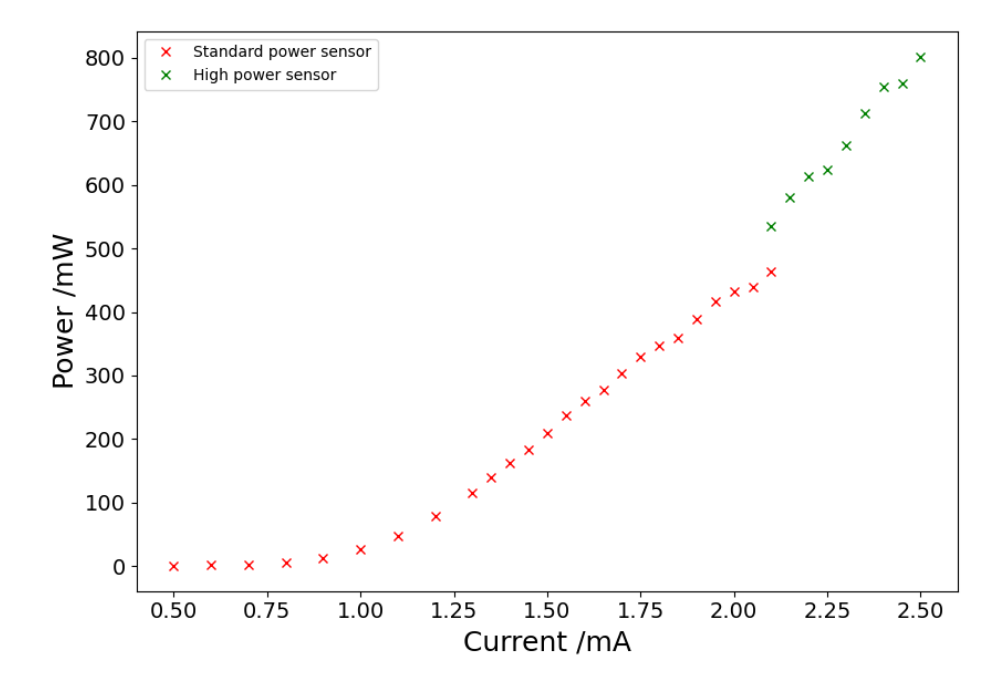


Figure 3.14: Current supplied to TA against the power output, for a seed beam of 12.3 mW

Once the injection of the seed beam was optimised, the collimation of the output beam was redone. The output lens, though optimised for power, is able to

collimate the output beam in the vertical axis. However, due to the nature of the TA, the output beam is far more divergent in the horizontal axis. To correct for this, a cylindrical lens is placed just after the TA box. Then a telescope was used to scale down the beam to a 1 mm width. These lenses are shown in the diagram of the optical alignment, Figure 3.6.

# 3.4 Testing of repaired experiment

Once the repairs to the experiment's laser system were completed, the experiment's functionality needed to be tested. This was done in two ways: first, a MOT was obtained from the caesium reservoir, then from the offline <sup>133</sup>Cs beam. Both are characterised using fluorescence imaging. The absorption imaging software had some issues, and since fluorescence imaging provided us with the information needed to be able to test the system and continue with developing the experiment, fixing the absorption imaging software was unfortunately not as high a priority.

## 3.4.1 MOT from caesium-133 vapour

Figure 3.15 shows an image of a MOT with a population of 175,000 atoms. Figure 3.16 shows the fluorescence level that is used to monitor the MOT population.

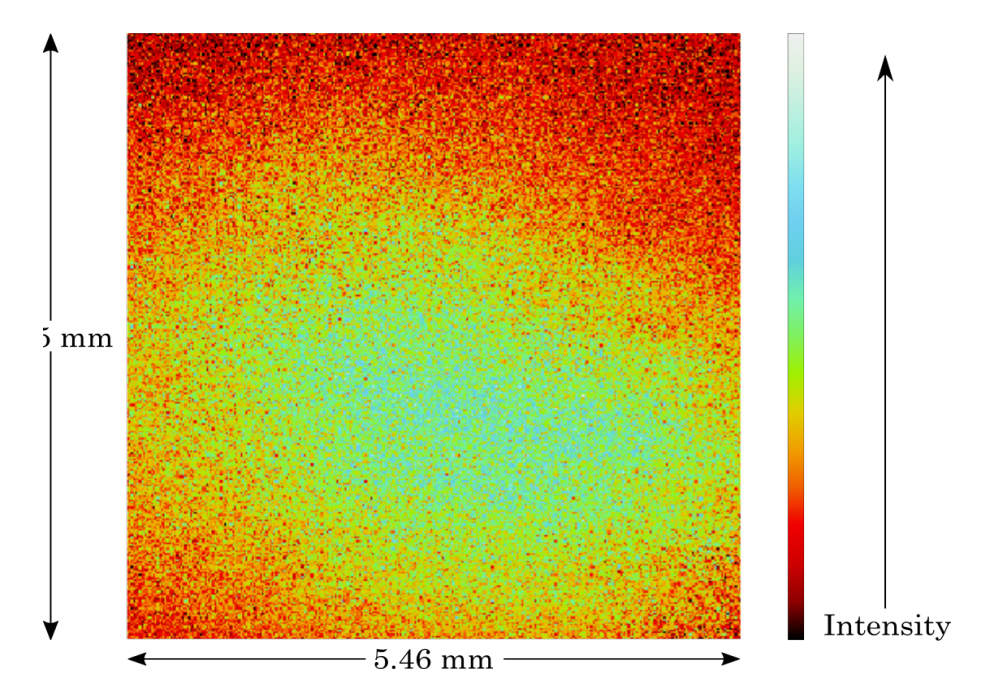
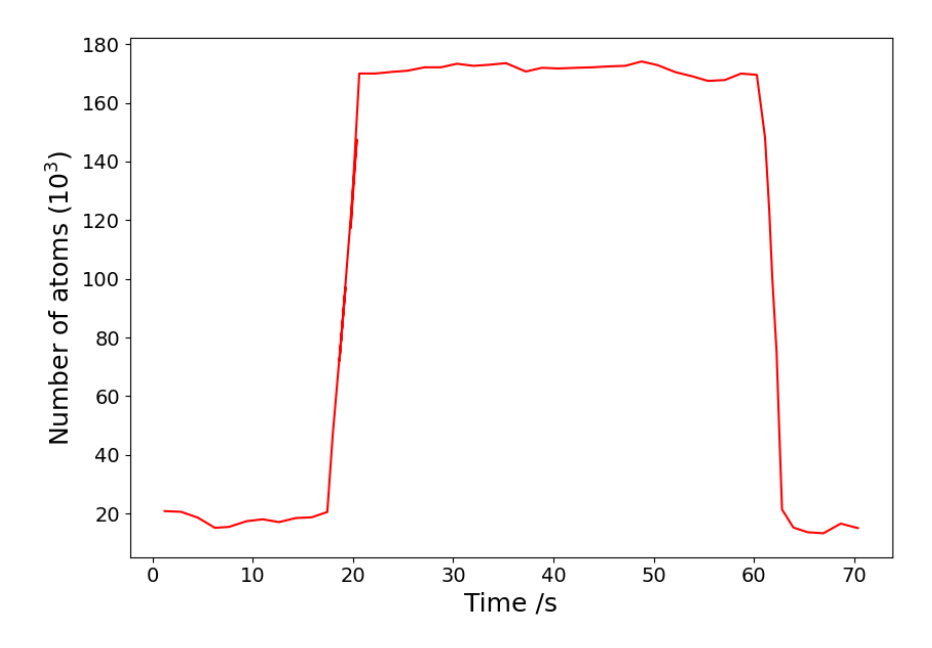


Figure 3.15: Colour-scaled image of MOT from caesium vapour.



**Figure 3.16:** Fluorescence of MOT captured from caesium vapour. Magnetic field turned on at 17 s and off at 60 s.

The figures were obtained after optimising the beam powers, polarisation, angles, gradient coils, compensation coils. Successfully obtaining a MOT from the caesium vapour from the ampoule reservoir verified that all components of the experiment, aside from the neutraliser and the PDMS coating, were functioning well. This includes the lasers, the locking of the lasers, the tapered amplifier, the conditions in the chamber, the gradient coils and compensation coils. In essence, all of the parts of the experiment that had been damaged and then repaired, amongst others.

#### 3.4.2 MOT from offline caesium-133 ion beam

During the power cuts, the cold atoms chamber was exposed to atmospheric pressure for long durations. It was therefore possible that the PDMS coating could have degraded. The fact that a MOT was obtained from the caesium ampoule does not assess the condition of the PDMS coating, as there are enough atoms available to simply overwhelm any number of adsorption sites that exist in the chamber and still have free caesium atoms available for trapping. To determine whether the coating was functional, a MOT was obtained from the <sup>133</sup>Cs<sup>+</sup> beam. The use of the offline

stable ion source and the beam line from the source until the beam switchyard was obtained for a short time to test this.

To rule out the presence of caesium atoms from the ampoule test, the experiment was run with the valve to the ampoule closed, and no MOT fluorescence was observed. The trace shown in Figure 3.17 was taken just before the ion beam tests. Once the gradient field was turned on at 20 s, there was no noticeable increase in the MOT fluorescence, confirming that there were no Cs atoms left over from the vapour tests.

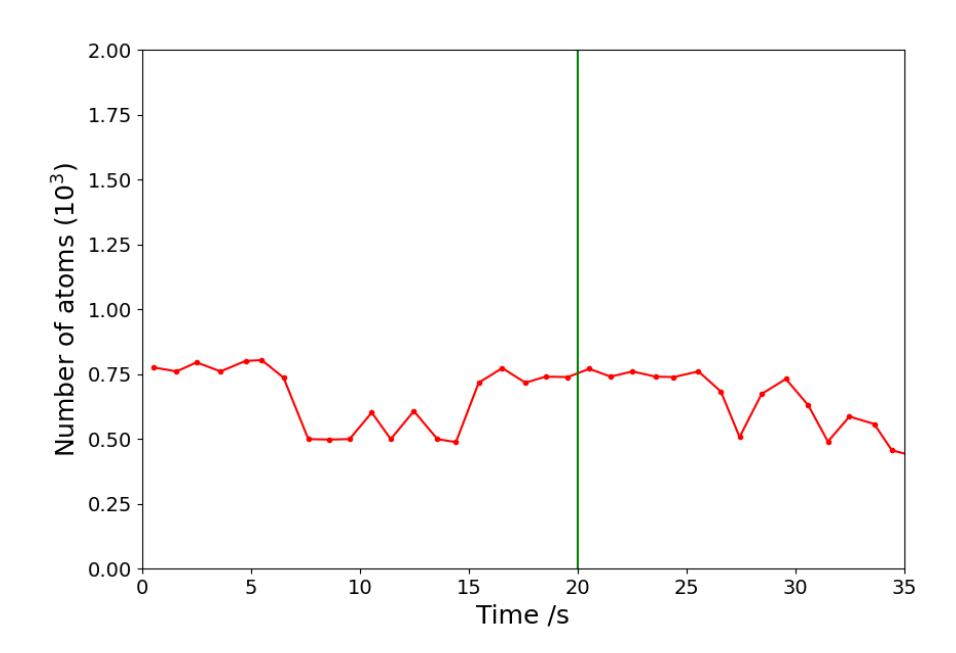


**Figure 3.17:** Confirmation of no visible MOT fluorescence prior to offline ion beam tests. The green line at 20 s indicates the gradient field being turned on,

The current of the beam was measured via the neutraliser, and it was  $(4.8 \pm 0.6)$  pA, which corresponds to  $(3.0 \pm 0.4) \times 10^7$  ions per second. The current was measured at the neutraliser, as this is the only way of measuring the ion beam within the cold atoms chamber. However, this method of measuring the ion beam current is less accurate than the Faraday cup, as the secondary current that can be generated by the impact of the ion beam onto the yttrium foil is not suppressed as it would be for a Faraday cup [63]. The measured current is in fact inflated by the secondary

current, meaning that the number of atoms from which

The MOT shown in Figure 3.18 was obtained at a neutraliser temperature of 984 K, and contains 250,000 atoms. A visible MOT was detected at neutraliser temperatures as low as 698 K. This MOT confirms that the coating is reducing the proportion of atoms that are being adsorbed to the surface of the chamber. Were this not the case, then it would not be possible to trap a MOT due to the limited number of atoms introduced via the beam. Though there was less concern about the status of the neutraliser, this test also verified that the neutraliser was working well after three years of not being used.

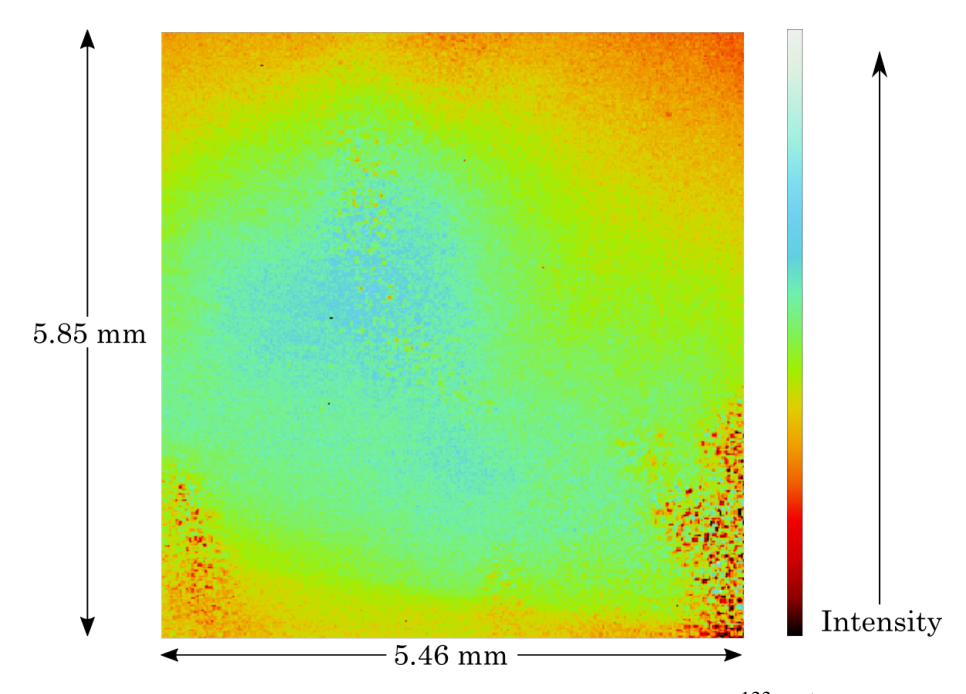


**Figure 3.18:** Colour-scaled image of MOT from offline <sup>133</sup>Cs<sup>+</sup> beam

In addition to this, whether the multi-step process of: the neutralisation of the ions, the emission of atoms from the neutraliser, the thermalisation of atoms and then the trapping of said atoms is happening quickly enough that an increase in the MOT population can be seen when the ion beam is allowed into the cold atoms chamber is strong evidence that the PDMS coating is functioning as needed. This growth of the MOT population can be seen in Figure 3.19, a time trace of the MOT fluorescence.

During this test, the neutraliser was heated to a lower temperature of 733 K. Higher temperatures produced a much larger MOT from the bulk of the neutraliser which was quickly depleted, meaning that the observation of the MOT growing as a direct result of the  $(4.8 \pm 0.6)$  pA ion beam wouldn't be possible. However, working with a smaller MOT also meant that fluctuations in the background fluorescence were noticeable. Under these circumstances, the absolute values of the number of atoms in the MOT as obtained from the fluorescence level are unreliable. However, the change in fluorescence that is detected when the MOT is released by turning of the gradient field does still correspond to the number of atoms that were in the MOT. So, the number of atoms in the MOT was found by turning the gradient field off and measuring the change in the calibrated number of atoms value. As such, Figure 3.19 instead has a relative vertical scale, and the number of trapped atoms inferred from each instance of turning off the gradient field is labelled on the trace.

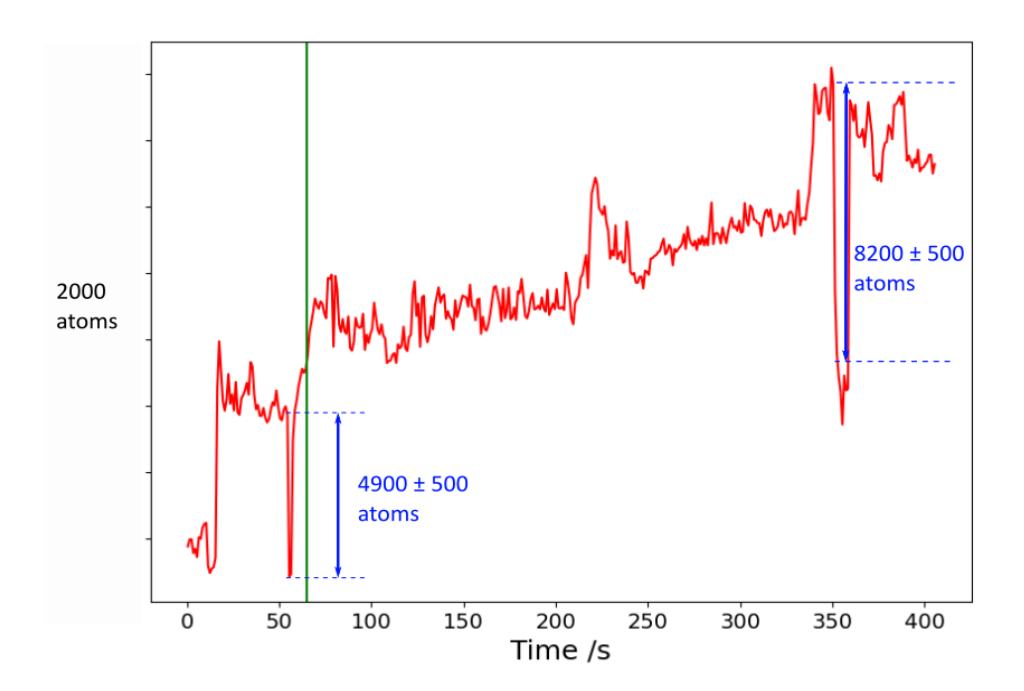


**Figure 3.19:** Fluorescence of MOT captured from offline <sup>133</sup>Cs<sup>+</sup> beam. Green line indicates when the gate valve between the beam and cold atoms chamber was opened.

The size of the MOT was verified at two different points in the trace by turning

the magnetic field off and noting the decrease in fluorescence measured. The gradient field for the MOT was turned on at 15 s, then the magnetic field was turned on and off again at 55 s, just before the valve was opened, and the MOT population was verified as 4900. The valve was opened at 65 s (indicated by the green line in Figure 3.19). The MOT was allowed to grow with the ion beam entering the chamber until 355 s. In the space of 290 s, the MOT population grew from (4900  $\pm$ 500) to (8200  $\pm$ 500) atoms. This uncertainty has been obtained from the variation in population before the ion beam entered the chamber. This growth in the MOT population indicates that the coating was in a good enough condition for the ions to be converted to atoms and then trapped in the MOT within minutes.

However, in addition to the rising background mentioned above, there are also large fluctuations in the atom number during the time that the ion beam was allowed into the chamber. If we consider the ion beam current as detected at the neutraliser over a similar period of time, in Fig. 3.20, it is apparent that it also experiences large fluctuations.

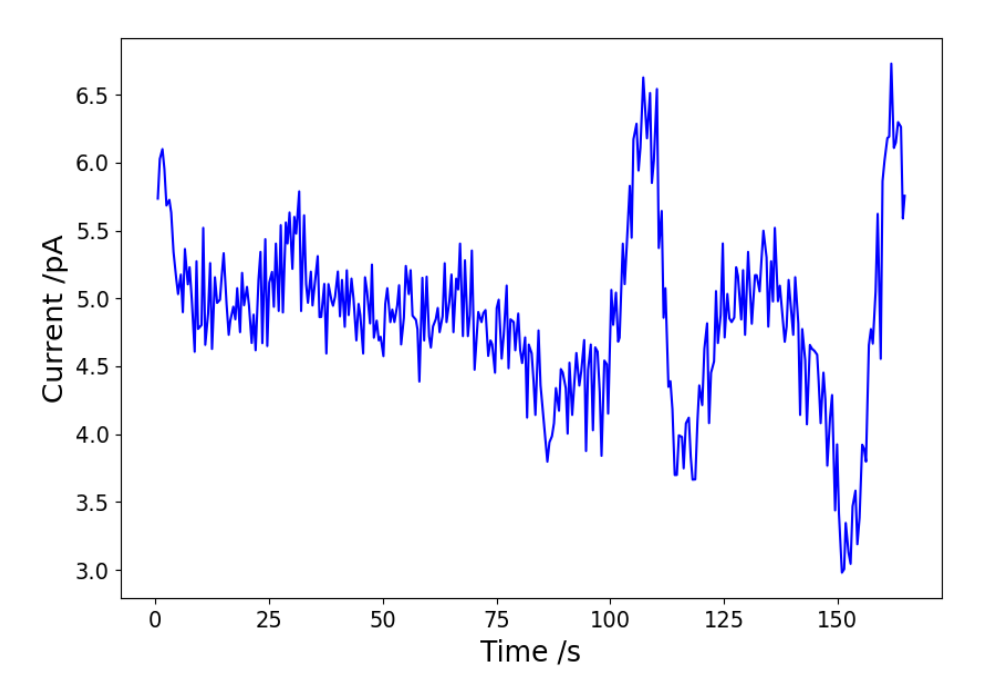


Figure 3.20: Ion beam current as detected at the neutraliser.

When the ion beam has fluctuations, those fluctuations in atom/ion number are passed through the trapping process; through diffusion, thermalisation and trapping, thereby causing an increased or decreased number of atoms trapped in the MOT. The fluctuations present in Fig. 3.19 are large, comparable to 50% of the starting MOT population. And in Fig. 3.20 the fluctuations are of a similar scale. Furthermore, the fluctuations occur on a similar time scale, at 217 s in Fig. 3.19 and 100 s in Fig. 3.20. While these fluctuations make the MOT fluorescence trace more difficult to interpret, they are in fact another indicator that the system is neutralising, thermalising, and trapping atoms directly.

# 3.5 Offline caesium-134 & $^{135}$ aesium-135 ion beams

This section discusses the sources for <sup>134</sup>Cs<sup>+</sup> and <sup>135</sup>Cs<sup>+</sup>, with details of their production, and the progress to date in obtaining offline beams from them.

#### 3.5.1 Irradiated caesium

As a result of a collaboration with Dr Ulli Koester at the Institut Laue-Langevin (ILL), we obtained sources of <sup>134</sup>Cs and <sup>135</sup>Cs. The ILL nuclear reactor produces a high flux of neutrons, and this was used to produce radioactive caesium atoms. The following process is carried out at ILL.

Diluted CsNO<sub>3</sub> solution is placed in quartz ampoules (outer diameter of 8 mm, inner diameter of 6 mm, length of 45 mm) and dried, such that each ampoule contains 5  $\mu$ g of Cs and 2.3  $\mu$ g of NO<sub>3</sub>. These are then placed into the path of the neutron flux, where single or double neutron capture reactions can occur. This leads to the production of <sup>134</sup>Cs and <sup>135</sup>Cs respectively.

The proportion of  $^{134}\text{Cs}$  to  $^{135}\text{Cs}$  that is produced via neutron capture reactions depends upon the length of time for which the caesium is irradiated, as the amount of  $^{135}\text{Cs}$  that is produced increases with the irradiation time. The first batch of ampoules were irradiated for 10 days, as the goal was to create  $^{134}\text{Cs}$  atoms. It was estimated that these ampoules had  $5\times10^{14}$   $^{134}\text{Cs}$  atoms,  $3.3\times10^{13}$   $^{135}\text{Cs}$  atoms and  $2.2\times10^{16}$   $^{133}\text{Cs}$  atoms that were not transmuted. The second batch of ampoules

were irradiated for 50 days to increase the amount of  $^{135}$ Cs atoms produced.  $2.0 \times 10^{16}$   $^{133}$ Cs atoms are estimated to have remained unchanged, and  $1.9 \times 10^{15}$   $^{134}$ Cs atoms and  $6.5 \times 10^{14}$   $^{135}$ Cs atoms will have been produced.

As a consequence of the ampoules being irradiated, trace impurities within the quartz are also activated such as <sup>46</sup>Sc, <sup>51</sup>Cr, <sup>65</sup>Zn, <sup>95</sup>Zr, <sup>124</sup>Sb. These pose no contamination risk, as the active atoms remain in the quartz, even when the ampoule is broken and crushed. The more serious risk of contamination comes from traces of active atoms on the surface of the ampoules as a result of being handled by equipment in the hot cell in which the irradiation takes place. This consists of <sup>51</sup>Cr, <sup>60</sup>Co and <sup>124</sup>Sb, and will be removed by washing the ampoules in acid before being handled by our colleagues in Jyväskylä.

## 3.5.2 Preparation of ion beam

The following work described was carried out by our colleagues from the University of Jyväskylä, as they have more experience working directly with radioactive materials.

The ampoules contain  $CsNO_3$  at a concentration of  $0.166 \,\mu g/ml$ . A  $50 \,\mu l$  water droplet (corresponding to  $2.56 \times 10^{13}$  atoms) is dried onto a piece of  $6.6 \,mg/cm^2$  Tantalum (Ta) foil. To produce  $Cs^+$  ions, the atoms need to be heated quickly and greatly, then the ions can be accelerated and guided towards the cold atoms chamber. Unlike the offline  $^{133}Cs^+$  beam, the ionisation of the caesium atoms in these samples takes place in a 'Hot Cavity', pictured in Figure 3.21.

It consists of a metal ionisation tube in which the sample is placed, a copper inductive heater coil, two water-cooled copper mounts that support the ionisation tube and serve as electrical contacts for the inductive heater that are attached to a base, and finally a suspension mount to the front of the tube through which a thermocouple can be attached to monitor the temperature of the cavity.

The heating comes from either resistive heating or radio frequency (RF) heating. The former is the more simple method of heating where an electric current is

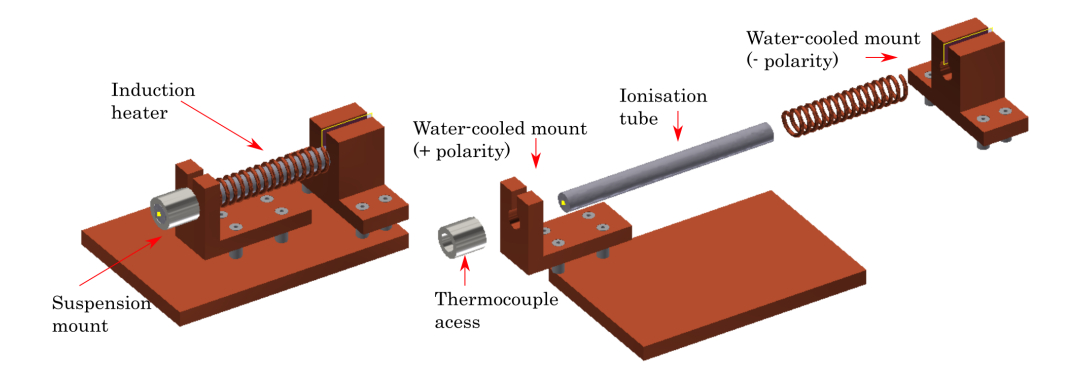


**Figure 3.21:** Diagram of 'Hot Cavity'. The actual cavity is the dark grey component within the copper coil. The Ta foil is inserted into the cavity from the left.

run through the copper coil to provide heating. The latter is the method used for higher temperatures and quicker rise times, where an AC current oscillating at radio frequencies is sent through the inductive heater to create a magnetic field that will induce eddy currents in the ionisation tube. These eddy currents heat up the ionisation tube and the sample inside it.

All throughout this process, several safety measures will have to be taken due to the risks that come with working with radioactive materials. Indeed, the liquid nature of the radioactive materials introduces additional hazards- the evaporation and spillage of radioactive material.

#### 3.5.3 Caesium-133 test beam

Along with samples of <sup>134</sup>Cs and <sup>135</sup>Cs, we were also sent samples of <sup>133</sup>Cs prepared in the same way as the radioactive specimens. These were used to test and optimise the production of the ion beam from the ampoules, as well as establish the above procedure for the preparation of samples, by our colleagues from the University of Jyväskylä.

To detect the ions in the beam, the current of the beam was measured at the switchyard (shown in Figure 3.1). Figure 3.22 shows the measured current over the 20 hours it took to deplete the sample in the Hot Cavity. Integrating the graph gives a total of  $4.5 \times 10^{12}$  ions detected at the switch yard. This means that we have an efficiency of 18% for the Hot Cavity beam.

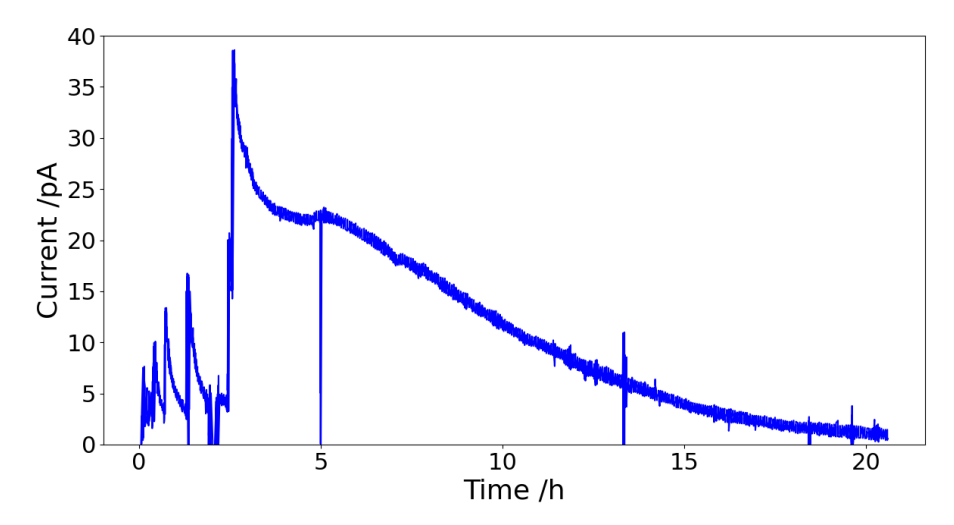


**Figure 3.22:** The current detected at the switch yard due to the ion beam. The first 2.5 hours on the graph correspond to an initial period of ion beam alignment and optimisation.

In addition to measuring the amount of ions in the beam, a mass scan of the beam was taken (Figure 3.23). As the switch yard guides beams towards the correct beam line experiments based on the mass to charge ratio of the beam, the solitary peak at a mass of 133 verifies that the beam consists of <sup>133</sup>Cs ions.

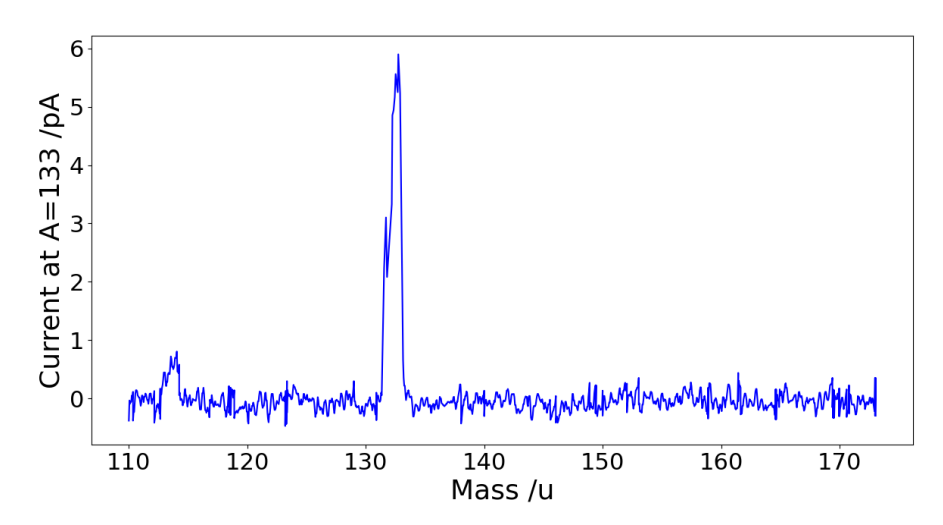


**Figure 3.23:** Mass spectrometry measurement of the ion beam. The single peak at a mass of 133 confirms that the beam consists of <sup>133</sup>Cs.

# Chapter 4

# **Offset Locking**

One of the significant changes required when working with different isotopes of caesium is that the frequency of the cooling and repump lasers will need to change, as the electronic structures of the isotopes are shifted relative to the <sup>133</sup>Cs isotope. The following chapter covers the work done to assess these changes and develop the apparatus to accommodate them. The frequency shifts that will need to be made to the <sup>133</sup>Cs isotope cooling and repump transitions have been calculated. Section 4.2 describes the set up of a frequency offset locking system which will enact the frequency shifts. Due to the COVID-19 pandemic's impact on international travel, this was set up and characterised in UCL, and will later be installed in Jyväskylä.

# 4.1 Variation in cooling cycle frequencies with isotopes and isomers

The shifted trapping and repump frequencies for <sup>135</sup>Cs, <sup>134</sup>Cs and the metastable <sup>135m</sup>Cs isomer are calculated below. Though the main objective of the experiment is to trap and cool the <sup>135m</sup>Cs isomer down to a BEC, the apparatus itself is designed to trap atoms from an ion beam. <sup>135</sup>Cs and <sup>134</sup>Cs are longer lived isotopes of caesium, and a <sup>134</sup>Cs MOT has not as yet been achieved, though a MOT of <sup>135</sup>Cs was obtained by Di Rosa et al. [64]. Furthermore, a potential source of the two isotopes has been found, as discussed in Section 3.5.

To find the shifted frequencies, first the change to the fine structure splitting

must be considered. Specifically, what the isotopic shift,  $\delta_{v}$ , in the difference between the  $6s^{2}S_{1/2}$  and the  $6p^{2}P_{3/2}$  levels is. The causes of this shift are mentioned in Section 1.3. This was found for the isotopes and isomer in [65].

The hyperfine structure is caused by the interaction of the nuclear magnetic dipole moment with the electrons' magnetic field, and the nuclear electric quadrupole moment with the electric gradient of the distribution of charge in the atom [21]. As these moments vary between isotopes and isomers, so does the hyperfine structure. For each of the species, the hyperfine energy shifts were calculated using the below formula (previously mentioned in Section 1.3) [20],

$$\delta = \frac{1}{2}AK + B\frac{\frac{3}{2}K(K+1) - 2I(I+1)J(J+1)}{2I(2I-1)2J(2J-1)}$$
(4.1)

where A and B are the hyperfine constants for the magnetic dipole and electric quadrupole moments, I is the nuclear spin, J is the total electron angular momentum. K is defined in Eq. 1.4. The parameters that differ from isotope to isotope are shown in Table 4.1.

|                    | Ι             | $\delta_{\scriptscriptstyle V}$ /MHz | $A(6S_{1/2})$ /MHz | $A(6P_{3/2})$ /MHz | $B(6P_{3/2})$ /MHz |
|--------------------|---------------|--------------------------------------|--------------------|--------------------|--------------------|
| <sup>134</sup> Cs  | 4             | 33.1                                 | 2328.2             | 51.3               | 54.9               |
| <sup>135</sup> Cs  | $\frac{7}{2}$ | -36.4                                | 2430.9             | 53.5               | 3.7                |
| <sup>135m</sup> Cs | <u>19</u>     | -17.6                                | 713.6              | 15.7               | 126.6              |

**Table 4.1:** From left to right, the parameters for each species shown are: nuclear spin I, isotopic shift  $\delta_{\nu}$ , the magnetic dipole hyperfine constants for  $6S_{1/2}$  and  $6P_{3/2}$ , and the electric quadrupole hyperfine constant for  $6P_{3/2}$ .

As  $^{135}$ Cs has the same nuclear spin as the  $^{133}$ Cs isotope, the F values for the hyperfine levels were no different as given by

$$F = |I - J|, \dots, |I + J| \tag{4.2}$$

in steps of one, meaning that the cooling and repump transitions are still  $F=4 \to F'=5$  and  $F=3 \to F'=4$ . However, for  $^{135m}\text{Cs}$  and  $^{134}\text{Cs}$ , I differs which leads to different F values. For  $^{134}\text{Cs}$ , the cooling transition is  $F=\frac{9}{2} \to F'=\frac{11}{2}$ , and the repump is  $F=\frac{7}{2} \to F'=\frac{9}{2}$ . For  $^{135m}\text{Cs}$  the cooling transition is  $F=10 \to F'=11$ , and the repump is  $F=9 \to F'=10$ .

The transition frequencies are given by [20]:

$$\Delta v = v_c - \delta_F + \delta_{F'} \tag{4.3}$$

where F and F' are the lower and upper energy levels respectively, and  $v_c$  is the energy difference between  $6^2S_{1/2}$  and the  $6^2P_{3/2}$ . The numbers calculated are shown in Table 4.2

| Transition                 | Frequency/ MHz  | Shift from <sup>133</sup> Cs/ MHz |  |
|----------------------------|-----------------|-----------------------------------|--|
| <sup>135</sup> Cs Cooling  | 351 721 709.825 | -250.705                          |  |
| <sup>135</sup> Cs Repump   | 351 731 163.282 | 261.102                           |  |
| <sup>134</sup> Cs Cooling  | 351 721 960.530 | -543.805                          |  |
| <sup>134</sup> Cs Repump   | 351 731 573.731 | 671.551                           |  |
| <sup>135m</sup> Cs Cooling | 351 722 566.675 | 606.145                           |  |
| <sup>135m</sup> Cs Repump  | 351 729 456.680 | -1 445.500                        |  |

**Table 4.2:** Summary of cooling and repump transition frequency shifts for  $^{135}$ Cs,  $^{134}$ Cs, and  $^{135m}$ Cs.

# 4.2 Frequency offset locking

## **4.2.1** Offset Phase Lock Servo (OPLS)

Ideally, when trapping any isotope of caeisum, the lasers would be locked to the atomic transitions of the species being trapped. However, the manufacture of ra-

dioisotope vapour cells comes with many difficulties. The cells are typically filled with the alkali vapour by one of three main methods: evaporating pure liquid alkali metal, inducing a chemical reaction in an alkali compound, and dispensing the vapour from a solid state dispenser [66]. Manipulating the active isotopes into states from which the cell could be filled poses safety risks to those involved. In any case, alternative methods of frequency locking would be needed for shorter lived species, regardless of the feasibility of vapour cell production.

The locking scheme described in this chapter is known as frequency offset locking. A master, or reference laser, is locked to a known atomic transition or Fabry-Pérot resonator. For this experiment, the master lasers will be locked to  $^{133}$ Cs transitions. The second laser, the slave laser, is locked a set frequency away from the master, matching the desired frequency. The frequency offset between the two lasers is monitored using a beat note. In general terms, this is a signal that is produced when two waves of slightly different frequencies ( $f_1$  and  $f_2$ ) are summed, where the resulting signal has a periodic variation in amplitude. The variation in the amplitude occurs at the frequency difference between the two superposed waves,  $|f_1 - f_2|$  known as the beat frequency [67]. In this case, the signal is produced by overlapping the two laser beams, and the beat frequency is detected in the intensity of the beam using a photo diode.

The frequency offset locking scheme set up in London was the Vescent D2-135 Offset Phase Lock Servo (OPLS). It is capable of phase locking or frequency offset locking, in the event that phase locking is not possible. Figure 4.1 shows a schematic of the internal circuit of the OPLS. Beams from both the master and

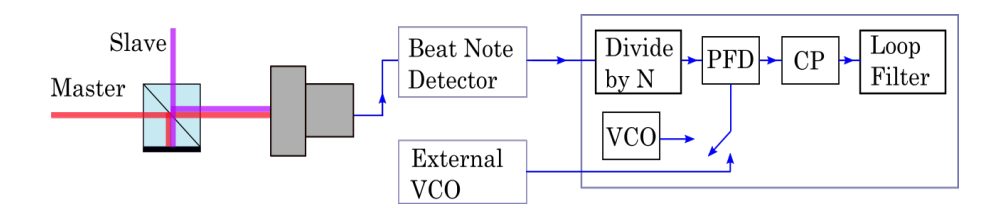


**Figure 4.1:** Schematic of the OPLS internal circuit, illustrating how the beat note is converted to an error signal. PFD: Phase Frequency Detector, CP: Charge Pump, VCO: Voltage controlled Oscillator.

slave laser are overlapped to and injected into a fibre, which is connected to a beat note detector. The OPLS is capable of locking to wide range of offset frequencies, from 250 MHz to 10 GHz. The upper limit of this range is dictated by the highest frequency the fast photo-detector in the beat-note detector can detect. In order to facilitate this large range of frequencies, the beat frequency is divided by a power of two, either N = 8, 16, 32, 64, and then compared to the reference signal. The N value is chosen via a front panel setting. The internal Voltage Controlled Oscillator (VCO) can be set to produce reference signals for offset frequencies which, once multiplied by the N value, range from 385 MHz to 10 GHz. Reference signals for frequency offsets as low as 250 MHz can be used with the use of an external signal generator.

The divided beat frequency and the reference signal are then input into the Phase Frequency Detector (PFD), where their frequencies and phases are compared. The PFD outputs a signal proportional to the phase difference between the lasers, which is then used to create the error signal for phase locking. In the event that phase locking is not possible, the PFD compares the beat and reference frequencies and outputs a signal proportional to the difference between them. The PFD output passes through a charge pump, a circuit in which capacitors are used to produce higher voltages [68], and a loop filter which provides the feedback going to the slave laser to maintain the frequency of the beat note. The error signal shown in Figure 4.2 is symmetrical, and the reflection point (shown in blue) is where the master laser is locked.

The loop filter has PID feedback for the locking. The output, u(t) of a PID feedback loop is given by Eq. 4.4 [69]

$$u(t) = K_P e(t) + K_I \int_0^t e(t) + K_D \frac{de(t)}{dt}$$
 (4.4)

where the error, e(t), is the discrepancy between the value to be maintained and the measured value in the feedback loop. The constants  $K_P$ ,  $K_I$  and  $K_D$  determine the size of the contribution that each response has to the overall output, and in electrical

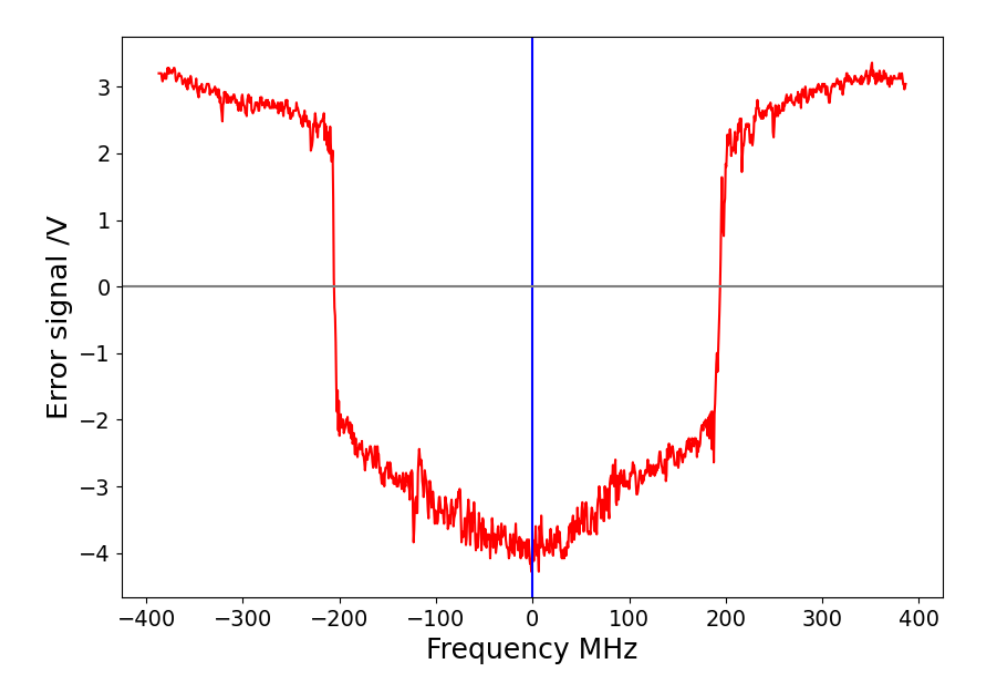


**Figure 4.2:** Error signal produced by the OPLS, the blue line shows the reflection point of the signal, which is where the master laser has been locked

terms, they are the gain for each part of the circuit. The proportional response is determined by the error at any one time. The integral response is determined by the sum of the error over a given time. And the differential response is linked to the rate of change of the error. The  $K_P$  and  $K_D$  gains can be tuned in the OPLS, as well as the corners of the PID loop's transfer function, shown in Figure 4.3 [70].

A transfer function defines the output of a system for every possible input [71]. Figure 4.3 shows the gain of the feedback response for a perturbation of a given frequency. There are three corners in the function, the first is  $f_I$ , the frequency where the feedback loop switches from an integral response to proportional response. The second,  $f_D$ , is the frequency at which the feedback loop response switches from a proportional response to a differential response. The third,  $H_F$  is a high frequency cut-off. The differential response will only increase for higher and higher frequencies, a cut-off point is needed to prevent the differential response from amplifying high frequency noise in the circuit.

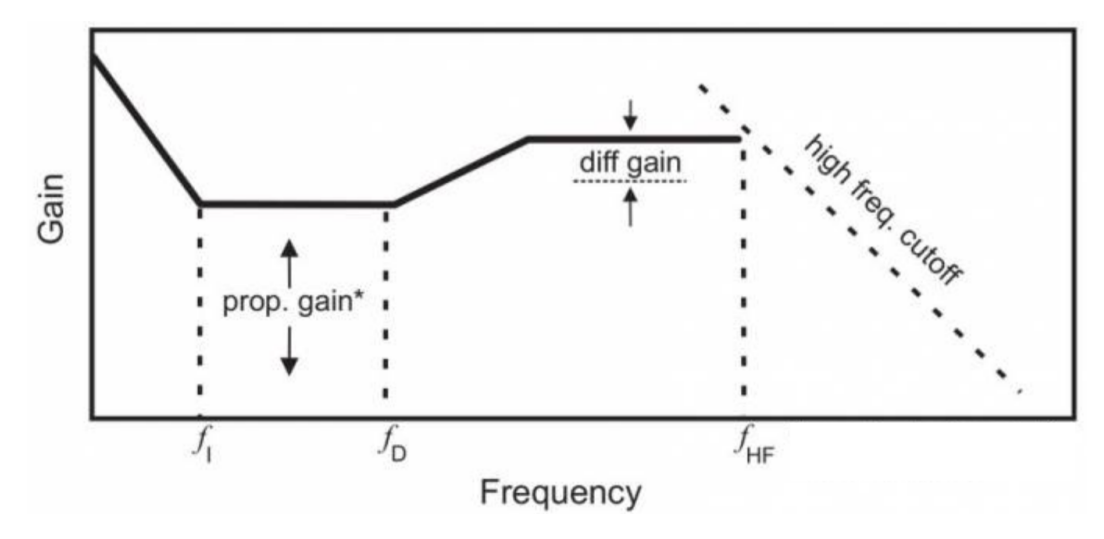


**Figure 4.3:** Transfer function of the OPLS, shown with three corners in the function-  $f_I$ ,  $f_D$  and  $f_{HF}$ 

## 4.2.2 Optical alignment

The lasers used for the characterisation of the OPLS in this chapter lacked the capability to be locked with feedback going to the current of the laser diode, which is required for phase locking. Hence only frequency offset locking has been demonstrated. The laser apparatus that was used for this is shown in Figure 4.4.

The master ECDL laser alignment includes a DAVLL arrangement, explained in Sections 2.2.1 and 2.2.3. While it was not strictly necessary for frequency offset locking, the slave ECDL laser's alignment also includes a SAS arrangement (also explained in Sections 2.2.1 and 2.2.3), so that the frequency of the slave laser could be monitored in relation the master laser lock position.

The beat note detector requires an input power in the range of 50  $\mu$ W to 1 mW. Beams of 350  $\mu$ W were taken from both laser and are combined at an NPBS, as a beat note would not have been produced had the two beams been of orthogonal polarisations. The beams were coupled into the fibre after passing through a telescope to reduce the size of the beams and an additional lens that aided the injection of the fibre.

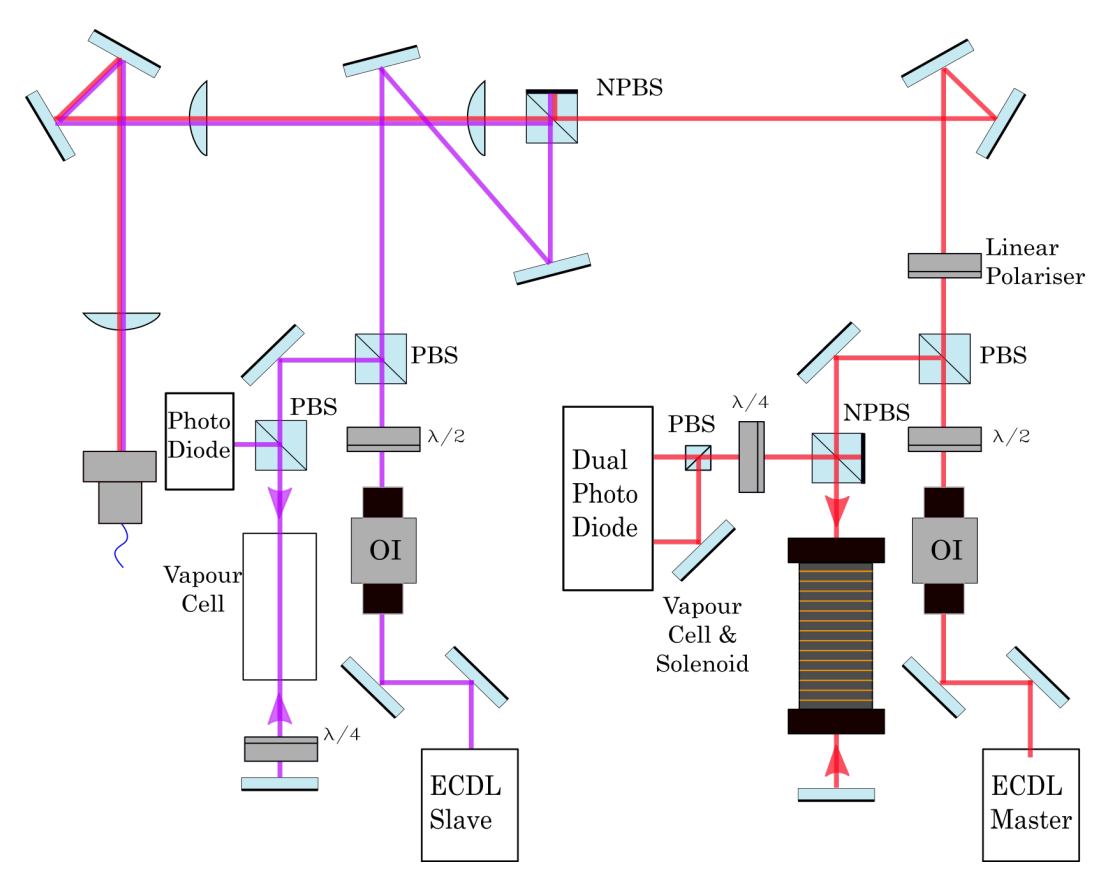


**Figure 4.4:** Optical alignment used with the Vescent OPLS. The master laser is shown in red, the slave laser in purple.

## 4.2.3 Beat note and locking

Initially, both the master and slave lasers were tuned to the cooling manifold. The spectroscopy of the slave laser and the error signal could be seen together (as shown in Figure 4.5). Hence, the beat frequency, the reference signal and the position of the error signal could be compared and confirmed to correspond to one another, before moving on to larger frequency offsets. The spectroscopy of the slave laser also allowed the monitoring of the condition of the laser. The beat frequency was observed on an Anritsu MS2718B spectrum analyser.

Once the beat note was found and only a very basic frequency lock was obtained, the parameters for the PID loop were optimised. These are the values of the proportional and differential gain ( $K_P$  and  $K_D$ ), and the corners of the PID function ( $f_I$ ,  $f_D$  and  $f_{HF}$ ). A comparison is made in Figure 4.6 between the beat frequency when it was unlocked and locked with optimised parameters. The locked beat note

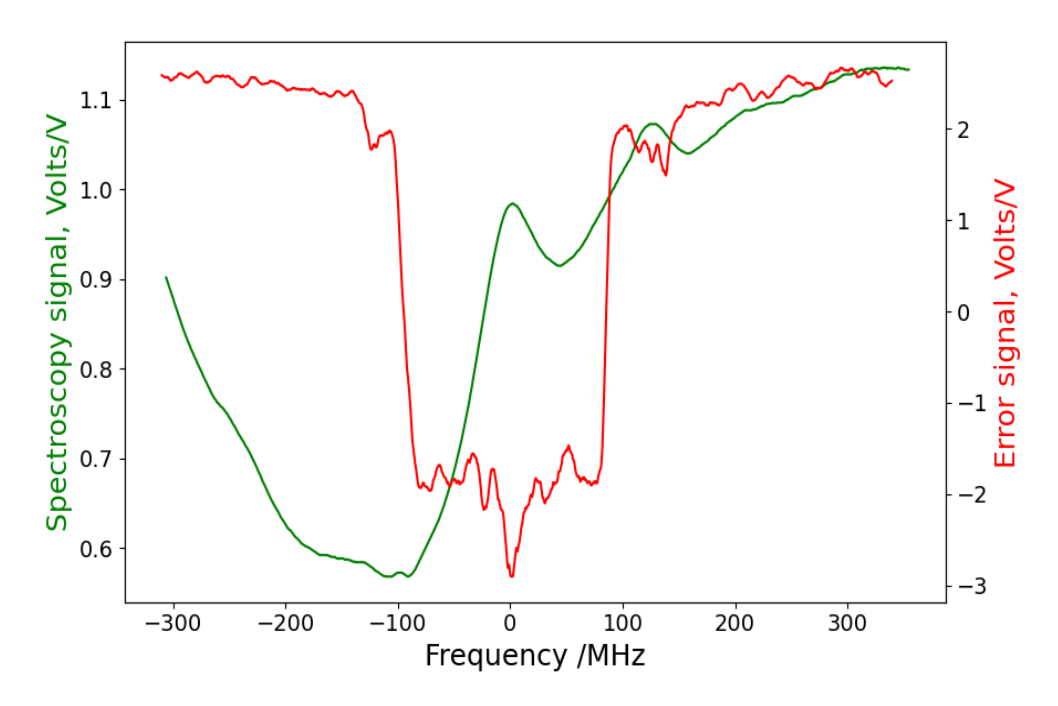


**Figure 4.5:** Error signal (red) shown with spectroscopy of slave laser (green). The x-axis is frequency from master locking point

appears to have a larger spread of frequencies in it than the unlocked beat note. However, the amplitudes of the other frequencies in the beat note are comparatively low, meaning that the wider spread of frequencies that comes with locking the slave laser should not make a significant difference to the experiment. In addition to this, the purpose of offset locking has been achieved, in that the main frequency of the locked beat note is maintained for up to an hour after initial locking.

Frequency offsets up to 9.9 GHz were successfully locked to, with more focus given to the 120 MHz - 2 GHz range as that is where the repump and cooling frequency offsets fall for the isotopes and isomers considered. This range is shown in Figure 4.7. The lowest frequency offset that can be achieved with the OPLS is quoted as 250 MHz. However in practice, it was found to be 200 MHz, which provides a good overlap between the frequency alteration that can be provided by an AOM with a single laser system. Now, with the offset locking system characterised and established, it will be installed in Jyväskylä. This will replace the current system of having multiple double pass AOMs instead of one double pass AOM before

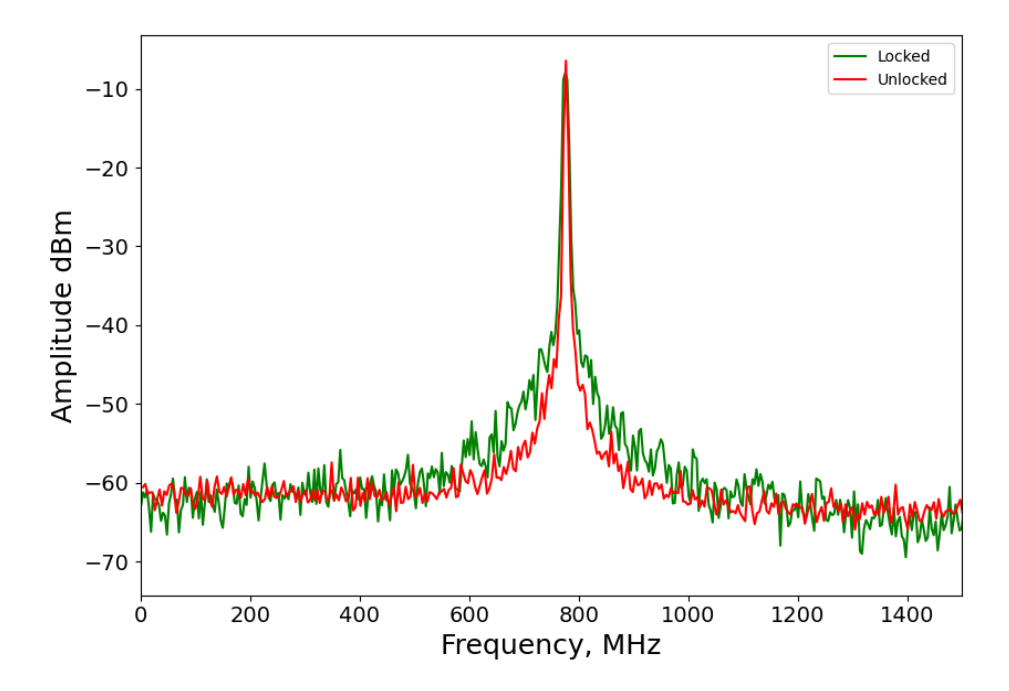


**Figure 4.6:** Locked and unlocked beat frequencies as seen on the spectrum analyser, with optimised locking parameters.

spectroscopy.

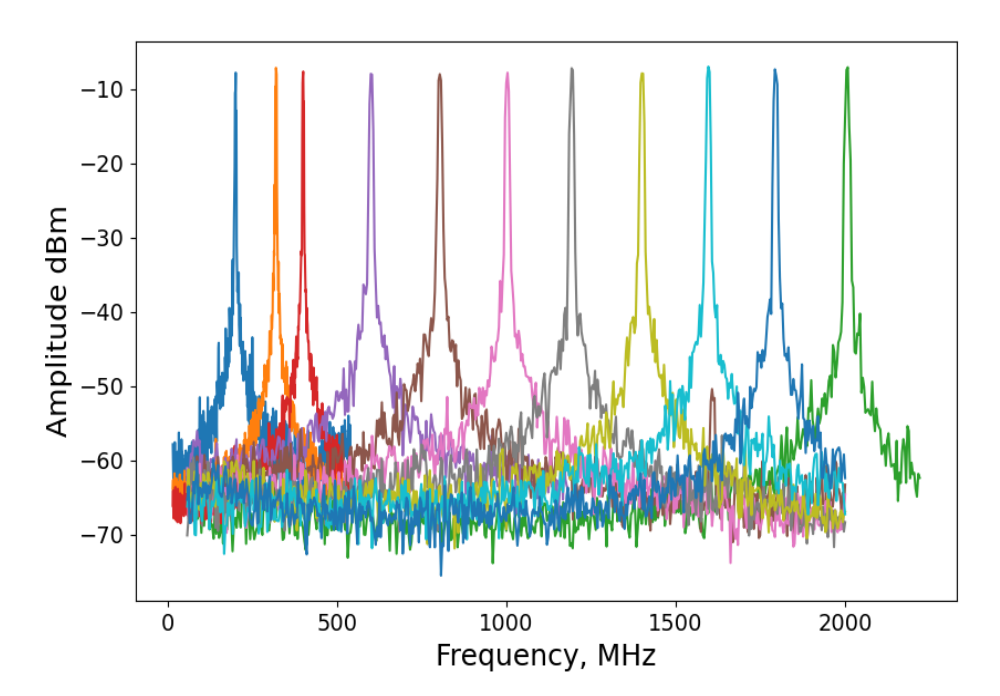


**Figure 4.7:** Demonstration of the range of frequency offsets that can be locked in the 120 MHz to 2 GHz range. The plot shows the beat frequencies as seen on the spectral analyser.

# **Chapter 5**

# **Cold Atom Magnetometry**

In addition to working on the caesium experiment in London, I also worked on a cold atoms rubidium experiment, where the cold atoms have been used for optical atomic magnetometry. The preparation of the cold atoms for the magnetometry has a large overlap with the isomer trapping experiment in Chapters 2 and 3, and working on this in the intial stages of my PhD was beneficial.

The magnetometer presented in the following chapter is a Radio-Frequency Optical Atomic Magnetometer (RF-OAM). Using atomic spin and a coherent source of light to detect magnetic fields was proposed by Dehmelt [72], and first achieved by Bell et al. [73]. Much of RF-OAM research uses atoms at room temperature or above, known as thermal RF-OAMs [74, 75, 76]. However using cold atoms for atomic magnetometry is an attractive prospect. Current radio-frequency atomic thermal magnetometry experiments are limited in spatial resolution by the size of the vapour cells used. However this is an issue that does not affect cold atom magnetometry, where there is more control over the atomic motion, atomic samples of smaller volume, and also fewer collisions [77, 1].

This work was completed with Yuval Cohen, Dr Luca Marmugi, Michela Venturelli, Sindi Sula, and with assistance from Cameron Deans. It was published in *Applied Physics Letters* with the title *A cold atom radio-frequency magnetometer* [1]. The magnetometry specific additions to the experiment, data collection, and data analysis were carried out for the most part by myself and Yuval Cohen.

# **5.1** Working principles

RF atomic magnetometry relies upon an effect known as Larmor spin precession [78], where the electronic spin with Zeeman split energy states will precess about an external magnetic field. The frequency of this precession is known as the Larmor frequency. Its value is dependent on the magnetic field causing the Zeeman splitting between the magnetic sub levels. The precession involves the atom moving between the  $m_F$  states, once the degeneracy has been lifted by Zeeman splitting.

This precession alters the optical absorptive properties of the atoms. Specifically, the  $\sigma^+$  and  $\sigma^-$  polarised components of light experience different phase shifts,  $\phi_+$  and  $\phi_-$  respectively. They are given by [79]

$$\phi_{\pm} = \frac{2\pi l}{\lambda} n_{\pm} \tag{5.1}$$

where l is the length of the atom sample along the probe beam,  $\lambda$  is the wavelength of the probe beam and  $n_{\pm}$  is the refractive index for  $\sigma^{\pm}$  polarised light. For the overall beam, this causes the rotation of a linear polarisation, which occurs at the Larmor frequency and thus the frequency can be observed. This rotation is known as Faraday rotation. From this, the magnetic field splitting the levels can be found. This is how DC fields can be detected. AC magnetic fields can be detected by using a known DC magnetic field for Zeeman splitting, then exposing the optically pumped atoms to this field to drive the precession.

However, if all of the spins are out of phase with each other, all the polarisation shifts will cancel out, and no Larmor precession will be detected in the probe beam. To avoid this, all the atoms are optically pumped ([80, 81]) into a specific  $m_F$  state before their precession is driven, in order to have a coherent Larmor precession signal.

Consider the simplified case of a two state atom with  $m_F = 0, \pm 1$  for the ground state and  $m_F' = 0, \pm 1, \pm 2$  for the excited state, being pumped by  $\sigma^+$  light as pictured in Figure 5.1.  $\sigma^+$  will pump the atom into the excited state and increase  $m_F$  by

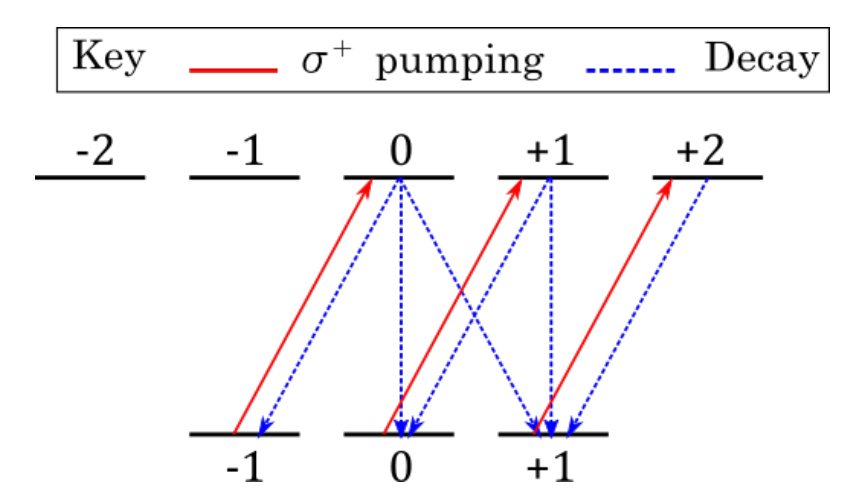


**Figure 5.1:** Optical pumping with  $\sigma^+$  light being used to polarise atoms with two states and three Zeeman split levels.

1, as shown in Figure 5.1. The atom will then decay to a ground state Zeeman sub-level with probabilities given by branching ratios, via transitions allowed by selection rules  $\Delta m_F = 0, \pm 1$ , also shown in Figure 5.1. In this way the atoms can be continually pumped until they all decay down to the  $m_F = +1$  state. This is possible, as an atom in this state will be excited to the  $m_F' = +2$  state, which can only decay back down to the  $m_F = +1$  state. This is also possible with  $\sigma^-$  light, in which case the atoms would be pumped into the  $m_F = -1$  state.

# 5.2 Apparatus and procedure

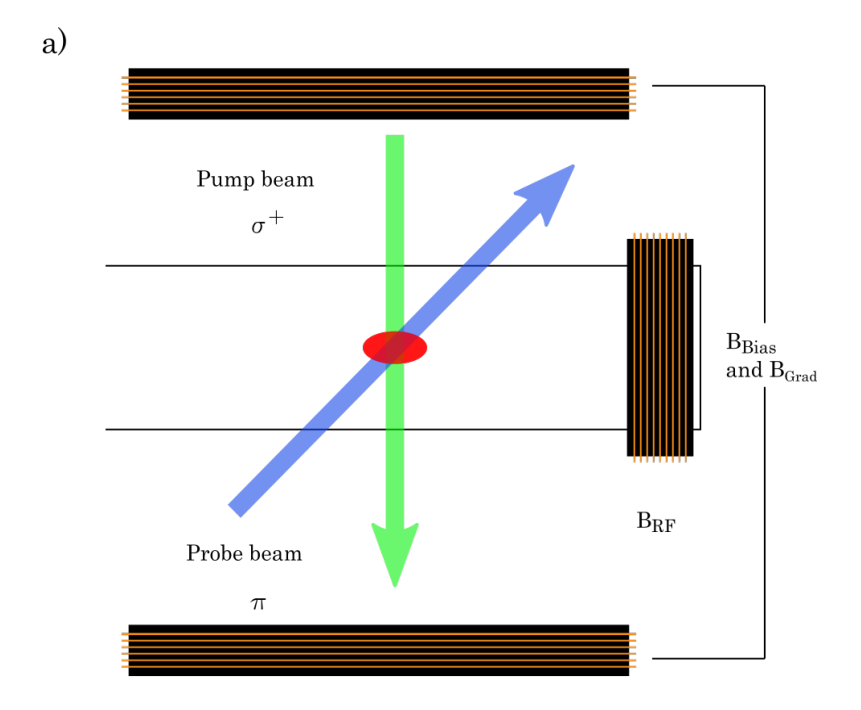
The science chamber used for the cold atom magnetometry is identical to the one used for the caesium double MOT system in Chapter 2, and a loading MOT is also used here. The six counter propagating beams for cooling and repump lasers are incident on the glass cell. The cooling laser is a 780 nm MOGLabs MSA003, a semi-conductor laser amplifier with an in-built seed laser.

It is tuned -1 $\Gamma$  to the red of the <sup>87</sup>Rb 5 $s^2S_{1/2}$ ,  $F=2 \to 5p^2P_{3/2}$ , F'=3 transition with  $\Gamma=2\pi$  x 6.066 MHz being the natural linewidth. The average intensity of the beams is 7.5 mW cm<sup>-2</sup>. The repump laser is a MOGLabs CEL002 tuned to the <sup>87</sup>Rb 5 $s^2S_{1/2}$ ,  $F=1 \to 5p^2P_{3/2}$ , F=2 transition and has an average intensity of 1.4 mW cm<sup>-2</sup>. There are coils in the anti-Helmholtz configuration that create a magnetic field gradient of 32 G/cm.

In addition to standard cold atoms equipment, there are magnetometry specific elements, as shown in Figure 5.2. There is an additional pair of coils for the homogeneous bias field that creates Zeeman splitting in the atoms for the optical pumping stage, known as  $B_{bias}$ . There is a single coil attached to the glass cell, and this produces an AC magnetic field that will drive the Larmor spin precession, known as  $B_{RF}$ . The RF coil is driven by the internal oscillator of the lock-in amplifier (AMETEK 7230 DSP). This effectively replicates fields that would be measured using the magnetometer. There is also the probe beam, a separate RadiantDyes NarrowDiode laser that has been tuned to the  $^{85}$ Rb  $5s^2S_{1/2}$ ,  $F = 3 \rightarrow 5p^2P_{3/2}$ , F = 3/4 crossover with an intensity of 257  $\mu$ W cm<sup>-2</sup>. The probe beam emerges from the science chamber and is then incident upon a PBS. This separates the different linearly polarised components, which are subsequently fed into a dual photodiode, where the difference between its two channels is given as an output, which will show the Faraday rotation at the Larmor frequency.

The sequence for the magnetometry procedure consists of preparing the cold atoms and then carrying out the magnetometry. The first stage of the procedure was to obtain a MOT. The MOT is loaded for 7 s before the next stage. The MOT is then compressed for 12 ms by rapidly increasing the magnetic field gradient to 59 G/cm. The cooling laser is detuned to -2 $\Gamma$ . Next, the atoms are cooled for 7ms using Polarisation Gradient Cooling (PGC). For this stage the magnetic field gradient is turned off. The cooling laser is now detuned to -4 $\Gamma$  and the intensity is reduced to 3 mW cm<sup>-2</sup>. This brings as many as  $10^8$  atoms down to a temperature of  $(19 \pm 4)\mu$  K at a density of  $10^{10}$  cm<sup>-3</sup>. This concludes the 'cold atoms' part of the procedure.

The next step is to prepare the atoms' spin polarisation, with the atoms in a single state, F = 2,  $m_F = +2$ .  $B_{bias}$  is turned on. The cooling laser is blocked, while the repump is tuned to the  $^{87}$ Rb  $5^2S_{1/2}$ ,  $F = 2 \rightarrow 5^2P_{3/2}$ , F' = 3 transition and is  $\sigma^+$  polarised. Finally,  $B_{RF}$  is turned on for 10 ms to drive the atoms' precession. Simultaneously, the probe beam is triggered so that the Larmor precession is observed.



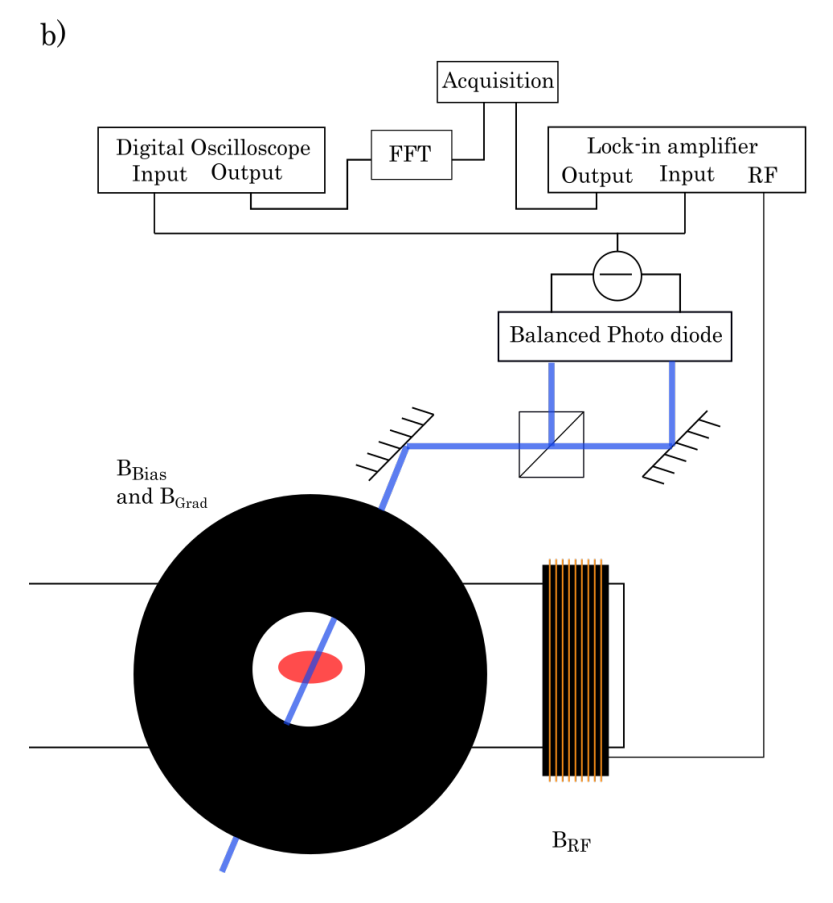


**Figure 5.2:** a) shows the glass cell containing the cold atom cloud with the coils that produce  $B_{Bias}$  and  $B_{RF}$ , and the optical pumping and probe beams. b) shows the top view of the apparatus and the probe beam's path after interacting with the atoms, with a schematic of the data acquisition system. The bias coils are placed on top of the coils that create the gradient field for the MOT,  $B_{Grad}$ .

The signal from the polarimeter is acquired for the whole of the RF pulse phase. It is then fed to the lock-in amplifier (AMETEK 7230 DSP) and a digital oscilloscope (Tektronix DPO2014). The lock-in amplifier, together with a LabVIEW data acquisition system, was used to quickly build up RF spectra for the optimisation of the magnetometer. For data taking, the input was sent to the oscilloscope which was triggered to collect the polarimeter signal during the 10 ms. A typical polarimeter signal is a sine wave oscillating at the Larmor frequency with an exponential decay component. This is then passed on to a LabVIEW program for analysis.

# 5.3 Results and analysis

## **5.3.1** Response of magnetometer

The decay constant of the exponential component of the magnetometer's output signal is found to be  $\tau = (8.4 \pm 0.3)$  ms. The amplitude of the Larmor oscillations reduces as the number of atoms undergoing coherent Larmor precession decreases. One mechanism through which atoms could no longer contribute to the signal is if they escape the atom cloud. Yet this is unlikely to contribute to the decay of the signal, as the MOT lifetime is on the order of  $10^2$  ms. The sources of noise that could quicken the decay of the signal are alkali-alkali collisions and random magnetic fields in the environment. Thus, the decay of the signal can be ascribed to the finite nature of coherent precession.

The magnetometer's sensitivity can be calculated as [82]

$$\delta B = \frac{B_{RF}}{SNR} \tag{5.2}$$

where  $\delta B$  is the sensitivity,  $B_{RF}$  is the field produced by the RF coil that drives the precession of the atoms and SNR is the Signal to Noise Ratio. The SNR is the ratio between the Fast Fourier Transform (FFT) of the polarimeter signal, and the noise signal. The noise signal is obtained by running the measurement without triggering  $B_{RF}$  and is shown in Figure 5.3 along with the signal. Equation 5.2 gives a sensitivity of 330 pT/ $\sqrt{Hz}$ . This is consistent with an alternative definition of sensitivity in Equation 5.3 [83],

$$\delta B_2 = \frac{\hbar}{g_F \mu_B} \frac{\Gamma}{SNR} \tag{5.3}$$

where  $\Gamma$  is the linewidth of the RF resonance,  $g_F$  is the Landé factor.

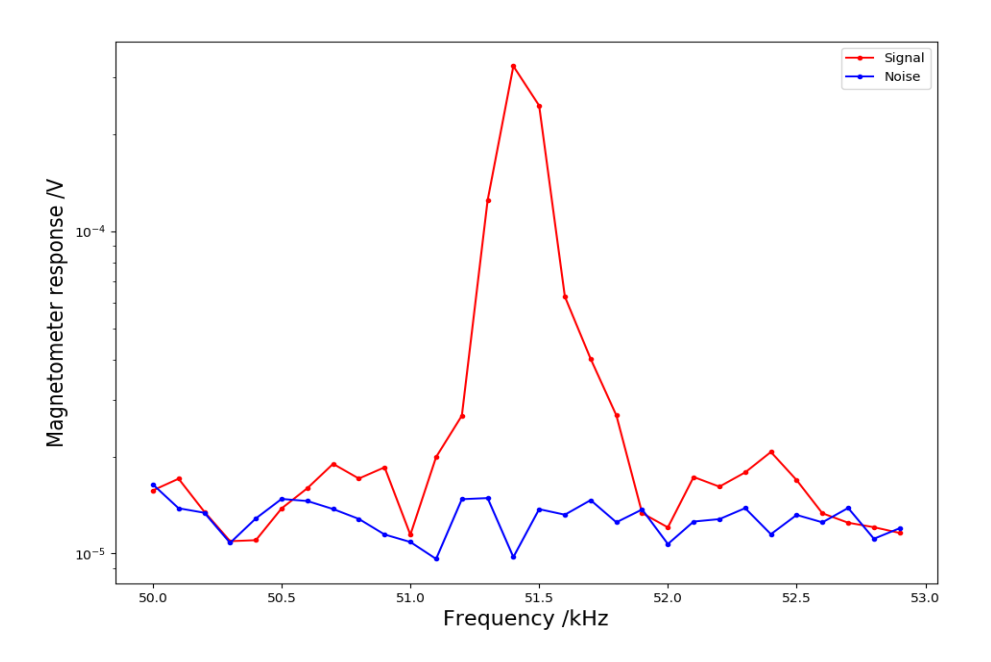
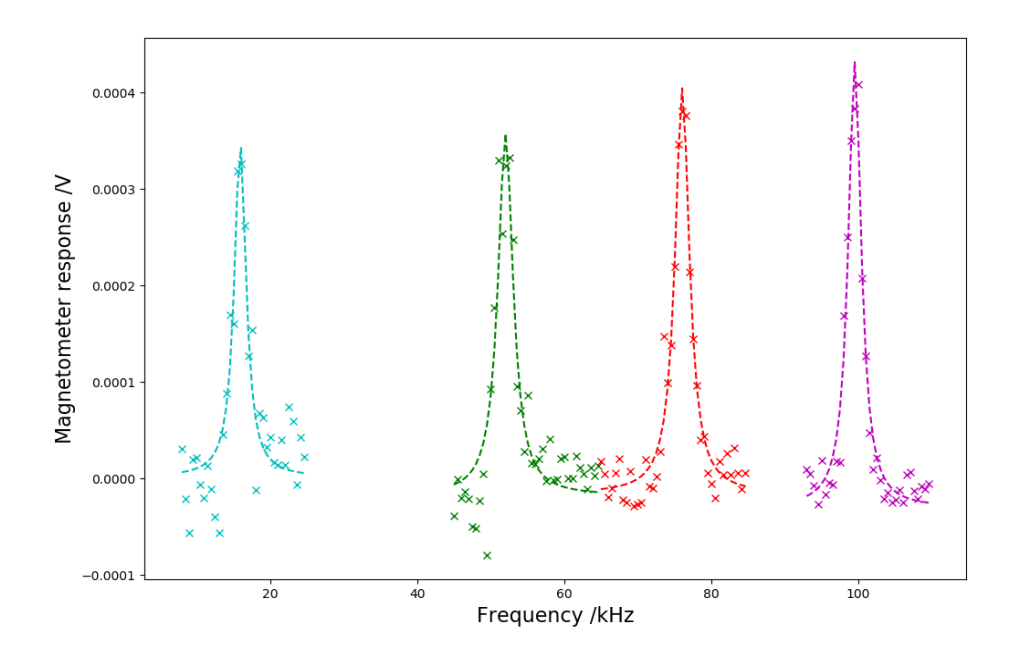


Figure 5.3: FFT of polarimeter signal for Larmor oscillation, and a noise FFT.

# 5.3.2 Operational range

The cold atom magnetometer is capable of measuring AC magnetic fields over a broad range of frequencies. Figure 5.4 shows displays operation from 16 kHz to 100 kHZ. There are small changes in the signal height, and negligible changes to the linewidth across the frequencies, however the sensitivity is consistently below  $nT/\sqrt{Hz}$  across the explored frequency range.

Due to the large tunable range of the magnetometer, it can be used to measure DC magnetic fields, as mentioned in 5.1, as different resonant frequencies would be detected for different DC fields. The operational frequency range shown by Figure



**Figure 5.4:** Lorentzian fits of data acquired using the lock-in amplifier, with resonant frequencies of 17 kHz, 52 kHz, 75 kHz, and 99 kHz.

5.4 corresponds to DC fields between 22.7 mG and 142.3 mG. The large operational range is also significant for AC magnetometry in the context of electromagnetic induction imaging (EII) [84]. EII uses an oscillating magnetic field to induce eddy currents in conductive materials, which cause secondary fields. These secondary fields are measured using an atomic magnetometer, and vary depending on the conductivity of the material.

## 5.3.3 Effect of atom number

The ability to control the number of atoms used for magnetometry is one of the main things that sets cold atom magnetometry apart in the field. Figure 5.5 shows how the sensitivity varies with atom number in the cloud, with a constant atomic density of 3 x  $10^{10}$  cm<sup>-3</sup>. The relationship between atom number and sensitivity is typified by a power law [74],

$$\delta B = aN^b \tag{5.4}$$

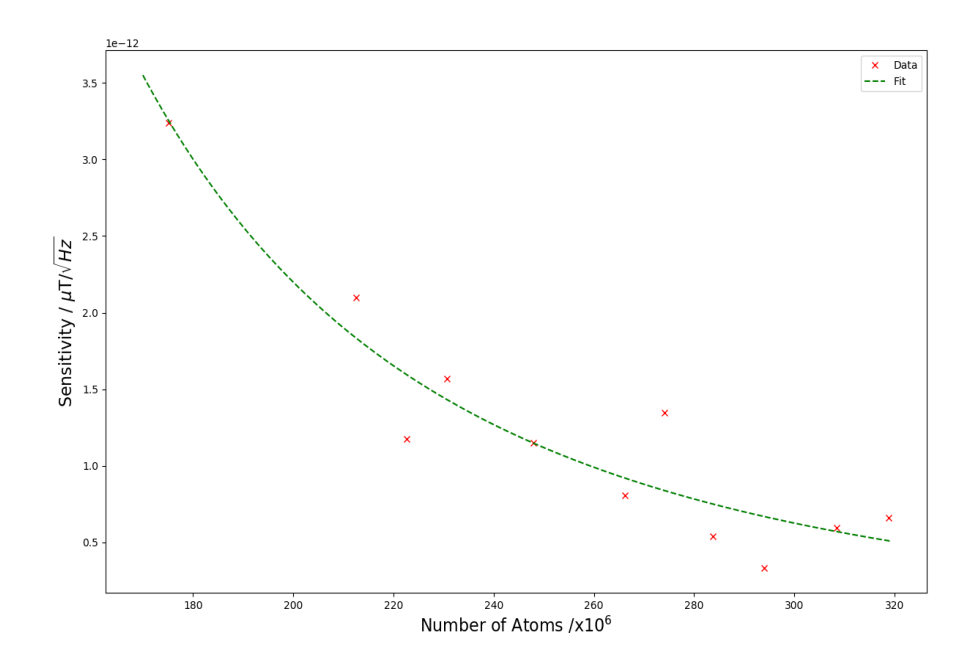


**Figure 5.5:** Sensitivity of magnetometer as a function of the number of atoms.

where N is the number of atoms, a is a constant, and b = -1.17. The 95% confidence interval for this estimate is [-1.32, -1.01]. This relationship gives important information on the limits of the magnetometer. Spin projection noise is the noise associated with the quantum fluctuations in measured populations [85]. If this was the factor limiting the sensitivity of the magnetometer, then a b value of -1/2 would be expected, as is predicted and observed for thermal magnetometry [74]. As this is not seen in the data, it is thought that the main limit on the sensitivity of the magnetometer may be due to magnetic noise and gradients. This could be counteracted by shielding the apparatus with mu-metal. Or a compensation coil system that uses a fluxgate sensor and a feedback loop (as described in [83]) to actively stabilise the field around the magnetometer could be implemented to combat the effect of magnetic noise.

#### Chapter 6

## **Conclusions and Outlook**

#### 6.1 Summary

The trapping and cooling of nuclear isomers involves both nuclear and atomic physics. Pursuing this requires knowledge and experience from two different specialities as well as specialised apparatus. This led to a situation in which the experiment and the nuclear expertise were in Jyväskylä, and the laser cooling expertise was in London. As a result, I have worked on a few different experiments, all of which are reported on in this thesis.

First, an experiment in London where the stable isotope of caesium, <sup>133</sup>Cs, is trapped and cooled in a MOT, was discussed. This is used as an analogue to the experiment in Jyväsklä. A laser system including a TA was set up and a double MOT system was constructed, with one MOT connected to an LVIS beam to supply the science MOT. The MOT's temperature and population size were characterised using an absorption imaging system, while the decay rate was found using fluorescence imaging.

Then the training I gained in London was put to use in an experiment situated on the IGISOL beam line in Jyväskylä, Finland. However, due to several city wide power cuts, the experiment suffered considerable damage. Aside from the Radiant-Dyes cooling laser, which was repaired by RadiantDyes, I undertook the repairs to the laser system. This involved re installing the cooling laser, the TA and repairing a slave laser for the repump laser.

After the repairs were made, the experiment was tested by obtaining a <sup>133</sup>Cs MOT from a vapour, specifically confirming that the laser system was functioning well enough for trapping. However, this did not give any indication as to the state of the PDMS coating, nor did it assess the performance of the experiment in the context of trapping atoms from an ionic beam. So, a MOT was found using the off line <sup>133</sup>Cs<sup>+</sup> beam, verifying that the neutraliser and the coating were in good condition. Aside from getting a MOT from the ion beam, the direct growth in the MOT population once the ion beam was allowed into the cold atoms chamber was observed. This meant that the coating was capable of thermalising atoms quickly enough that they could be trapped within minutes.

As the electronic structure shifts for different isotopes and isomers, the altered cooling and repump laser frequencies for species of interest were calculated. Having found these, a Vescent D2-135 Offset Phase Lock Servo (OPLS) was set up to accommodate these frequency changes. The range of frequency offsets available with the OPLS was 200 MHz - 9.9 GHz.

The final experiment discussed used a  $^{87}$ Rb MOT for radio frequency atomic magnetometry, which I worked on as part of my initial training. Laser-cooled atoms were used to detect AC magnetic fields. The magnetometer has a sensitivity of 330 pT/ $\sqrt{Hz}$ , and is able to operate over a range of radio frequencies, 17 kHz - 99 kHz. It was also possible to vary the number of atoms available for magnetometry, which leads to higher sensitivities.

Unfortunately due to the repairs needed to the experiment and the ongoing COVID-19 pandemic, progress in trapping isotopes and isomers was hindered. The following sections discuss upcoming work that had been delayed.

#### 6.2 Offline caesium-134 & caesium-135 ion beams

The offline sources mentioned in Section 3.5 have been used to produce a <sup>133</sup>Cs<sup>+</sup> beam. Further tests will entail obtaining a <sup>133</sup>Cs MOT from this beam source. This would involve confirming what amount of the CsNO<sub>3</sub> solution is needed for the

beam to get a visible MOT, and this could give an estimate of the efficiency of the entire process, from the CsNO<sub>3</sub> to the MOT. Such an estimate would be valuable information for the subsequent goals of producing <sup>134</sup>Cs and <sup>135</sup>Cs ion beams and trapping them.

An assessment on the logistics of using ampoule samples to capture MOTs of  $^{134}\text{Cs}$  and  $^{135}\text{Cs}$  can be made by considering the data gathered to date and presented in Sections 3.4 and 3.5. First, the procedure by which different detunings of the two calculated trapping frequencies are found will be described. The cooling laser detuning will be varied between  $\pm$  2 $\Gamma$  using the offset lock described in Chapter 4, in steps of about  $0.2\Gamma$ . Then for each cooling laser detuning, the repump laser will be cyclically varied by inputting a 10 mHz triangular wave form in to the offset lock for the repump. The peaks and troughs of the wave form will correspond to the upper and lower bands of the repump detuning,  $\pm$  100 MHz about the calculated frequency.

Fig. 3.20 shows a total of  $4.5 \times 10^{12}$  ions detected at the switchyard. The efficiency between the switchyard and the neutraliser is 43%, so this would translate to  $4.5 \times 10^{12}$  ions at the neutraliser from a single sample. The ampoules with the highest concentration of radioactive isotopes are those that were irradiated for 50 days, with 8.4% of the atoms being  $^{134}$ Cs and 2.9% being  $^{135}$ Cs. This would give us  $1.6 \times 10^{11}$  ions of  $^{134}$ Cs<sup>+</sup>, and  $5.6 \times 10^{10}$  ions of  $^{135}$ Cs<sup>+</sup>. The highest stable current from the ampoule in Fig. 3.20 was around 23 pA. Were this current maintained, the sample would be depleted after 8.7 hours. At the neutraliser this would be 8.7 hours of 9.89 pA, 0.83 pA for  $^{134}$ Cs<sup>+</sup> and 0.29 pA for  $^{135}$ Cs<sup>+</sup>.

Another consideration is that the current measured at the neutraliser is likely to actually be smaller due to the secondary current produced by the impact of the ion beam. The current measured at the neutraliser will be used as a reference point in the following assessment, and any inaccuracies in the current should be normalised.

The procedure above will allow for two cycles of repump detuning in a little over three minutes. Together with relocking the cooling laser, it can be assumed

that each cooling laser detuning will take at least 5 mins to investigate, of which there may be up to 20. So the minimum amount of time required for fully scanning the detuning of the two lasers would be 1 hour and 40 minutes. Since this is much less than the 8.7 hours that would be available at the highest stable ion beam current observed, preliminary MOT detunings may be found with one sample, if not with two.

The exact strategy may depend on the limitations of the current of the ion beam produced. If a higher current is possible, then we would be able to have a higher current of our desired isotope coming into the chamber for a shorter time comparable to one full detuning sweep, and things may proceed as they did (or better) for the MOT showing growth directly due to the ion beam. With trapping a limited number of isotopes at as of yet uncertain frequencies, there would be no issue of a large bulk of atoms emitted from the neutraliser obscuring results as was the case in the testing of the coating. Instead it would be possible to have the neutraliser heated to the optimum temperature of 900-1000 K. This would mean that the maximum of atoms that could be emitted from the neutraliser at any given time would be. If a larger ion beam current was not possible, then the neutraliser could be loaded for a short while between each round of tests, so that when the optimal detuning combination is used, a MOT signal will be seen.

#### **6.3** Planned apparatus updates

#### **6.3.1** Pneumatic gate valve

In order to protect the cold atoms chamber from room pressure in the event of another power cut, a pneumatic gate valve will be installed in front of the turbo-molecular pump. The gate valve is a CF 100 Pneumatic Bellows Sealed Gate Valve from Kurt J. Lesker. In the event of a power cut, the gate valve will shut, and prevent the venting of the system through the turbo-pump and scroll pump if they have turned off.

#### **6.3.2** MagneTOF detector

Currently the current of incoming beams is measured using the Faraday cup and the neutraliser foil. The lowest current that Faraday cups can detect is  $10^{-12}$  A. While this is more than suitable for the offline  $^{133}\text{Cs}^+$  source (4-7  $\times$  10<sup>-12</sup> A), radioactive beams will have smaller currents. A MagneTOF detector from ETP Electron Multipliers will be installed in the setup. It is capable of measuring incoming ions at a rate of  $10^{10}$  ions per second down (1.6  $\times$  10<sup>-9</sup> A) to a few ions per second.

#### Appendix A

# Fluorescence imaging MOT population calibration

This appendix outlines the process by which the fluorescence of the MOT as detected by a CCD camera is used to measure the number of atoms in a MOT [86]. The population of the MOT can be related to the counts measurement by the CCD camera by the following equation:

$$N_{MOT} = \frac{N_c}{\eta T_c \Omega \Gamma_{sc} t_{exp}} \tag{A.1}$$

where  $N_c$  is the number of counts that the CCD detects,  $\eta$  is the quantum efficiency of the sensor,  $T_c$  is the transmission coefficient for the imaging apparatus,  $\Omega$  is the solid angle,  $t_{exp}$  is the exposure time of the sensor and  $\Gamma_{sc}$  is the scattering rate, which is given by:

$$\Gamma_{sc} = \frac{\Gamma}{2} \frac{6I/I_s}{1 + (6I/I_s) + 4(\delta/\Gamma)^2}$$
 (A.2)

where  $\Gamma$  is the natural line width for the  $6s^2S_{1/2} \to 6p^2P_{3/2}$  transition, I is the intensity of the MOT beams,  $I_s$  is the saturation intensity for the cooling transition  $6s^2S_{1/2}, F = 4 \to 6p^2P_{3/2}, F = 5$ , and  $\delta$  is the detuning of the cooling laser.

The solid angle is calculated using the following equation:

$$\Omega = \frac{\pi}{4} \left( \frac{F}{D f_n} \right)^2 \tag{A.3}$$

where F is the focal length of the objective prior to the CCD, and D is the distance between the MOT and the aperture.  $f_n$  is the focal length of the objective divided by the aperture diameter. The above was used in a LabVIEW program that can simultaneously provide a live image and population of the MOT.

## Appendix B

## Baking of vacuum chamber

To reach Ultra-High Vacuum (UHV), which includes pressures from  $10^{-7}$  mbar to  $10^{-12}$  mbar, vacuum chambers must be baked. This refers to the process of heating the chamber to high temperatures to increase the desorption rate of contaminants from the chamber's inner surface while pumping away the released contaminants.

The temperature of the chamber is raised using heating tapes wrapped around it. Uniform heating of the chamber is ensured by placing three layers of aluminium foil over the chamber and heating tapes. The temperature of the baking is slowly raised in increments of 10 °C every 20 minutes until the final temperature is reached.

The final temperature of the bake varies depending on the nature of the chamber. A standard steel cold atoms chamber such as that shown in Section 2.2.2 can handle higher temperatures than the glass chamber with the PDMS coating in Section 3.1.4, though the steel glass connections of the former must be heated with care. The level of suspected contamination also affects the final temperature, as well as the baking duration.

## **Appendix C**

# PDMS coating procedure

The procedure for applying the PDMS coating to the Pyrex cold atoms chamber is based on the procedure outlined in [35]. It consists of four main stages; cleaning, evacuation, coating and installation.

First, the pyrex cell is cleaned with a mixed solution of methanol, ethanol and potassium hydroxide (KOH). The exact proportions are 45% methanol, 45% ethanol and 10% KOH. The KOH must be added after the two alcohols are mixed, and stirred at length. The solution heats up to around 40 °C when it is added. After rinsing the cell with this mixture, it is additionally rinsed with de-ionised purified water five times over.

The cell is then evacuated with a scroll and turbo pump that are directly connected. The cell is gently baked using heating tapes, the temperature is slowly raised until 120 °C is reached. This evacuation continues until the pressure of the chamber stabilises at  $10^{-6}$  mbar.

The PDMS coating is diluted with ether such that the solution is 5% PDMS and 95% ether. This is placed in the chamber and the cell is rotated at a rate of 1 Hz until the entire inner surface has been coated. The excess solution is disposed of. The chamber is once again evacuated directly to the scroll and turbo pumps, and baked at a temperature of 100 °C. This continues until the pressure reaches a stable minimum.

Then the cell is installed back onto the main line. The neutraliser along with its supports is placed within the chamber, before it is mounted onto the CF40 cross piece (shown in Figure 3.3). Then the final gentle baking (around 100 °C) of the chamber as well as the closest parts of the beam line is done. After this, the passivation of the coating takes place. This entails exposing the coating to caesium vapour from the ampoule attached to the vacuum system. As the vapour moves throughout the chamber, the adsorption sites of raw coating interact become occupied with caesium atoms. The progress of the passivation is monitored by the growing population of a MOT.

## **Bibliography**

- [1] Yuval Cohen, Krishna Jadeja, Sindi Sula, Michela Venturelli, Cameron Deans, Luca Marmugi, and Ferruccio Renzoni. A cold atom radio-frequency magnetometer. *Applied Physics Letters*, 114:073505, Feb 2019.
- [2] Luca Marmugi, Philip M. Walker, and Ferruccio Renzoni. Coherent gamma photon generation in a bose–einstein condensate of <sup>135m</sup>Cs. *Physics Letters, Section B: Nuclear, Elementary Particle and High-Energy Physics*, 777:281–285, Feb 2018.
- [3] Philip Walker and George Dracoulis. Energy traps in atomic nuclei. *Nature*, 399:35–40, May 1999.
- [4] G. Audi, O. Bersillon, J. Blachot, and A. H. Wapstra. The NUBASE evaluation of nuclear and decay properties. *Nuclear Physics A*, 729:3–128, Dec 2003.
- [5] H C Britt. Properties of fission isomers. *Atomic Data and Nuclear Data Tables*, 12:407–414, 1973.
- [6] V.I. Kirischuk, V.A. Ageev, A.M. Dovbnya, S.S. Kandybei, and Yu. M. Ranyuk. Induced acceleration of the decay of the 31 year isomer of <sup>178*m*2</sup>hf using bremsstrahlung radiation. *Physics Letters B*, 750:89–94, 2015.
- [7] D. Belic, C. Arlandini, J. Besserer, J. de Boer, J. J. Carroll, J. Enders, T. Hartmann, F. Käppeler, H. Kaiser, U. Kneissl, M. Loewe, H. J. Maier, H. Maser, P. Mohr, P. von Neumann-Cosel, A. Nord, H. H. Pitz, A. Richter, M. Schumann, S. Volz, and A. Zilges. Photoactivation of <sup>180m</sup>Ta and its implications

- for the nucleosynthesis of nature's rarest naturally occurring isotope. *Phys. Rev. Lett.*, 83:5242–5245, Dec 1999.
- [8] A. Y. Dzyublik. Triggering of nuclear isomers by x-ray laser. *JETP Letters*, 92:130–134, Aug 2010.
- [9] A. Y. Dzyublik, V. Méot, and G. Gosselin. Decay of isomers stimulated by laser radiation. *Laser Physics*, 17:760–764, May 2007.
- [10] S. N. Bose. Plancks gesetz und lichtquantenhypothese. Z. Phys, 26, 1924.
- [11] A. Einstein. Quantentheorie des einatomigen idealen gases. *Sitzber. Kgl. Preuss. Akad. Wiss*, pages 261–267, 1924.
- [12] A. Einstein. Quantentheorie des einatomigen idealen gases. *Sitzber. Kgl. Preuss. Akad. Wiss*, pages 3–14, 1925.
- [13] M. H. Anderson, J. R. Ensher, M. R. Matthews, C. E. Wieman, and E. A. Cornell. Observation of bose-einstein condensation in a dilute atomic vapor. *Science*, 269:198–201, 1995.
- [14] Tino Weber, Jens Herbig, Michael Mark, Hanns-Christoph Nägerl, and Rudolf Grimm. Bose-einstein condensation of cesium. *Science*, 299:232–235, 2003.
- [15] Vitaly L. Ginzburg. Nobel lecture: On superconductivity and superfluidity (what i have and have not managed to do) as well as on the "physical minimum" at the beginning of the xxi century. *Rev. Mod. Phys.*, 76:981–998, Dec 2004.
- [16] H. K. Avetissian, A. K. Avetissian, and G. F. Mkrtchian. Self-amplified gamma-ray laser on positronium atoms from a bose-einstein condensate. *Phys. Rev. Lett.*, 113:023904, Jul 2014.
- [17] H. K. Avetissian, A. K. Avetissian, and G. F. Mkrtchian. Gamma-ray laser based on the collective decay of positronium atoms in a bose-einstein condensate. *Phys. Rev. A*, 92:023820, Aug 2015.

- [18] E. V. Tkalya. Proposal for a nuclear gamma-ray laser of optical range. *Phys. Rev. Lett.*, 106:162501, Apr 2011.
- [19] G. C. Baldwin and Michael S. Feld. Kinetics of nuclear super-radiance. *Journal of Applied Physics*, 59:3665–3671, Jun 1986.
- [20] Daniel A Steck. Cesium D line data. http://steck.us/alkalidata, 1998. [Online; accessed 27/11/2018].
- [21] G K Woodgate. *Elementary Atomic Structure*. Oxford science publications. Oxford University Press, London, England, 2nd edition, August 1983.
- [22] Vladislav Gerginov, Andrei Derevianko, and Carol E. Tanner. Observation of the nuclear magnetic octupole moment of <sup>133</sup> Cs. *Physical Review Letters*, 91, Aug 2003.
- [23] V Gerginov, C E Tanner, and W R Johnson. Observation of the nuclear magnetic octupole moment of <sup>87</sup> Rb from spectroscopic measurements of hyperfine intervals. *Canadian Journal of Physics*, 87:101–104, January 2009.
- [24] Jun Ye, Steve Swartz, Peter Jungner, and John L. Hall. Hyperfine structure and absolute frequency of the  $^{87}$ Rb  $5p_{3/2}$  state. *Opt. Lett.*, 21:1280–1282, Aug 1996.
- [25] K. Beloy, A. Derevianko, and W. R. Johnson. Hyperfine structure of the metastable  ${}^{3}P_{2}$  state of alkaline-earth-metal atoms as an accurate probe of nuclear magnetic octupole moments. *Phys. Rev. A*, 77:012512, Jan 2008.
- [26] J S Grossman, L A Orozco, M R Pearson, J E Simsarian, G D Sprouse, and W Z Zhao. Hyperfine anomaly measurements in francium isotopes and the radial distribution of neutrons. *Hyperfine Interactions*, 120:657–660, 1999.
- [27] B. Cheal, T. E. Cocolios, and S. Fritzsche. Laser spectroscopy of radioactive isotopes: Role and limitations of accurate isotope-shift calculations. *Physical Review A Atomic, Molecular, and Optical Physics*, 86, Oct 2012.

- [28] P. Campbell, I. D. Moore, and M. R. Pearson. Laser spectroscopy for nuclear structure physics. *Progress in Particle and Nuclear Physics*, 86:127–180, Jan 2016.
- [29] W. H. King. Isotope Shifts in Atomic Spectra. Springer US, 1984.
- [30] Klaus Blaum, Jens Dilling, and Wilfried Nörtershäuser. Precision atomic physics techniques for nuclear physics with radioactive beams. *Physica Scripta*, Jan 2013.
- [31] Adriana Pálffy. Nuclear effects in atomic transitions. *Contemporary Physics*, 51:471–496, 2010.
- [32] E. Gomez, S. Aubin, G. D. Sprouse, L. A. Orozco, and D. P. DeMille. Measurement method for the nuclear anapole moment of laser-trapped alkali-metal atoms. *Phys. Rev. A*, 75:033418, Mar 2007.
- [33] M. R. Kalita, J. A. Behr, A. Gorelov, M. R. Pearson, A. C. DeHart, G. Gwinner, M. J. Kossin, L. A. Orozco, S. Aubin, E. Gomez, M. S. Safronova, V. A. Dzuba, and V. V. Flambaum. Isotope shifts in the 7s → 8s transition of francium: Measurements and comparison to ab initio theory. *Phys. Rev. A*, 97:042507, Apr 2018.
- [34] R. Calabrese L. Corradi . Dainelli A. Khanbekyan C. Marinelli E. Mariotti L. Marmugi G. Mazzocca L. Moi L. Ricci L. Stiaccini S. Agustsson, G. Bianchi and L. Tomassetti. Observation of  $7p_{3/2}$   $7d_2$  optical transitions in 209 and 210 francium isotopes. *Opt. Lett.*, 42:3682–3685, Sep 2017.
- [35] Steinn Agustsson, Giovanni Bianchi, Roberto Calabrese, Lorenzo Corradi, Antonio Dainelli, Alen Khanbekyan, Carmela Marinelli, Emilio Mariotti, Luca Marmugi, Leonardo Ricci, Leonardo Stiaccini, Luca Tomassetti, and Andrea Vanella. Enhanced atomic desorption of 209- and 210-francium from organic coating. *Scientific Reports*, 7, Jun 2017.

- [36] Arimondo E. Allegrini, M. and L. A. Orozco. Survey of hyperfine structure measurements in alkali atoms. *Journal of Physical and Chemical Reference Data*, 51(4):043102, 2022.
- [37] K. Harada T. Hayamizu M. Itoh H. Kawamura H. Nagahama K. Nakamura N. Ozawa K.S. Tanaka, U. Dammalapati and Y. Sakemi. Two-dimensional beam profile monitor for the detection of alpha-emitting radioactive isotope beam. *Nuclear Instruments and Methods in Physics Research Section A: Accelerators, Spectrometers, Detectors and Associated Equipment*, 1017:165803, 2021.
- [38] T Hayamizu M Itoh H Kawamura S Liu H S Nataraj A Oikawa M Saito T Sato H P Yoshida T Aoki A Hatakeyama T Murakami K Imai K Hatanaka T Wakasa Y Shimizu Y Sakemi, K Harada and M Uchida. Search for a permanent EDM using laser cooled radioactive atom. *Journal of Physics: Conference Series*, 302:012051, Jul 2011.
- [39] Gorelov A. Melconian D. Behr J. A. Anholm M. Ashery D. Behling R. S. Cohen I. Craiciu I. Gwinner G. McNeil J. Mehlman M. Olchanski K. Shidling P. D. Smale S. Fenker, B. and C. L. Warner. Precision measurement of the β asymmetry in spin-polarized <sup>37</sup>K decay. *Phys. Rev. Lett.*, 120:62502, Feb 2018.
- [40] V. Palmaccio X. Yu P. F. Smith E. R. Hudson P. Hamilton C. Schneider E. Chang A. Renshaw F. Malatino P. D. Meyers C. J. Martoff, F. Granato and B. Lamichhane. HUNTER: precision massive-neutrino search based on a laser cooled atomic source. *Quantum Science and Technology*, 6:024008, Feb 2021.
- [41] Christopher J Foot. *Atomic physics*. Oxford master series in atomic, optical, and laser physics. Oxford University Press, Oxford, 2007.
- [42] Carl E. Wieman and Leo Hollberg. Using diode lasers for atomic physics. *Review of Scientific Instruments*, 62:1–20, 1991.

- [43] K. B. MacAdam, A. Steinbach, and C. Wieman. A narrow-band tunable diode laser system with grating feedback, and a saturated absorption spectrometer for Cs and Rb. *American Journal of Physics*, 60:1098–1111, 1992.
- [44] T. W. Hänsch, I. S. Shahin, and A. L. Schawlow. High-resolution saturation spectroscopy of the sodium D lines with a pulsed tunable dye laser. *Phys. Rev. Lett.*, 27:707–710, Sep 1971.
- [45] Greg A. Pitz, Charles D. Fox, and Glen P. Perram. Pressure broadening and shift of the cesium D2 transition by the noble gases and  $N_2, H_2, HD, D_2, CH_4, C_2H_6, CF_4, and He_3$  with comparison to the D1 transition. *Physical Review A Atomic, Molecular, and Optical Physics*, 82, Oct 2010.
- [46] M. A. Clifford, G. P. T. Lancaster, R. S. Conroy, and K. Dholakia. Stabilization of an 852 nm extended cavity diode laser using the zeeman effect. *Journal of Modern Optics*, 47:1933–1940, 2000.
- [47] Z. T. Lu, K. L. Corwin, M. J. Renn, M. H. Anderson, E. A. Cornell, and C. E. Wieman. Low-Velocity Intense Source of atoms from a Magneto-optical Trap. *Phys. Rev. Lett.*, 77:3331–3334, Oct 1996.
- [48] E. Ramsden. *Hall-effect sensors : theory and applications*. Elsevier/Newnes, 2nd edition, 2006.
- [49] Bagnato V. S. Zilio S. Weiner, J. and P. S. Julienne. Experiments and theory in cold and ultracold collisions. *Rev. Mod. Phys.*, 71:1–85, Jan 1999.
- [50] Edwards N. H. Cooper C. J. Zetie K. P. Foot C. J. Steane A. M. Szriftgiser P. Perrin H. Townsend, C. G. and J. Dalibard. Phase-space density in the magneto-optical trap. *Phys. Rev. A*, 52:1423–1440, Aug 1995.
- [51] T. G. Walker D. W. Sesko and C. E. Wieman. Behavior of neutral atoms in a spontaneous force trap. *J. Opt. Soc. Am. B*, 8:946–958, May 1991.
- [52] Sesko D. Walker, T. and C Wieman. Collective behavior of optically trapped neutral atoms. *Physical Review Letters*, 64:408–411, 1990.

- [53] P. Laurent A. Nadir G. Santarelli A. Clairon Y. Castin D. Grison Drewsen, M. and C. Salomon. Investigation of sub-doppler cooling effects in a cesium magnetooptical trap. *Applied Physics B: Lasers and Optics*, 59:283–298, 1994.
- [54] V. Bagnato Y. Wang C. Tsao J. Weiner O. Dulieu Y. B. Band Marcassa, L. G. and P. S. Julienne. Collisional loss rate in a magneto-optical trap for sodium atoms: Light-intensity dependence. *Physical Review A*, 47:0–3.
- [55] M. Stephens and C. Wieman. High collection efficiency in a laser trap. *Physical Review Letters*, 72:3787–3790, 1994.
- [56] Tadas Pyragius. Developing and building an absorption imaging system for ultracold atoms. University of Nottingham, 2012.
- [57] Alexandros Giatzoglou, Tanapoom Poomaradee, Ilkka Pohjalainen, Sami Rinta-Antila, Iain D. Moore, Philip M. Walker, Luca Marmugi, and Ferruccio Renzoni. A facility for production and laser cooling of cesium isotopes and isomers. *Nuclear Instruments and Methods in Physics Research, Section A: Accelerators, Spectrometers, Detectors and Associated Equipment*, 908:367–375, Nov 2018.
- [58] K.H. Weber and C.J. Sansonetti. Accurate energies of nS, nP, nD, nF, and nG levels of neutral cesium. *Phys. Rev. A*, 35:4650–4660, Jun 1987.
- [59] M. Stephens, R. Rhodes, and C. Wieman. Study of wall coatings for vapor-cell laser traps. *Journal of Applied Physics*, 76:3479–3488, 1994.
- [60] H. L. Stover and W. H. Steier. Locking of laser oscillators by light injection. *Applied Physics Letters*, 8:91–93, 1966.
- [61] Agilent Technologies Italia. Agilent 4UHV Ion Pump Controller. https://www.agilent.com/cs/library/usermanuals/public/4UHV\_Controller\_User\_Manual.pdf, 2018.
- [62] Coherent. TA-0850-3000 Tapered Amplifier for MOPA Setups. https://www.coherent.com/resources/datasheet/components-

- and-accessories/DILAS\_TA-0850-3000.pdf, 2017. [Online; accessed 07/12/2021].
- [63] J. C. Vickerman, S. Y. Lai, A. Brown, and D. Briggs. The relationship between electron and ion induced secondary electron imaging: A review with new experimental observations. *Surface and Interface Analysis*, 8:93–111, 1986.
- [64] M.D. Di Rosa, S.G. Crane, J.J. Kitten, W.A. Taylor, D.J. Vieira, and X. Zhao. Magneto-optical trap and mass-separator system for the ultra-sensitive detection of <sup>135</sup>Cs and <sup>137</sup>Cs. *Applied Physics B: Lasers and Optics*, 76:45–55, Jan 2003.
- [65] C Thibault, F Touchard, S Buttgfnbach, R Klapisch, M DE Saint Simon, H T Dijong, P Jacquinot, P Juncar, S Liberman, P Pillet, J Pinard, J L Vialle A Pesnelle, The Isolde Collaboration Cern, and G Huber. Hyperfine structure and isotope shift of the D2 line of <sup>118–145</sup>Cs and some of their isomers. *Nuclear Physics*, 367:12, 1981.
- [66] Pawel Knapkiewicz. Technological assessment of MEMS alkali vapor cells for atomic references. *Micromachines*, 10:25, Dec 2018.
- [67] Raymond A Serway and John W Jewett. *Physics for scientists and engineers with modern physics*. Brooks/Cole Cengage Learning, 9th edition, 2014.
- [68] Dan Harres. Chapter 20 creating high voltage. In *MSP430-based Robot Applications*, pages 299–312. Newnes, Oxford, 2013.
- [69] Karl J Aström and Tore Hägglund. *PID Controllers: Theory, Design, and Tuning*. Instrument Society of America, 2nd edition, 1995.
- [70] Vescent. Offset Phase Lock Servo: D2-135-FC. https://www.vescent.com/manuals/doku.php?id=d2:offset\_phase\_lock\_servo, 2021. [Online; accessed 04/12/2021].

- [71] M A Laughton and D F Warne, editors. *Electrical engineer's reference book*. Newnes, 16th edition, May 2014.
- [72] H. G. Dehmelt. Modulation of a light beam by precessing absorbing atoms. *Phys. Rev.*, 105:1924–1925, Mar 1957.
- [73] William E. Bell and Arnold L. Bloom. Optical detection of magnetic resonance in alkali metal vapor. *Phys. Rev.*, 107:1559–1565, Sep 1957.
- [74] I. M. Savukov, S. J. Seltzer, M. V. Romalis, and K. L. Sauer. Tunable atomic magnetometer for detection of radio-frequency magnetic fields. *Physical Re*view Letters, 95:063004, Aug 2005.
- [75] M. P. Ledbetter, V. M. Acosta, S. M. Rochester, D. Budker, S. Pustelny, and V. V. Yashchuk. Detection of radio-frequency magnetic fields using nonlinear magneto-optical rotation. *Phys. Rev. A*, 75:023405, Feb 2007.
- [76] David A. Keder, David W. Prescott, Adam W. Conovaloff, and Karen L. Sauer. An unshielded radio-frequency atomic magnetometer with sub-femtotesla sensitivity. *AIP Advances*, 4:127159, 2014.
- [77] M. Vengalattore, J. M. Higbie, S. R. Leslie, J. Guzman, L. E. Sadler, and D. M. Stamper-Kurn. High-resolution magnetometry with a spinor bose-einstein condensate. *Physical Review Letters*, 98:200801, May 2007.
- [78] Malcolm H Levitt. *Spin dynamics*. Wiley-Blackwell, West Sussex, England, 2nd edition, March 2008.
- [79] T. Isayama, Y. Takahashi, N. Tanaka, K. Toyoda, K. Ishikawa, and T. Yabuzaki. Observation of larmor spin precession of laser-cooled Rb atoms via paramagnetic faraday rotation. *Physical Review A*, 59:4836–4839, Jun 1999.
- [80] William Happer. Optical pumping. Rev. Mod. Phys., 44:169–249, Apr 1972.

- [81] Claude Cohen-Tannoudji and Alfred Kastler. I Optical Pumping. volume 5 of *Progress in Optics*, pages 1–81. Elsevier, 1966.
- [82] W. Chalupczak, R. M. Godun, S. Pustelny, and W. Gawlik. Room temperature femtotesla radio-frequency atomic magnetometer. *Applied Physics Letters*, 100:242401, Jun 2012.
- [83] Cameron Deans, Luca Marmugi, and Ferruccio Renzoni. Sub-picotesla widely tunable atomic magnetometer operating at room-temperature in unshielded environments. *Review of Scientific Instruments*, 89:083111, Aug 2018.
- [84] Cameron Deans, Luca Marmugi, and Ferruccio Renzoni. Through-barrier electromagnetic imaging with an atomic magnetometer. *Optics Express*, 25:17911, Jul 2017.
- [85] D. J. Wineland, J. J. Bollinger, W. M. Itano, and D. J. Heinzen. Squeezed atomic states and projection noise in spectroscopy. *Physical Review A*, 50:67–88, Jul 1994.
- [86] Alexandros Giatzoglou. *Towards laser cooling and trapping of unstable caesium atoms*. PhD thesis, University College London, 2019.